Reconstruction
of π^0 and η Mesons
via Conversion
in ^{197}Au+^{197}Au at 1.23 GeV/u
with the HADES Spectrometer

von
Claudia Behnke
aus Bad Soden am Taunus

Frankfurt 2016

vom Fachbereich Physik der Johann Wolfgang Goethe-Universität
als Dissertation angenommen.

Dekan:
Prof. Dr. Rene Reifarth

Gutachter:
Prof. Dr. Joachim Stroth
Prof. Dr. Tetyana Galatyuk
Datum der Disputation:

Sometimes I've believed as many as six impossible things before breakfast.

Queen of Hearts, Alice in Wonderland

Abstract

Lepton pairs emerging from decays of virtual photons represent promising probes of nuclear matter under extreme conditions of temperature and density. These extreme conditions can be reached in heavy-ion collisions in various facilities around the world. Hereby the collision energy in the center-of-mass system ($\sqrt{s_{NN}}$) varies from few GeV (SIS) to the TeV (LHC). In the energy domain of 1 - 2 GeV per nucleon (GeV/u), the HADES experiment at GSI Helmholtzzentrum für Schwerionenforschung in Darmstadt studies dielectrons and strangeness production. Various reactions, for example collisions of pions, protons, deuterons and heavy-ions with nuclei have been studied since its installation in the year 2001. Hereby the so called *DLS Puzzle* was solved experimentally [A$^+$10c], with remeasuring ^{12}C+^{12}C at 1 and 2 GeV/u [ea08, ea07] and by careful studies of inclusive pp and pn reactions at 1.25 GeV [Gal09]. With these measurements the so-called reference spectrum was established. Measurements of e^+e^- production ^{40}Ar+KCl showed an enhancement on the dilepton spectrum above the trivial NN background. Theory predicts a strong enhancement of medium radiation with the system size, due to large production of fast decaying baryonic resonances like Δ and N^*. The heaviest system measured so far was Au+Au at a kinetic beam energy of 1.23 GeV/u. The precise determination of the medium radiation depends on a precise knowledge of the underlying hadronic cocktail composed of various sources contributing to the measured dilepton spectrum. In general the medium radiation needs to be separated from contributions coming from long-lived particles, that decay after the freeze out of the system. For a more model independent understanding of the dilepton cocktail the production cross sections of these particles need to measured independently. In the related energy regime the main contributers are π^0 and η Dalitz decays. Both mesons have a dominant decay into two real photons and have been reconstructed successfully in this channel [AHMS03]. Since HADES has no electromagnetic calorimeter the mesons can not be identified in this decay channel directly. In this thesis the capability of HADES to detect e^+e^- pairs from conversions of real photons is demonstrated. Therefore not only the conversion probability but also the resulting efficiencies are shown. Furthermore, the reconstruction method for neutral mesons will be explained and the resulting spectra are interpreted. The measurement of neutral pions is compared to the independent measured charged pion distribution, and extrapolated to full phase space. An integrated approach is used to determine the η yield. Both measurement are compared to the world data and to theory model claculations. Finally, the measurements will be used together with the reconstructed dilepton spectra to determine the amount and the properties of in medium radiation in the Au+Au system.

Kurzfassung

Leptonenpaare, welche aus dem Zerfall virtueller Photonen stammen, sind einer der vielversprechenden Proben zur Untersuchung von Kernmaterie unter extremen Bedingungen. Diese extremen Bedingungen können in Schwerionenkollisionen in Forschungseinrichtungen auf der ganzen Welt erzeugt werden. Die Kollisionsenergie variiert hierbei von wenigen GeV (SIS) bis hin zu TeV (LHC). Im Energieberreich von 1-2 GeV/u studiert das HADES Experiment, welches am GSI Helmholtzzentrum für Schwerionenforschung in Darmstadt platziert ist, Dielektonen- und Seltsamkeits Produktion. Verschiedenste Reaktionssysteme, zum Beispiel Kollisionen von Pionen, Proton, Deuteronen und Schwerionen mit Kernen, wurden seit der Installation im Jahr 2001 gemessen. Hierbei wurde das sogenannte *DLS Puzzle* experimentell gelöst, indem die Systeme ^{12}C+^{12}C bei 1 und 2 GeV/u sowie ^{40}Ar+KCl bei 1.76 GeV/u erneut gemessen wurden [ea07, A$^+$11a]. Diese Messungen bestätigen die Überhöhung des Dileptonen Spektrums über dem trivialen NN Hintergrund. Außerdem wurde dieser NN Hintergrund mit n+n und n+p Reaktionen bei 1.25 GeV detailliert studiert [Gal09]. Theoretische Rechnung sagen einen starken Anstieg der Mediumstrahlung mit der Systemgröße vorher, bedingt durch eine starke Produktion schnell zerfallender baryonischer Resonanzen, wie etwa Δ und N^*. Das schwerste bisher gemessene System ist ^{179}Au+^{179}Au mit einer kinetischen Stahlenergie von 1.23 GeV/u. Die präzise Bestimmung der Mediumstrahlung hängt von der genauen Kenntnis des darunterliegenden hadronischen Cocktails ab, welcher aus verschiedensten Quellen, die zum Dilepton Spektrum beitragen, besteht. Im Allgemeinen muss die Mediumstrahlung von Beiträgen langlebiger Teilchens getrennt werden, welche nach dem Ausfrieren des Systems zerfallen. Für ein modellunabhängigeres Verständniss des Dileptonen Cocktails sollten die Produktions Wirkungsquerschnitte dieser Teilchen unabhängig gemessen werden. Im relevanten Energiebereich stammen die größten Beiträge von π^0- und η- Dalitz Zerfällen. Beide Mesonen zerfallen dominant in zwei reale Photonen und wurden in diesem Zerfalskanal erfolgreich rekonstruiert [AHMS03]. Da in HADES kein elektromagnetisches Kaloriemeter installiert ist, ist eine Identifikation in diesem Zerfalskanal nicht direkt möglich. In dieser Arbeit wird die Fähigkeit von HADES demonstriert e^+e^- Paare, welche aus Konversion dieser realen Photonen stammen, zu identifizieren. Dafür wurde nicht nur die Konversionswahrscheinlichkeit bestimmt, sondern auch die resultierenden Effizienzen. Des Weiteren wird die Rekonstruktionsmethode für neutrale Mesonen erklärt und die entstandenen Spektren interpretiert. Die Messung neutraler Pionen wird mit der unabhängigen Messung geladener Pionen verglichen und zum totalen Phasenraum extrapoliert. Eine integrierte Herangehensweise für die Korrekturen wird ebenfalls erklärt und später zur Bestimmung des η Beitrages genutzt. Letztendlich wird die Messung, zusammen mit dem rekonstruierten Dileptonen Spektrum, genutzt, um die Menge und die Eigenschaften der Medium Strahlung des Au+Au Systems zu bestimmen.

Contents

Part I
Introduction and Motivation

In the beginning the Universe was created. This has made a lot of people very angry and has been widely regarded as a bad move.

Douglas Adams - The Hitchhiker's Guide to the Galaxy

13.7 billion years ago [H$^+$13, A$^+$15], our universe was created in the so-called *Big Bang*, and started to expand. After 10^{-12} seconds, elementary particles were created. Today, we know six different types of quarks (u, d, s, c, b, t) and six different types of leptons ($e^\pm, \mu^\pm, \tau^\pm, \nu_e, \mu_\mu, \nu_\tau$). Furthermore, there are 12 known exchange bosons (photon γ, W$^\pm$- and Z-Bosons and 8 gluons g) that mediate the forces (see Figure 0.1). The universe expanded further, cooled down and the quarks were combined into hadrons after 10^{-6} seconds. Two types of hadrons are established. Baryons are composed of three quarks and mesons are a combination of a quark-anti-quark pair. Both are bound by the strong force, which is described by the corresponding theory of Quantum Chromodynamics (QCD) and is mediated via so-called color charge. Baryons are color neutral objects, which can only be explained by three colors (red, blue, green) that combine into neutral white. Mesons contain color and anti-color and are therefore color neutral as well. Furthermore, the coupling constant α_{QCD} becomes asymptotically weaker as energy increases and distance decreases [GW73, Pol73]. Therefore, quarks are confined within the hadrons [Wil74]. Protons and neutrons, the constituents of atomic nuclei, are baryons. Together with the electromagnetic force, described by the theory of Quantum Electrodynamics (QED), the strong force forms the matter that surrounds us in daily life. The electromagnetic force binds the negatively charged electrons to the positive charge of the nucleus. This finally form atoms, which are the constituents of everything that we currently know.
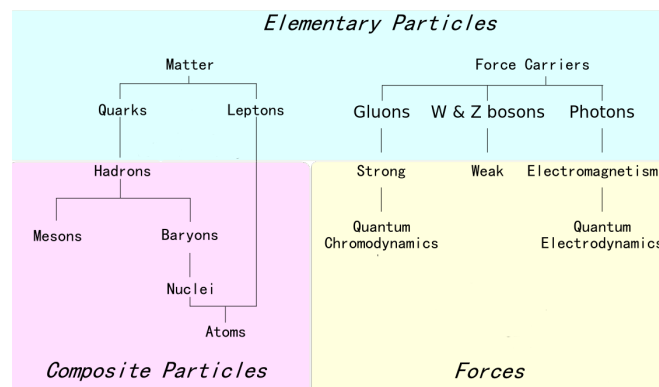

Figure 0.1: The standard model of nuclear physics includes two types of matter particles (upper left) and 12 exchange bosons (upper right). In the lower left part the compound particles are shown. In the lower right part the forces are assigned to their exchange particles.

1 Nuclear Matter and the QCD Phase Diagram

The study of the nature of nuclear matter begun in 1911 when Rutherford found the nucleus inside the atom [Rut11]. Since those days nuclear matter was studied intensively through experiments and theory. Today the QCD phase diagram (Shown in Figure 1.1) describes the behavior of nuclear matter as a function of (net-baryon) density (or baryochemical potential, μ_B) and temperature (T). μ_B describes nothing more, but the difference of number between particles and antiparticles in a system. With high energy densities the confinement of the nu-
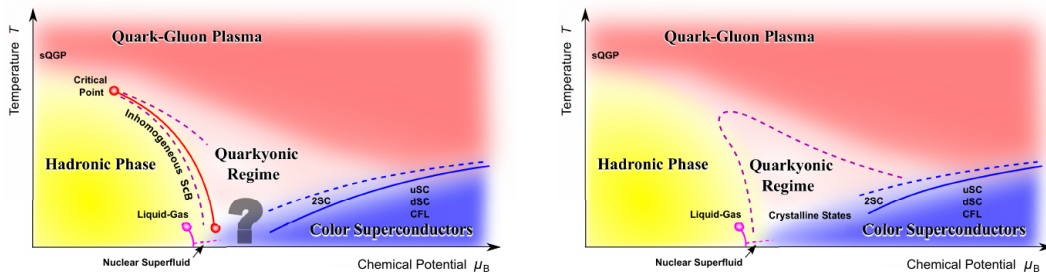
Figure 1.1: Two possible scenarios for the QCD phase diagram. Left panel: including the QCD critical point(s), right panel: without the first-order phase transition at all [FH11, FS13].

clear matter can be revoked and a quark gluon plasma (QGP) can be created [BN77]. At vanishing baryochemical potential the transition to this phase is a smooth crossover, according to Lattice QCD calculations [BBC+90, FK04]. At higher baryochemical potentials a first order phase transition is predicted (red line in Figure 1.1, left hand site) into the deconfined phase [SPW07]. This phase transition should end in a critical point, predicted by various calculations [Ste09, Ste11, CHJ+09, GG11]. Nevertheless, possible scenarios without any phase-transition exist as well [FS13] (Figure 1.1, right hand panel). Besides deconfinement, restoration of chiral symmetry is predicted at these high densities [NJL61]. The chiral phase transition is most likely a cross over type, and indicated with the pink dashed line in Figure 1.1. Calculations with infinite number of colors [MP07] predict a third region, where the nuclear matter is chirally restored but confined. This region, called quarkyonic regime, exists independent whether deconfined phase transition is a cross over or first order. The created matter has, on the one hand, quark as degrees of freedom, but is, on the other hand, still confined. In the *bag model* [BR79], where a hadron is calculated as quarks interacting with the surface of a bag, quarkyonic matter is described as one big bag, filled with quarks. A possible signature of this state is given by electromagnetic interactions. (Virtual) photons, interacting with this matter, might signal that quarks are still localized in baryons [TVL14, Vog14]. At even higher baryochemical potentials more exotic phases are predicted [ASRS08, Bar77],which are likely not accessible in heavy-ion reactions

1.1   Spontaneous Chiral Symmetry Breaking

The standard model can describe mass creation by the coupling of the elementary particles to the Higgs field [EB64, Hig64, GHK64]. The self interaction of this field is the so-called *Higgs particle*, which was discovered in 2012 at the LHC [C$^+$12, A$^+$12a]. The mass of the lightest quarks that are created by the higgs mechanism are in the order of a few MeV/c^2 [N$^+$10]. Comparing those to the mass of a nucleon (M_p = 938 MeV/c^2), the contributions from the Higgs-field are less than one percent. The formation of massive nucleons out of (nearly) massless quarks is an unique feature of QCD and the exact mechanism is still not understood. One of the most promising theories to describe the dynamically creation of masses is chiral symmetry breaking [PMW$^+$06, Wil99, Koc97]. Symmetries have been a very successful concept for understanding fundamental laws of physics, especially in quantum field theories (QFT). Besides the space-time symmetries (Poincaré [Poi06] and CPT [Kos98]), the Lagrangian also has internal symmetries, for example the local $SU(3)$ gauge symmetry, that describes the color charges and the coupling to the exchange bosons (gluons). Chiral symmetry describes the independence of left and right handed (or chiral) particles coupling in QCD and can be divided into vector symmetry and axial vector symmetry. A consequence of chiral symmetry is appearance of parity doublets[1] in the hadron spectrum [VW91] which, however, do not occur in nature. The Lagrangian itself contains both symmetries, but the ground state (i.e., the vacuum) does not, this means that spontaneous symmetry breaking has taken place. In Figure 1.2 a mechanical example of spontaneous symmetry breaking is shown. On the left panel the minimum of the potential is just in the center and potential as well as ground state are invariant under rotations. The right panel shows the and rotational invariant potential, but the minimum lies at a certain distance from the center. The central point is a point of unstable equilibrium, which means a ball put there would certainly roll down to minimum potential. Even though the symmetry is broken, the potential itself maintains its rotational

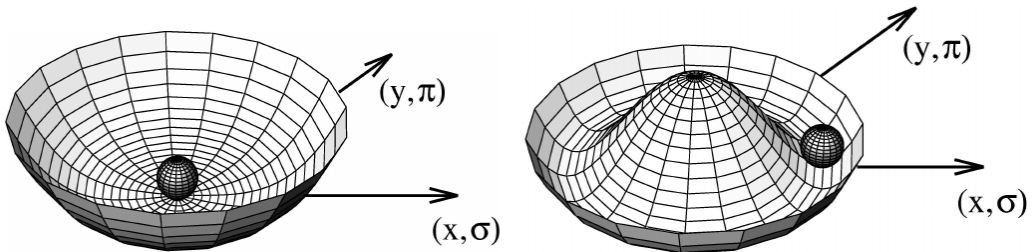Figure 1.2: Spontaneous symmetry breaking in a mechanical example. On the left hand side the potential and ground state exhibit rotational symmetry, while on the right hand side only the potential is symmetric but for the ground state symmetry is broken. The right potential is often called *Mexican hat*.

---

[1]mesons with same quark content, but different parity i.e. ρ ($J^P = 1^-$) and a_1 ($J^P = 1^+$)

symmetry. Rotational excitations will not cost any energy whereas radial excitations do. In nature, the vector symmetry is still preserved, but the axial symmetry is spontaneously broken in the QCD-field. Goldstone's theorem says, that as soon as a generic continuous symmetry is broken, new scalar massless particles appear in the spectrum of possible excitations, the so-called Goldstone bosons [Gol, Nam60]. These bosons are a result of rotational excitations in the picture of Figure 1.2. Assuming the existence of only up (u) and down (d) quarks,

the Goldstone bosons are the isotriplet of the π mesons. Including the strange (s) quark, the Goldstone bosons correspond to the members of the light pseudo-scalar[2] octet, the π, k and η mesons, shown in Figure 1.3. In this representation the mesons are characterized by their isospin and their (net) strangeness. These properties can be translated to the quark picture. Particles with positive strangeness are the kaons that contain an $\bar{s}$ quark, while negative strangeness implies an s quark as content. Studying kaons gives further access to the understanding of

Figure 1.3: Graphical representation of the scalar meson octet

chiral symmetry breaking, but is part of a different work [Sch16, Sch15]. Non-strange particles, π- and η mesons, are the main observable used in this work and will be discussed now in greater detail.

1.2   Properties of Pion and Eta Mesons

In 1947, as the first mesons, the charged pions $\pi^\pm$, were discovered in cosmic ray experiments [LMOP47]. They have a mass of 139.57 MeV/c^2 and their quark content is $\pi^+ = u\bar{d}$ and $\pi^- = d\bar{u}$ [N+10]. Even so they are stable under the strong interaction, they can decay weakly into (anti-)leptons (e$^\pm$,$\mu^\pm$) and their corresponding (anti-)neutrinos (ν_e, ν_μ), which gives them an average lifetime of 26 ns. The neutral π^0 was discovered shortly later in 1950 via its two-γ decay channel [SPS50]. With a mass of 134.97 MeV/c^2 it is slightly lighter than the charged pions and has a much shorter lifetime of $8.4 \cdot 10^{-17}$ seconds. It consists out of a combination of u and d quarks:

$$\pi^0 = (u\bar{u} - d\bar{d})/\sqrt{2}, \tag{1}$$

---

[2] pseudo-scalar mesons have total spin 0 and odd parity (usually noted as J^P=0$^-$)

This means that all the main quantum numbers (charge, strangeness, isospin$_z$) are equal to zero. The η meson shares this property with the π^0 and therefore is located at the same position in the meson octet. It was first observed in 1961 in pion-nucleon collisions at the Bevatron [P+61]. The η' meson was discovered independently by two groups in 1964 [K+64, G+64]. The measured η states are a superposition of the QCD eigenstates η_1 and η_8:

$$\begin{pmatrix} \cos\theta_P & -\sin\theta_P \\ \sin\theta_P & \cos\theta_P \end{pmatrix} \begin{pmatrix} \eta_8 \\ \eta_1 \end{pmatrix} = \begin{pmatrix} \eta \\ \eta' \end{pmatrix} \tag{2}$$

The η_1 and η_8 mesons are essentially a different superposition of the wave functions of the same quarks.

$$\eta_1 = \frac{u\bar{u}+d\bar{d}+s\bar{s}}{\sqrt{3}} \text{ and } \eta_8 = \frac{u\bar{u}+d\bar{d}-2s\bar{s}}{\sqrt{6}}. \tag{3}$$

Since the mixing angle is small (Θ_p = -11.5°), the measured η particle is close to η_8 and the η' is close to η_1. With a mass of 547.86 MeV/c^2 the η is significantly heavier than the pions and the η' is even heavier with a mass of 957.78 MeV/c^2[N+10]. Due to this high mass the η' is not produced at the investigated energies, and is therefore not a part of this work. In Table 1.1 the properties of the η and the π^0 mesons are listed. Only a selection of the possible decay channels is shown.

Meson	Mass [MeV/c^2]	Life time [fm/c]	Decay	Branching ratio
π^0	134.97	7.7·10^5	$\gamma\gamma$	98.82 ± 0.03 %
			γe^+e^-	1.17 ± 0.04%
			$e^+e^-e^+e^-$	(3.34 ± 0.16) ·10^{-5}
η	547.86	5.0 ±0.3 · 10^5	$\gamma\gamma$	39.41 ± 0.20 %
			$\pi^0\pi^0\pi^0$	32.86
			$\pi^+\pi^-\pi^0$	22.92
			γe^+e^-	(6.9 ± 0.4) ·10^{-3}
			$e^+e^-e^+e^-$	(2.40 ± 0.22) ·10^{-5} %

Table 1.1: Quantities of η and π^0 mesons

1.3 Generation of Hadron Masses

If chiral symmetry was be only spontaneously broken in nature, the Goldstone bosons (pions) would have to be be massless, which is in contradiction to their observed properties. In addition to the spontaneous symmetry breaking, the chiral symmetry is explicitly broken as well. In case of a spontaneous breaking, the potential is still symmetric, whereas in case of an explicit breaking the potential is

not symmetric anymore. Since the contribution of quark masses in the Lagrangian is very small compared to Λ_{QCD}[3], the explicit breaking of chiral symmetry is very small as well. In the mechanical analogue of Figure 1.2, the breaking can be understood as a slight tilt of the Mexican-hat potential. The ground state of QCD is populated by scalar quark-antiquark pairs ($<q\bar{q}>$ condensate) and does not share the symmetry of the Lagrangian. These pairs are called chiral condensate and are responsible for a dynamic creation of the mass of the nucleon. With increasing temperature, a melting of the chiral condensate is predicted, which would lead to a restoration of the chiral symmetry. A similar situation can be realized by reaching high baryon densities where the chiral condensate is literally squeezed out. In Figure 1.4 the *melting* of the chiral condensate calculated within the Nambu-Jona-Lasinio model (NJL) is shown [FLW98]. The region, marked in red, shows densities and temperatures accessible with the SIS18 accelerator. According to the NJL model, the chiral condensate would have already decreased by 30-50%, so chiral symmetry should be partially restored. But the chiral condensate is not directly observable and there is no known direct experimental signature. A connection between hadronic observables and the condensate is realized via QCD sum rules by integration over hadronic spectral functions and operator product expansion [HL92, LM98]. Even though QCD sum rules do not give explicit predictions for masses and widths of hadrons, modern calculations, based on effective Lagrangians, predict a strong modification of the spectral functions of vector mesons within a hot and dense nuclear system. The spectral functions would be broadened and their pole masses shifted to lower masses [HR14], which could be observed with current experiments.
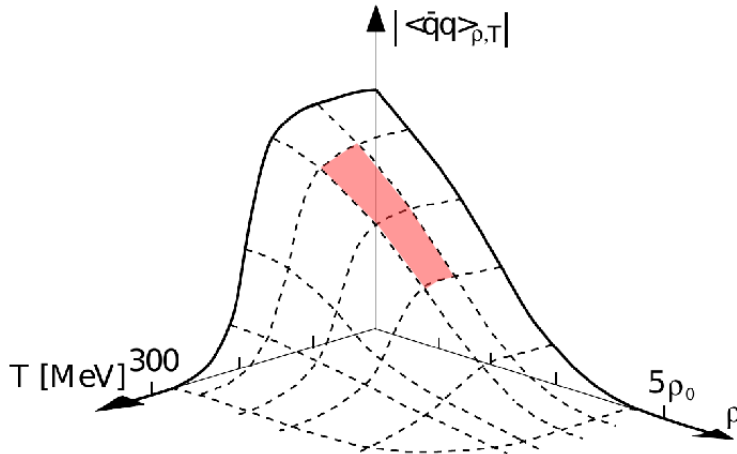

Figure 1.4: Melting of the chiral $<\bar{q}q>$condensate as a function of temperature and density. [Wei93] calculated in a Nambu-Jona-Lasinio model [NJL61]. The region accessible with SIS18 is shown in red.

---

[3]Λ_{QCD} represents the order parameter of QCD and is typically in the order of ≈ 200 MeV/c^2

1.4 Vector Meson Dominance and Form Factors

Force interactions are mediated via exchange particles. In the QED the exchange particle is a photon and allows the electromagnetic coupling of leptons to electrically charged quarks, and therefore to the hadrons. Since those photons only exist for a very short time, the uncertainty principle [Hei27] allows them to violate momentum and energy conservation. Therefore, they are called *virtual* photons. Two types of virtual photons exist. The space-like photons do not transfer energy but only momentum and are used to probe charge distributions. When for example an e^- is scattered on a probe, the momentum transfer, which corresponds to the momentum of the virtual γ, is measured. If the virtual photon transfers only energy but no momentum, it is called time-like. Such photons are studied in annihilation of e^+ and e^-. In the time-like region one observes the resonance interaction between photons and hadrons. Furthermore, the quantum numbers of a (virtual) photon are $J^P = 1^-$ and therefore equal to those of the vector mesons ρ, ω and ϕ (See Table 1.2). In 1960 J.J Sakurai introduced the vector meson dominance model (VMD), which describes photon-hadron interactions [Sak60]. It interprets the coupling of virtual photons with hadrons via intermediate vector mesons. At the SIS18 energy regime only the vector mesons up to ≈ 1 GeV/c^2 are produced. The lifetime of the ρ meson is 1.3 fm/c, and small compared to the lifetime of the fireball created in the core of a heavy-ion collision ($\tau = 10$ fm/c [VPS$^+$08]). This short lifetime allows a decay inside the dense medium, which makes the ρ meson a promising candidate for the measurement of the modification of the spectral functions as a result of chiral symmetry restoration. In Table 1.2 the branching ratios of light vector mesons into dilepton pairs are shown. Those branching ratios are much smaller than those of hadronic decays because of the small coupling constant $1/(\alpha_{em})^2 = 1/(137)^2 \approx 10^{-5}$ [Pes95].

Meson	Mass [MeV/c^2]	Decay width [MeV/c^2]	Life time [fm/c]	Branching ratio e^+e^-
ρ	775	149	1.3	$4.72 \cdot 10^{-5}$
ω	783	8.49	23.4	$7.28 \cdot 10^{-5}$
ϕ	1020	4.26	44.4	$295 \cdot 10^{-4}$

Table 1.2: Properties of light vector mesons [N$^+$10]

VMD can be further used to understand the electromagnetic transition form factors of Dalitz decays ($M \rightarrow Xe^-e^+$). The form factor $F(q)$ is an experimental observable to describe the deviation from scattering of the probe on point-like objects. They are used describe the scattering of particles on extended targets, and depend on the transfered momentum q. They have been used in measurements of electron scattering on nucleons and gave some of the first evidence of the existence of quarks and gluons [BCD$^+$69, BFK$^+$69]. Strong and electromagnetic interactions have to conserve all quantum numbers. Under the assumption of the

exchange of one single photon, conservation can be achieved either by identical in- and outgoing particles, or the occurrence of new particles, where the total quantum numbers are identical to the incoming ones. The first case are called *elastic* (or static) form factors and the second *transition* (or dynamical) form factors. For non-relativistic, spin 0 particles, the elastic form factors are a modification to the Rutherford scattering [Rut11]:

$$\left(\frac{d\sigma}{d\Omega}\right) = \frac{\alpha^2(\hbar c)^2 \cos^2(\Theta/2)}{4E^2 \sin^4(\Theta/2)} \cdot \left|F(q^2)\right|^2 = \left(\frac{d\sigma}{d\Omega}\right)_{point-like} \left|F(q^2)\right|^2, \qquad (4)$$

The from factor is the Fourier transformation of the charge distribution of the scattering target. A form factor of one is equivalent to a point-like object. The transition form factor for the Dalitz decay can be calculated from QED [Lan85]:

$$\frac{d\Gamma(P \to l^+ l^- \gamma)}{dq^2 \Gamma(P \to \gamma\gamma)} = \frac{2\alpha}{3\pi}\left[1 - \frac{4m_l^2}{q^2}\right]^{1/2}\left[1 + 2\frac{m_l^2}{q^2}\right]\frac{1}{q^2}\left[1 - \frac{q^2}{m_p^2}\right]^3\left|F_P(q^2)\right|^2 \quad (5)$$

$$= \left(\frac{d\Gamma}{dq^2}\right)_{QED} \cdot \left|F_P(q^2)\right|^2 \qquad (6)$$

If only electromagnetic effects play a role in the transition the from factor is equal to one. The decay of a pseudoscalar particle into a dilepton pair is not possible due to C-parity conservation. Nevertheless, the decay is possible via a two-step process like $M \to X\gamma^* \to Xe^-e^+$ (Shown in Figure 1.5). In this case the transition form factor describes the electromagnetic structure of the vertex M$\to X\gamma$, which defines the electromagnetic properties of this hadron. Taking into account VMD, this process is described very well. Detailed knowledge of the form factors is not only important for an understanding of the structure of hadrons, it contributed also to the interpretation of the dilepton spectra from heavy-ion collision experiments. In the following, the form factors of π^0 and η will be discussed.
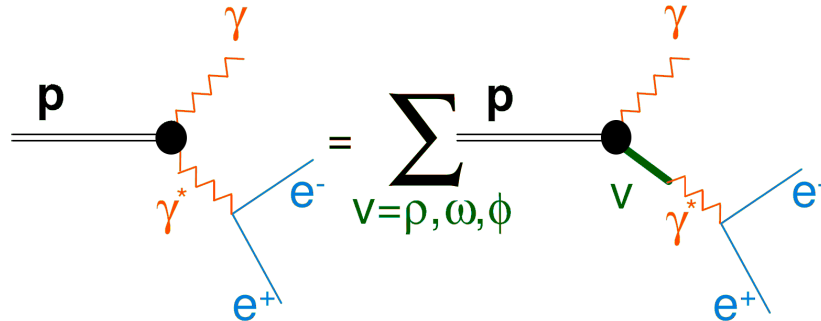
Figure 1.5: Diagrams of transition form factors for pseudoscalars in the VDM.

1.4.1   Form Factor of Pions

Figure 1.6 shows the pion form factor, which has been measured in a large energy range. The time-like region, where $q^2 \geq 4m_\pi^2$, has been accurately explored by various lepton colliders. Inverse electro production ($\pi^- p \to e^+ e^- n$) covers the lower q^2-region just above $4m_\pi^2$. In the space-like region, majority of data are available from $e\pi$ elastic scattering, complemented with data from the π-electro production reaction ($eN \to e\pi N$). The measured data sets can be described by a Breit-Wigner function:

$$|F_\pi(q^2)|^2 = \frac{m_\rho^4}{(q^2 - m_\rho^2)^2 + m_\rho^2 \Gamma_\rho^2}, \tag{7}$$

where m_ρ is the mass and Γ_ρ the width of the ρ meson. This simple-pole description clearly suggests and illustrates the success of the vector-meson dominance model.

Figure 1.6: The pion form factor as function of energy. It is determined from colliding beams, inverse electro production, and electro production measurements. The theoretical curves are discussed in [dMFPS06]. Data is taken from [BDG⁺99, BDG⁺00, Vol01].

1.4.2 Form Factor of Eta Meson

Measurements of the form factor of the η meson are challenging, and in total only two data sets were obtained. The dielectron channel, measured with the SND detector, located at VEPP-2M-Collider, 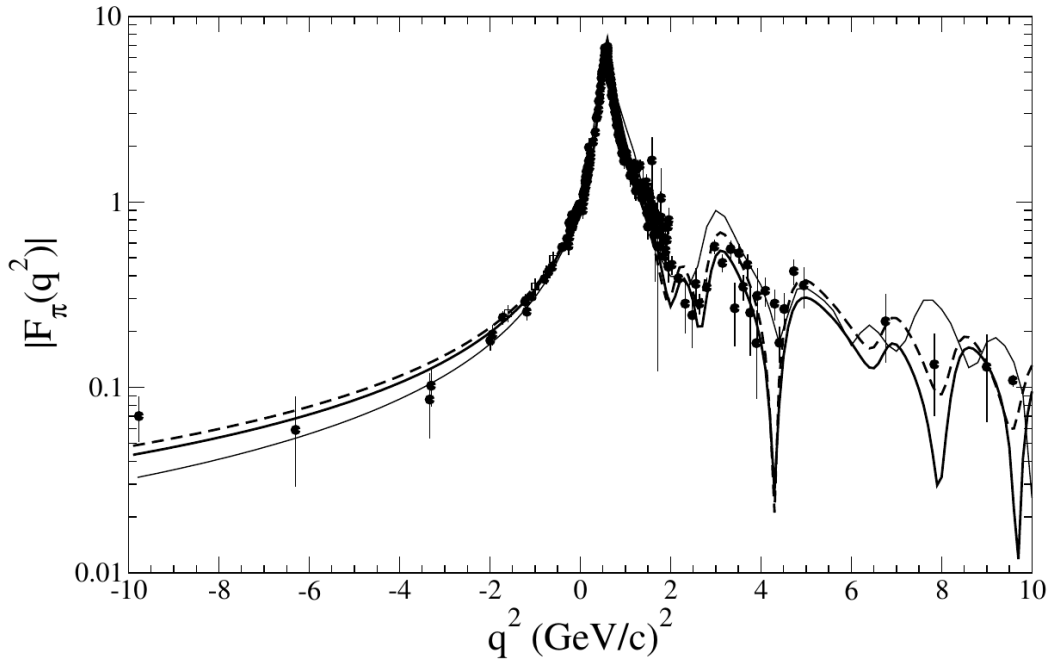suffers from impurities caused by dilepton pairs from external conversion [A+01]. Figure 1.7(a) shows the obtained data together with predictions from the VMD. The fit with the function:

$$F_\eta = \left(1 - \frac{q^2}{\Lambda_\eta^2}\right)^{-1} \tag{8}$$

gives an inverse slope of $1/\Lambda_\eta = 1.6 \pm 2.0 \, \text{GeV/c}^{-2}$, which is in agreement with the VMD as well a with F=1, suggesting a pure QED process. While the measurement in the dimuon channel does not suffer from external conversion, the decay in muons is suppressed by another order of magnitude compared to the dielectron channel. Figure 1.7(b) shows the results obtained by various experiments [Ura11] which are in agreement with the VMD assumption.

(a) $\eta \rightarrow e^+e^-\gamma$ (b) $\eta \rightarrow \mu^+\mu^-\gamma$
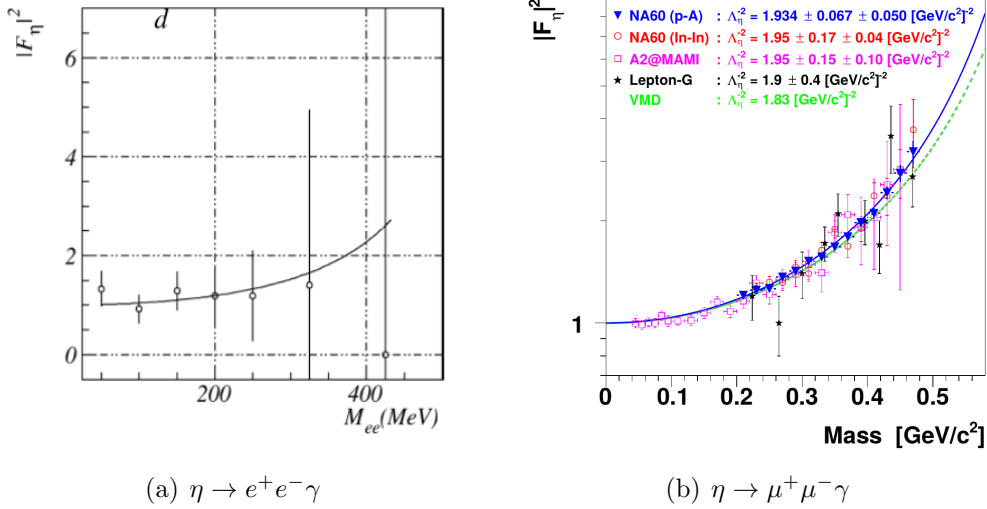
Figure 1.7: Eta form factor obtained in 2 different decay channels [DGK+, Ura11].

2 Meson Production in NN Reactions

Proton proton (p+p) collisions are used to study the production of (pseudoscalar) mesons and are used as baseline studies for heavy-ion experiments. Measurements of mesons near their production threshold help to understand the mechanisms of hadrons further. Consider a neutral meson M is created in a p+p collision, where one proton is in rest:

$$p + p \rightarrow p + p + M \tag{9}$$

Energy must be conserved

$$E = 2\gamma m_p c^2 = 2m_p c^2 + m_M c^2 \tag{10}$$

where γ in the center of mass system is:

$$\gamma = \frac{1}{\sqrt{1 - (\beta_{lab/c^2})^2}} \text{ with } \beta_{lab} = \frac{2\beta_{cm}}{1 + \beta_{cm}^2/c} \text{ and } \beta = 1 - \left(\frac{2m_p}{2m_p + m_M}\right)^2 \tag{11}$$

Here γ is the Lorenz factor. The total energy of the incoming proton is the sum of its mass and the kinetic energy T_{kin}, which is equivalent to the beam energy E_b:

$$E = T_{kin} + m_p c^2 = E_{beam} + m_p c^2 \tag{12}$$

Using theses relations, the minimum beam energy E_b for the production of the π^0 and η mesons, one gets:

$$E_b^{\pi^0} = 280 \text{ MeV and } E_b^{\eta} = 1261 \text{ MeV} \tag{13}$$

Reactions with these minimum energies will produce mesons which have no kinetic energy. To be reconstructed within a detector, the particle would need to have a kinetic energy at least a few MeV. In the case of the HADES detector the minimum momentum of an accepted $\pi^{\pm}$ is in the order of 50 MeV. This increases the minimum kinetic beam energy about 100 MeV in the $\eta \to \pi^+ \pi^- \pi^0$ channel. The same is true for the reconstruction of the lepton coming from the Dalitz decay.

In main focus of this chapter is the η production. The inclusive production cross sections of the η meson are well known, but at higher energies the existing data have large errors. The exclusive reconstruction of the η decays is an optimal tool to study the η-Dalitz decay. The only existing data sets before the measurement campaigns of HADES are shown in Figure 1.7(a). Measurements by CELSIUS of the angular distributions of the η showed non-isotropic production and showed a maximum of emitted η mesons perpendicular to the beam direction [C+99]. Later measurements from COSY, on the other hand, show no deviation from isotropy [AB+03]. The DISTO experiment observed polar angle anisotropy of the η in systematic exclusive measurements in p+p at beam energies of E_b = 2.15 GeV, 2.50 GeV, and 2.85 GeV. They also showed that the anisotropy vanishes with increasing beam energy [B+04b]. These findings have been included in the simulation package PLUTO which is used for this work. The HADES collaboration has measured p+p collisions in 3 different beam energies, namely E_b = 1.25 GeV, 2.2 GeV, and 3.5 GeV, which will now be discussed in detail.

2.1   Eta production in p+p and n+p at 1.25 GeV

Besides mesons ($NN \rightarrow NNM$) excited baryonic resonances ($NN \rightarrow N\Delta$, $NN \rightarrow NN^*$) can be formed in nuclear collisions. Baryonic resonances, with three u and/or d quarks, are called, depending on their isospin, N* (I = 1/2) or Δ (I = 3/2) resonances. These resonance are understood as excited protons or neutrons, and have a very short life time and are therefore broad[4]. Another source for particle production is NN bremsstrahlung. Here, the nucleons exchange a boson (usually realized by a meson) and then emit a virtual photon, which then decays into a dilepton. The theoretical assumption for bremsstrahlung productions is one-boson exchange models (OBE) [SM03, SBCM89]. Figure 2.1 (left panel) shows the corresponding Feynman diagram. Such process can be accompanied by excitation of baryonic resonances. These resonances then decays via emission of a virtual photon and nucleon. In Figure 2.1 (right panel) the corresponding Feynman diagram is shown. Diagrams of the same type, where a virtual photon is emitted from the other nucleon, are also included in the calculations. In all of these processes the baryonic resonance is produced off-shell (mass shell in this case) because the virtual photon does not obey energy and momentum conservation. The lowest energy at which HADES measured the p+p reactions was 1.25 GeV. This leads to resonances that are produces below their pole mass. Like for all virtual photons, strong coupling to the ρ meson
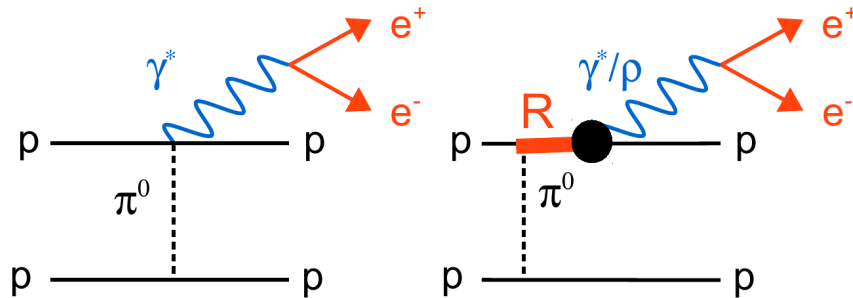
Figure 2.1: Proton-Proton reaction with OBE. Left side shows the direct coupling of the virtual photon to the vertex, left side the excitation of a resonance. For details see text.

is likely because of VMD. A clear drawback of the OBE approach is the large number of diagrams which have to be calculated and uncertainties in adjusting the parameters of the theory. At this energy, which is below the η production threshold, the dielectron production has two main sources: Dalitz decays of π^0 and of $\Delta(1232)$ resonance. Furthermore, a contribution from non-resonant nucleon-nucleon bremsstrahlung is present. In Figure 2.3(a) the p+p dilepton

---

[4]decay width is in the same oder as the mass

invariant mass spectrum is compared to the HSD[5] model. Similar comparisons are shown in [A^{+}10c, Gal09]. The p+p results have been successfully described by various model calculations. To understand isospin dependence of the particle production (quasi-free) neutron+proton (n+p) collisions have been measured. The neutron is quasi-free because the measurement was performed with a deuteron beam and proton spectator tagging with the Forward Wall. In Figure 2.3(b) the dilepton invariant mass distribution from the n+p collisions is shown.

Sub-threshold η production is possible as additional energy is provided by relative motion of the proton and neutron in the deuteron. The dilepton invariant mass spectrum shows a significantly higher yield in the region M_{ee} >300 MeV/c^2. A qualitative explanation was given by possible charged boson exchange and off-shell production of dileptons in the internal lines (See

Figure 2.2: Exchange of charged bosons within the OBE

Figure 2.2) [KK06]. The quantity of that contribution was better described in [SM10]. Adding even higher-order diagrams, where there creation of 2 resonances is possible, seemed to solve the discrepancies finally [BC14].

(a) Proton+Proton

(b) Proton+Neutron
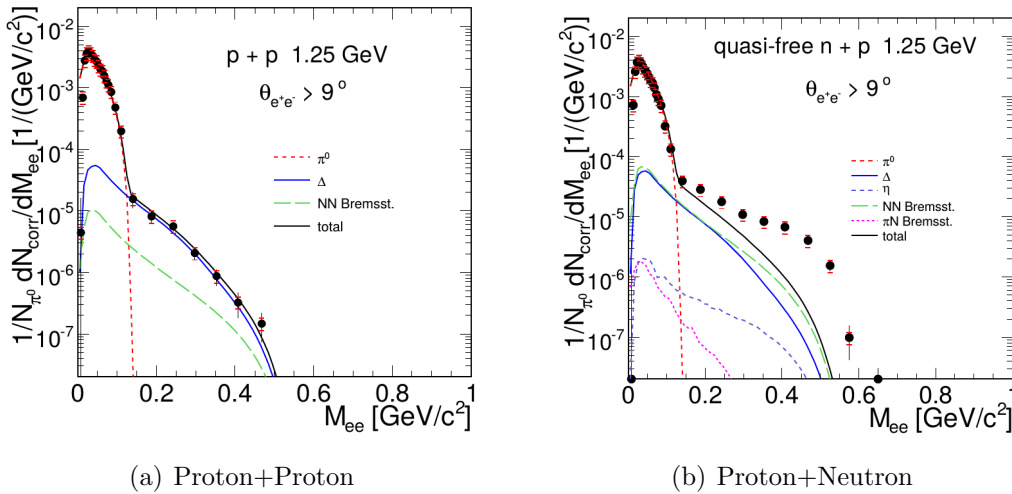
Figure 2.3: Invariant e^+e^- mass distribution measured in p+p (a) and pn (b) interactions at a beam energy of 1.25 GeV, together with HSD calculations: Red dashed line: π^0-Dalitz decay, blue solid line: Δ^+ Dalitz decay, purple dashed line η-Dalitz, green dashed line: NN bremsstrahlung, pink dotted line: πN bremsstrahlung, black solid line: total cocktail.

---

[5]HSD version from October 2007 including NN bremsstrahlung is used here

2.2 Eta production at p+p 2.2 GeV and p+p 3.5 GeV

The η production in the p+p reaction at 2.2 GeV was studied with HADES in three different decay channels: $\eta \to \pi^+\pi^-\pi^0$, $\eta \to \pi^+\pi^-\gamma$ and $\eta \to e^+e^-\gamma$ [Cav06, Spa05, Rus06]. The results show that the η meson produced via an intermediate N*(1535) resonance, analogous to Figure 2.1. This result confirms the DISTO [B+04b] measurement. Knowing the energy of the colliding protons and measuring the charged pions, the missing mass technique was used to reconstruct the η in the $\eta \to \pi^+\pi^-\pi^0$ decay channel (Shown in left hand panel of Figure 2.4). The dilepton invariant mass spectrum, constructed by using only dilepton pairs that are emitted from η meson decays, is shown in the right hand panel of Figure 2.4. The dilepton spectrum is compared to simulations using either QED or VMD form factors. The data favors the VMD from factors but is not conclusive. In
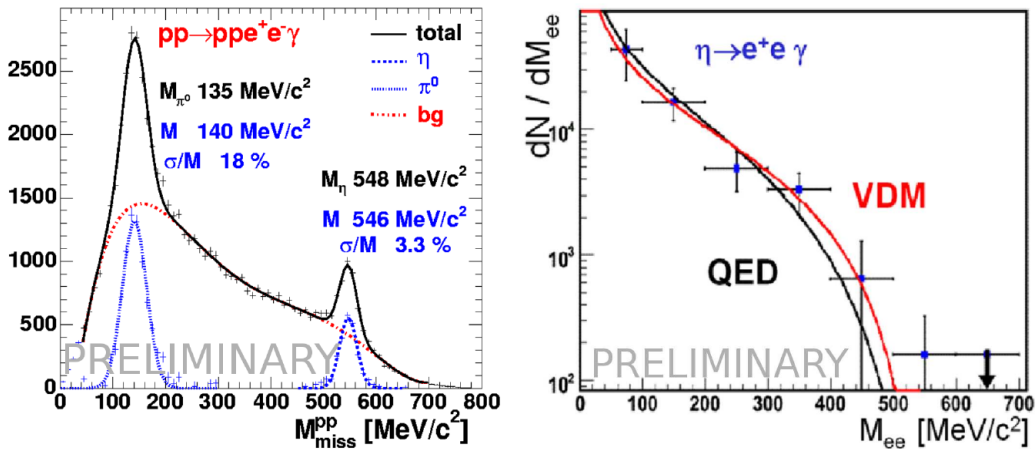
Figure 2.4: Form Factor of η meson measured in p+p at 2.2 GeV with HADES. Left: Proton-proton missing mass plot for electromagnetic η meson decay, after a kinematic refit procedure. Right: Invariant mass distribution of dielectron pairs coming from η decay, after the conversion rejection, in comparison with simulation by using QED or VMD η form factor [Spa07].

the proton+proton 3.5 GeV measurement campaign, η was reconstructed in the Dalitz-decay channel $\eta \to e^+e^-\gamma$ [Tar10], as well as in a three pion $\eta \to \pi^+\pi^-\pi^0$ [Tei11] channel. In Figure 2.5(a) the proton proton missing mas is shown without (black) and with (red) a kinematic refit. The usage of the refit increased the resolution and improved the signal to background ratio. Besides the η meson the ω meson is visible as well. The reconstructed η mesons are combined with measured protons to $M_{p\eta}^2$, and compared to simulations which include resonance production of the η. While the pure phase-space simulation (purple) can not describe the measurement, while the inclusion of the N*(1535) leads to a good agreement with the data. This picture confirms previous measurements.

(a) pp missing mass

(b) $\text{M}^2_{p\eta}$
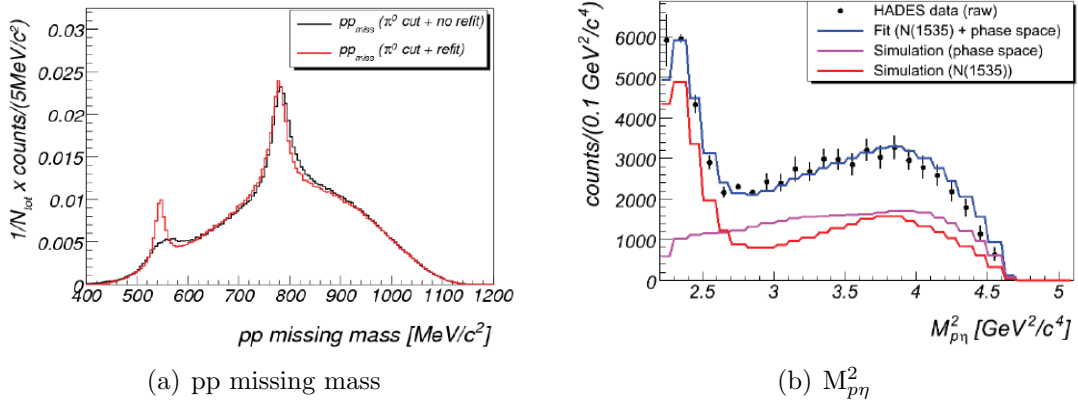
Figure 2.5: Results form proton+proton 3.5 GeV measurements in the $\eta \rightarrow \pi^+\pi^-\pi^0$ channel[Tei11].

2.3   Eta production in p+^{93}Nb at 3.5 GeV

The production mechanism of the η meson seems to be understood in p+p collisions. Nevertheless, the influence of the presence of nuclear matter on the production is not fully clear. To distinguish cold nuclear matter effects from changes due to a (fully) thermalized system, proton reactions with nuclear targets are measured. HADES measured proton on ^{93}Nb collisions at an energy of 3.5 GeV. The reconstruction of the neutral mesons using the full conversion method are shown in [ABB$^+$13] (More details in Section 8). In Figure 2.6 the 4 lepton invariant mass spectra together with the event mixing background (red) is shown. Both mesons are clearly visible.
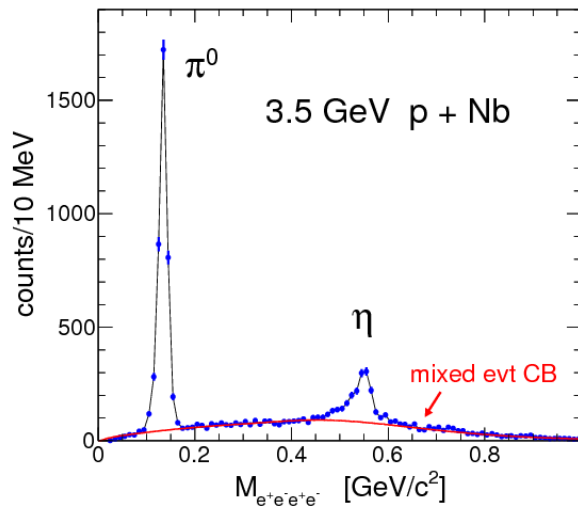
Figure 2.6: Uncorrected four lepton invariant mass $M_{e^-e^+e^-e^+}$ spectrum measured in p+^{93}Nb at 3.5 GeV

15

Furthermore, rapidity and $p_\perp$ spectra were reconstructed and compared to various transport calculations. The transport models will be explained in detail in Section 4. The π^0 production (Figure 2.7, left) is described by all models with discrepancies in the order of 10-25% in both observables. The rapidity distributions of all models are comparable to the measured ones, but with a slight shift towards target rapidity. On contrast, distributions from the η meson (Figure 2.7, right hand panel), show larger discrepancies between the models. While UrQMD reproduces the transverse momentum distribution quite well, the accepted yield is underestimated by a factor of 2-3. The shape of the rapidity distribution is also not well described. Both versions of GiBUU describe the rapidity distribution; the integrated yield and the extended-resonance implementation also agrees in the transverse-momentum. The HSD pion and eta yields do agree fairly well with the data, but their rapidity and transverse momentum distributions deviate substantially.

Missing data of the η production channels in this energy range can explain why the models tend to perform worse for η production than they do for π^0. The data from the p+^{93}Nb measurement is able to improve the models here.
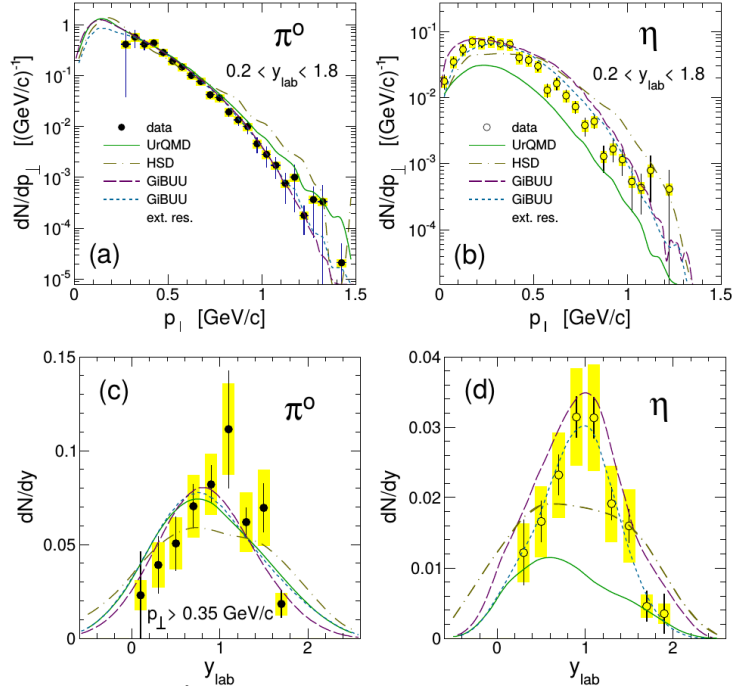

Figure 2.7: Upper row: π^0 and η transverse momentum distributions per minimum-bias event in 3.5 GeV p+^{93}Nb reactions (symbols) compared to results of the UrQMD, HSD, and GiBUU transport models. Lower row: π^0 (for $p_\perp$ >0.350 GeV/c) and η rapidity distributions per minimum-bias event compared to transport calculations.

3   Meson production in Heavy-Ion Collisions

Besides production of mesons in elementary reactions, meson formation in heavy-ion collisions is of great interest. While the production of π^0 in elementary reactions is mostly driven by decay of the $\Delta(1232)$ resonance, the η meson is produced by the decays of the much heavier N*(1535) resonance. Measuring the η and π^0 multiplicities in heavy-ion collision gives direct access to baryonic resonances and modification of their production rates due to in-medium effects. Theoretical models [VPS$^+$08, EvHWB15, GHR$^+$16, RW02] show, that baryon dominated matter is created in heavy-ion collision of a few GeV, which is the energy regime of the SIS18 accelerator at GSI. In the following π^0 and η production in heavy-ion collisions at low energies will be shown. Four experiments located at GSI are contributing to the systematic measurements. The Two Arm Photon Spectrometer (TAPS) was specifically designed for the reconstruction of neutral mesons in their two photon decay. The kaon spectrometer KaoS and the large acceptance FOPI spectrometer measured charged hadrons with a high precision and finally the HADES spectrometer also measures electron pairs.

3.1   Heavy-Ion Accelerators

Nowadays the best experimental tool to create and access high temperatures and densities of strongly interacting matter are heavy-ion collisions at relativistic energies. One can distinguish between so called *collider* experiments, where two beams of ions are crossed within a detector, and *fixed-target* experiments, where one beam hits a stationary target. Fixed target experiments are traditionally used to generate high net-baryon densities, whereas collider experiments are used to deliver very high energies and reach lower baryochemical potentials. Figure 3.1 shows the accessible regions of these accelerators in the phase diagram of nuclear matter. In these facilities different elements are ionized and then accelerated towards high velocities ($0.9c$ (SIS18) to $0.999c$ (LHC)). This acceleration process will be explained based on the example of the GSI facility in Section 5.
After the first successful collisions at the LBNL[6], Berkeley (USA) and at the JINR[7], Dubna (USSR) in the mid 1970's, various accelerator facilities were built. Ultra relativistic high energy experiments at LHC[8], CERN, and the RHIC[9], BNL, focus on studying the region of vanishing baryochemical potential, where the QGP is created. At RHIC the beam energy scan phase I was performed in 2010 and 2011, in order to search for the critical point, which would occur if the phase transition to QGP is a first order type. The accelerator facilities SPS[10] at CERN

---

[6]Lawrence Berkeley National Laboratory
[7]Joint Institute for Nuclear Research
[8]Large Hadron Collider
[9]Relativistic Heavy-Ion Collide
[10]Super Proton Synchrotron

and the AGS[11] at Brookhaven National Laboratory access the region of higher baryochemical potential and experiments at SPS saw deconfined matter for the first time [HJ00]. In the future SIS 100/300 at the FAIR Facility will investigate that region as well, using rare and penetrating probes. Furthermore, RHIC plans a complementary fixed target run. Even lower temperatures and higher net-baryonic densities are achieved at the BEVALAC [GHL71] and current (GSI[12]) SIS 18 accelerators.
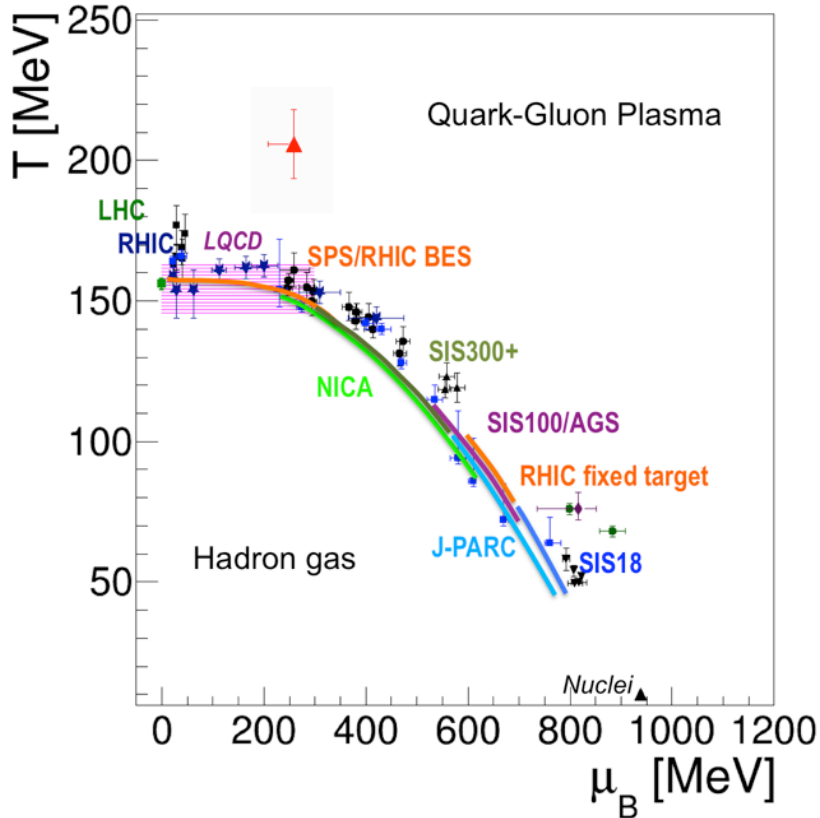
Figure 3.1: QCD phase diagram with indicated accelerator facilities. The data points are measurements of freeze-out parameters from various experiments. In the shaded area lattice QCD calculations are possible.

3.2   Parameters of a Heavy-Ion Collision

Since ions are extended objects, multiple nucleon-nucleon interactions can take place within the overlap region of the colliding nuclei. The overlap region is a key parameter, called centrality. It is defined by the impact parameter (b), which the distance between the centers of the two colliding nuclei. When an experiment

---

[11]Alternating Gradient Synchrotron

[12] GSI Helmholzentrum für Schwerionenforschung GmbH

measures all possible impact parameters from $0 < b < b_{max}$, the collision are called minimum bias. The centrality is often characterized in terms of the number of participants (A_{part}), which is number of nucleons that undergo at least one collision. Another observable, that is closely related, is the number of binary collisions among nucleons from the two nuclei (N_{coll}). The nucleons that do not participate in any collision, called *spectators*, essentially travel undeflected close to the beam direction. In general, a heavy-ion collision in the low energy regime can be separated into three stages (illustrated in Figure 3.2). Virtual photons are emitted from all stages, and the measured dilepton spectra is an integration over all this stages. At the very beginning of a collision, binary nucleon-nucleon collisions occur. Measurements of elementary p+p and p+n collisions, which are described in the previous chapter, can be used to extract information of the contribution of these early processes to the spectrum. Then a hot and dense stage (the so-called fireball) occurs. In the SIS18 energy regime the fireball exists for about 10-20 fm/c [GHR$^+$16] while it expands and cools down. Finally, the system can be found in chemical and thermal equilibrium, signalizing the end of the heavy-ion collision. In the last stage (freeze-out) hadrons are formed. At the SIS18 energy regime three mesons (π^0, η and ω) contribute to the dilepton invariant mass spectrum. These mesons have a very long life time compared to the lifetime of the fireball. The heaviest of the three mesons is the ω meson with
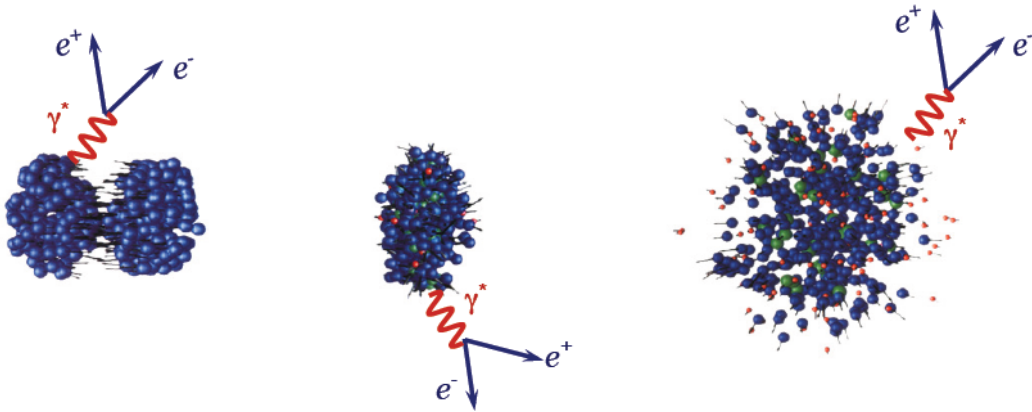
Figure 3.2: Sketch of a heavy-ion collision (^{197}Au+^{197}Au at 1 GeV/u) simulated with UrQMD [B$^+$98]. Three stages of the heavy-ion collision are shown. Lepton pairs emerging from virtual photons are indicated for each stage.

a mass of $M_\omega = 782$ GeV/c^2. In contrast to the two other mesons, the Dalitz decay of the omega, $\omega \to \pi^0 e^+ e^-$, contains a pion but not a γ. This work focuses on the reconstruction via γ conversion. Therefore, and because of the low number of omega's that is produced in the intermediate mass region (factor 100 smaller than from the η meson) the ω meson is not a topic of this work.

3.3   Results from TAPS and KaoS

TAPS has measured π^0 and η in heavy-ion collisions at various beam energies and for different collision systems [ea97, AHMS03, W+98, BPS+94, A+97, SP+94, M+97, M+99]. In Figure 3.3 the multiplicities of the π^0 and η mesons are shown, which follow excitation functions that are shown as colored lines. The energy dependence of the excitation functions is identical for the individual particle species and independent of the used collision system. The π meson production scales nearly linearly with the energy, independent of their isospin state. In the ^{197}Au+^{197}Au collision the positively charged pions show slightly smaller yields compared to neutral pions, due to isospin effects [DV66]. KaoS measured charged meson production as a function of A_{part} [Sen]. The flat behavior of the charged (and therefore also the neutral) pions as a function of A_{part} was established with that measurement. Both behaviors show that pion production is dominated by Δ resonance decay and low-mass ρ excitations, and possibly bremsstrahlung processes. The η meson yield, on the other hand, rises stronger compared to the π^0 yield with the energy, due to different production mechanisms. The decay from heavy resonances, known from elementary processes, is the dominant production
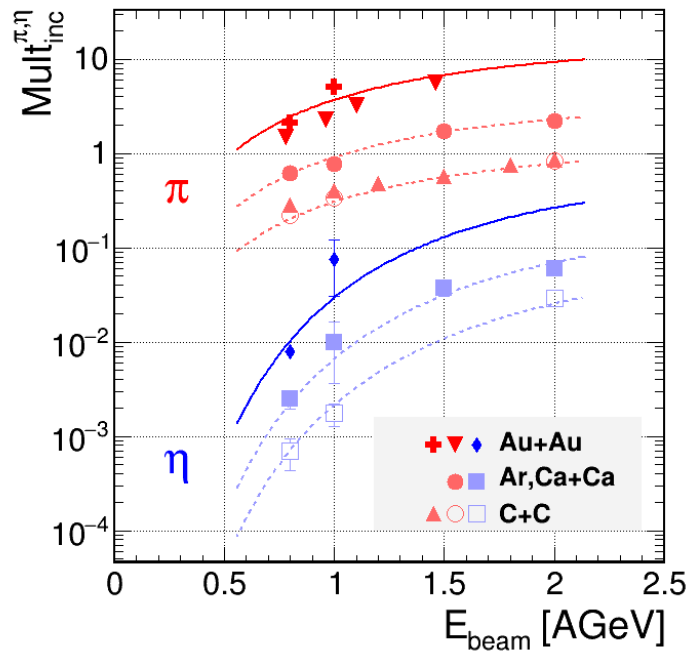
Figure 3.3: Production cross section for different systems and energies measured with the TAPS. The red symbols show the π and the blue the η yields. Triangles show the charged pion measurement from KaoS in ^{12}C+ ^{12}C and ^{197}Au+^{197}Au (upside down). The open symbols are the measurements in ^{12}C+ ^{12}C reactions. Closed red closed circles are π^0 measured in Ca+Ca, and the blue closed squares are the respective η multiplicities. The red crosses are neutral pions from ^{197}Au+^{197}Au collisions and blue diamonds the corresponding η multiplicities.

channel in this range. In ^{197}Au+^{197}Au the η meson yield was only measured at two different energies. Both measurements have large systematic errors. Additional measurements for this collision system are essential to verify if the assumed production mechanisms are valid in this heavy system.

3.4   Results from HADES

Besides the reconstruction of charged pions HADES has performed various dilepton measurement in heavy-ion collisions. The smallest system measured is ^{12}C+ ^{12}C at 1 and 2 GeV/u. The reconstructed dilepton spectra are compared to a hadronic cocktail of π^0, η and ω, created with the PLUTO event generator [F$^+$07]. For the η meson the measured azimuthal anisotropy as well as the transition form factors are included in the model. While the cocktail describes the region of the π^0 ($M_{ee} < 0.150$ GeV/c^2) within the systematical errors, the region of the η meson ($M_{ee} = 0.15$ - 0.50 GeV/c^2) clearly diverges from the cocktail. Adding contributions from the $\Delta(1232)$ resonance and the ρ decay pushes the cocktail closer to the data but still does not completely describe it. The overshoot in the region $M_{ee} = 0.15$-0.50 GeV/c^2 is called the dilepton excess N_{exc}. This excess was measured by the DLS experiment as well [P$^+$97].
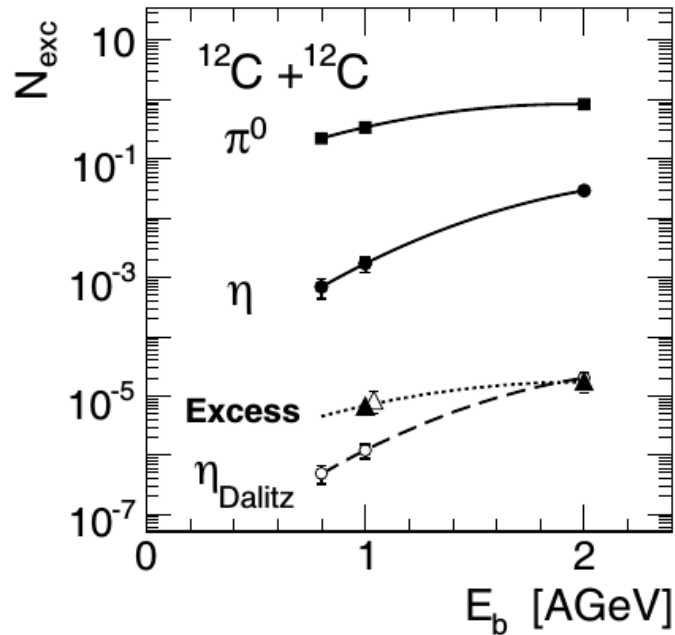
Figure 3.4: Inclusive multiplicity of the pair excess (N_{exc}) as function of bombarding energy E_{kin} (full triangles: HADES, open triangle: DLS). π^0 and η inclusive multiplicities from in ^{12}C+ ^{12}C collisions [ea97] (full squares and circles), as well as the corresponding η-Dalitz decay contribution (open circles) are shown as well. The shown η yield is the integration of the data in the region $M_{ee} = 0.15$-0.50 GeV/c^2. For comparison with N_{exc}, scaled-down π^0 (dotted) and absolute η-Dalitz (dashed) lines are shown [ea08].

Figure 3.4 shows this excess as function of beam energy together with the inclusive multiplicities of π^0 and η measured by TAPS. The TAPS data is fitted with excitation functions, which is discussed previously. Furthermore, the known branching ratio $\text{BR}_{\eta \to \gamma e^- e^+} = 0.6\%$ is used to visualize the η-Dalitz contribution of the invariant mass spectra in the range of $\text{M}_{ee} = 0.15\text{-}0.50$ GeV/c^2. For a better comparison the π^0 excitation function is scaled down to match N_{exc} multiplicity at 2 GeV/u. This shows that the excess scales with bombarding energy like pion production, rather than the production of the much heavier η meson, which suggests a similar production mechanism for π^0 and the dilepton radiation from the excess. System size effects are investigated by measuring dilepton production in ^{40}Ar+KCl collisions at 1.765 GeV/u. To be independent from the TAPS measurement and also to decrease systematic uncertainties resulting from to different detector acceptances and efficiencies, the HADES collaboration started to extract the multiplicities of the neutral mesons with their own detector. To do so, the conversion method is used to extract the π^0 and η multiplicities [HG13]. In Figure 3.5 the four-lepton invariant mass spectrum after subtraction of the event-mixed background is shown. Due to the statistical limitation of the data set a phase space dependent analysis is not possible. The extracted multiplicities are $\text{Mult}_{\pi^0} = 2.0 \pm 0.5$ and $\text{Mult}_{\eta} = 0.047 \pm 0.014$ and agree with the TAPS data.
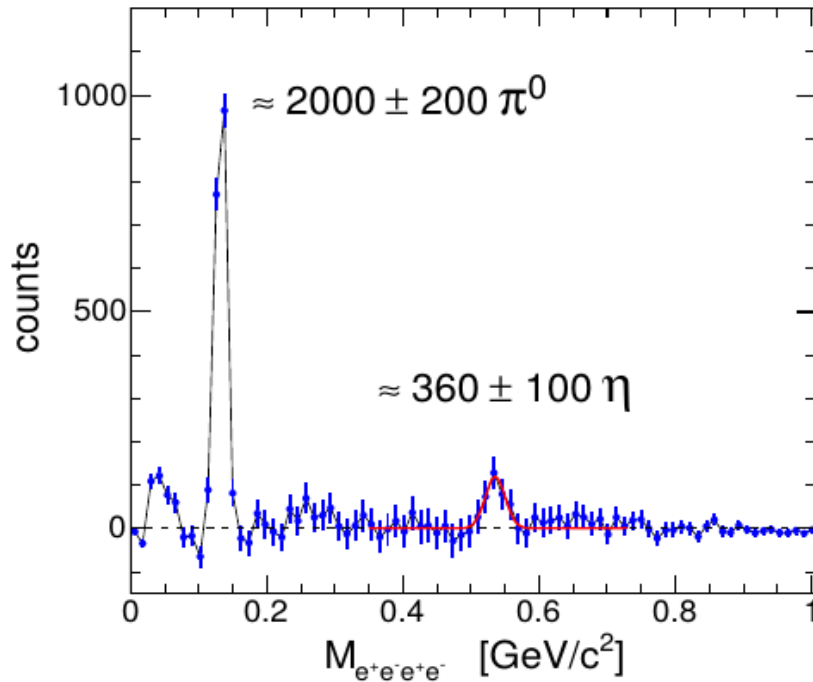

Figure 3.5: Four lepton invariant mass $M_{e^- e^+ e^- e^+}$ spectrum in ^{40}Ar+KCl [HG13]

4   Theoretical Approaches and the Interpretation of the Excess

Due to the complexity of heavy-ion collisions, results of measurements often need to be interpreted with the support of theoretical models. In general one can distinguish between models that describe global parameters of the system like volume, temperature and μ_B, and microscopic descriptions that treat ions as sum of their nucleons and try to understand the space-time history of the collision. Both descriptions have shown their validity in the past and also hybrid models, combining advantages of both, are emerging. The data obtained in this work will be compared with both types of models in Section 14.1.

4.1   Statistical Hadronization Models

Statistical models [BMRS03, Taw14, Flo14] are well-established methods to describe the hadron production in heavy-ion collisions. These models describe particle production in thermodynamic ensembles. Thermodynamic ensembles can be divided in micro canonical (N,E,V), canonical (N,T,V) and grand canonical (μ_B, T, V) [Gib10], where N is the number of particles, E the energy, V the volume, T the temperature and μ_B the chemical potential of the system. For the description of heavy-ion collisions, the grand canonical ensemble is used, which leads to a prediction of the particle multiplicity as function of μ_B, T, V, or vice versa the extraction of those parameters from the measured particle yields. The points shown in Figure 3.1 are freeze-out parameters which have been extracted by fitting these models to the measured particle yields. The freeze-out parameters show a regularity that has been widely interpreted as a hint that (local) chemical equilibrium is achieved at the end of heavy-ion collisions. If the average energy per hadron drops below 1 GeV, chemical freeze-out will happen [CR98]. In case of rare particles (multiplicity $<$ 1) the canonical ensemble is used, since particle production needs to be conserved exactly. In the SIS18 energy regime all particles that contain strangeness are produced rarely and therefore the strangeness suppression is introduced by a strangeness correlation radius R_c.
One of the questions emerging is, to what extent a hadronic system, created in a low energy heavy-ion collision can be described in terms of chemical and thermal equilibrium. The TAPS collaboration interpreted their results on π^0 and η production [W+98, BPS+94, A+97, SP+94, M+97, M+99] with a thermal model [AHMS03]. Simulations from [CEKS98, COR99] showed an agreement of proton, deuteron, charged pion, and kaon multiplicities with a chemical equilibrium at freeze-out. Nevertheless, they were not able to describe the η production. The results of the TAPS measurement show that the inclusive π^0 and η meson yields are consistent with the formation of a hadronic fireball in chemical equilibrium. With increasing the bombarding energy μ_B decreases from 800 MeV to 650 MeV and the temperature T increases from 55 MeV to 90 MeV. The baryochemical

potential grows with increasing mass system size while T remains nearly constant. On the other hand, no centrality dependence of the parameter has been found, while investigating the system ^{197}Au+^{197}Au at 0.8 GeV/u. Using the statistical

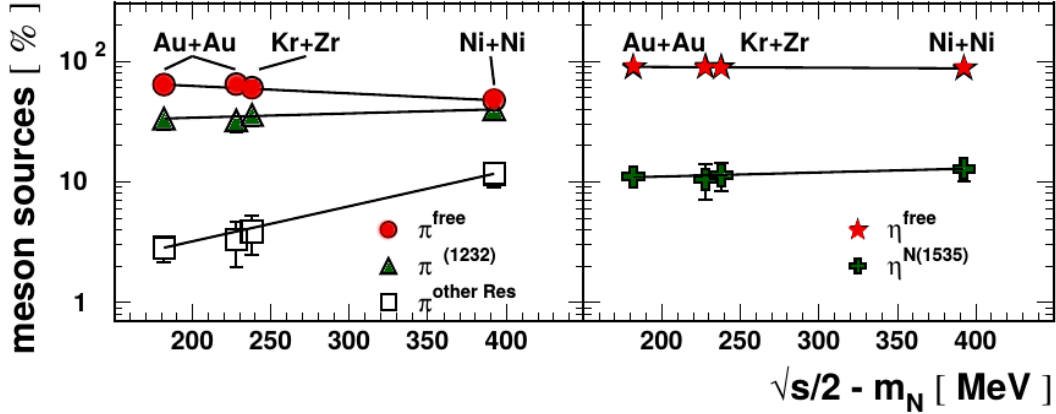Figure 4.1: π^0 (left) and η meson sources (right) at chemical freeze-out in the hadron-gas model. The mesons are either bound in resonances or already free. The relative contributions are shown as a function of the energy available per baryon. The error bars show the uncertainty of the used freeze-out parameters μ_B and T. Straight lines are drawn to guide the eye.

model, also the extraction of the chemical properties of the fireball is possible. The mesons can be present either as free particles, or still bound in baryonic resonances (see Figure 4.1). The amount of free pions decreases slightly with energy, but is never bigger than 65%, which means that always about 1/3 of the pions measured in a heavy-ion collision is still part of a resonance at the freeze-out point. In most of the cases it is hidden inside the $\Delta(1232)$ resonance, but with increasing energy also heavier resonances become important. The η production shows no resonance decay after chemical freeze-out, which is unexpected.

The hadron yields obtained from the ^{40}Ar+KCl measurement campaign from HADES were fitted with the THERMUS code [WCH09]. Here for the first time more than ten particle species [A$^+$11b, SL15, T$^+$09, A$^+$09a, A$^+$10b, A$^+$13, A$^+$11a, A$^+$09b] were fitted simultaneously. The following values for chemical freeze-out parameters were found: T = 70 ± 3 MeV, μ_B = 748 ± 8 MeV. A comparison of the data with the statistical model fit is shown in Figure 4.2. The lower part of this figure depicts the ratio of data and fit. All measured particle yields except for the Ξ^- and the η are described with good agreement. The Ξ^- production is discussed in [A$^+$16]. The η meson in ^{40}Ar+KCl is not measured by HADES but extrapolated from TAPS measurements at 1.5 and 2.0 GeV/u [AHMS03] and not included in the fit. The η meson seems to follow different freeze-out criteria compared to the rest of the more abundant particles. Also the parametrization of T and μ_B obtained in [AHMS03], which used mainly π^0 and η yields as input to the statistical model fit, showed values that are systematically higher than

the parameterizations of [CWOR06, ABBM⁺10]. The tension between the observed η production and the results from thermals models seems to come from the clearly different production mechanism in comparison, to i.e. the pions. The baryonic composition of the fireball seems not to be fully understood, and comparing branching ratios of the resonances into Nη also large uncertainties appear. While the N*(1535) had a branching ratio in the order of $42 \pm 10\%$ in the Nη channel, the slightly lighter N*(1520) only decays with a branching ratio of 0.24 ± 0.04 % [O⁺14]. A comparison of the ^{197}Au+^{197}Au measurements to the SHM will address this question as well.
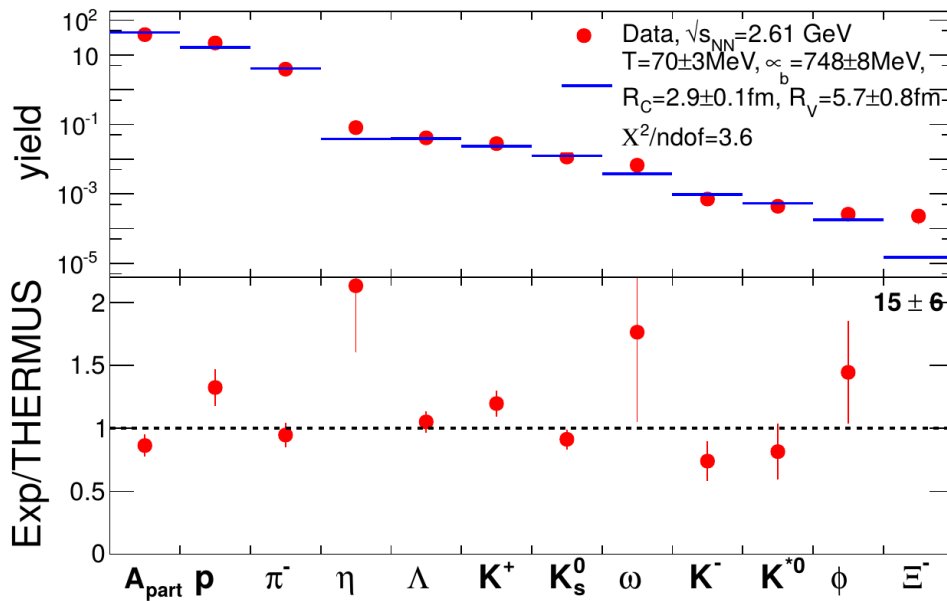
Figure 4.2: The upper plot shows the yields of secondary hadrons in ^{40}Ar+KCl reactions (filled red circles) and the corresponding THERMUS fit values (blue bars) as well as the obtained fit parameters. The lower plot shows the ratio of the experimental value and the statistical model value. For the Ξ^- the ratio number is quoted instead of a point.

4.2   Microscopic Transport Models

A promising approach to understand the fireball evolution with the experimentally observable hadronic final state are transport models. In these models the entire time evolution of the heavy-ion collisions is put into one framework. In microscopic transport models the full space-time evolution of all microscopic degrees of freedom, so in the SIS18 energy regime all hadrons present in the system, is calculated from the initial state to the final freeze-out. At each time step the collision criterion b $< \sqrt{\frac{\sigma_{tot}}{\pi}}$, where b is the impact parameter between two nucleons and σ_{tot} the total cross section, is checked. If the collision criterion is satisfied

the nuclei collide. The particle production cross sections are taken from [O+14]. In this work we will compare mainly with the UrQMD [BZS+99, B+98] transport code. Here, but also in codes like GiBUU [BGG+12] and HSD [EC96], all mesons are created via the decay of baryonic resonances. A drawback of this approach is the dependence on an extended set of input parameters (decay branching ratios, production cross sections, electromagnetic form factors). In addition some of these parameters are not constrained by data or theoretical approaches. The meson multiplicity simulated in UrQMD is compared to the experimental results of heavy-ion collisions [Beh11] in Figure 4.3. The η production is significantly underestimated by the model, for $^{12}C+$ ^{12}C collisions. In $^{40}Ar+KCl$ the model is closer to the data, but still does not describe the yield. This discrepancy can be connected, again, to question of the production of the η meson only via the decay of the N*(1535).
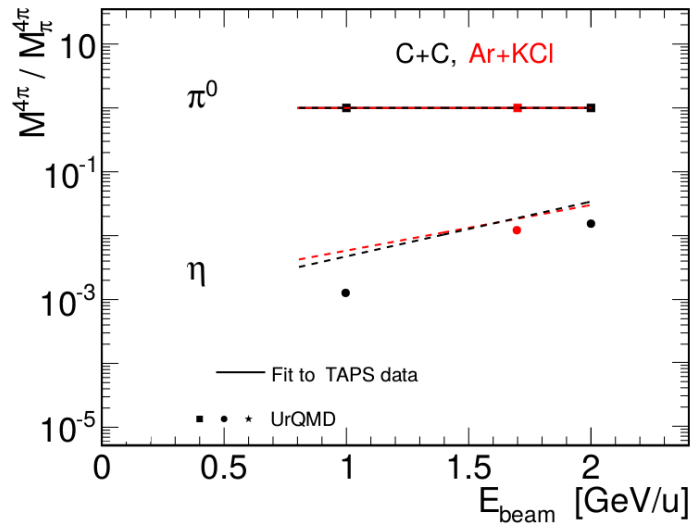
Figure 4.3: Simulated π^0 and η meson multiplicities (points) as function of as function of beam energy, together with fit to the TAPS data (lines) [W+98, BPS+94, SP+94, M+97, M+99], for $^{12}C+$ ^{12}C (black) and $^{40}Ar+KCl$ (red). All multiplicities are normalized to the number of π^0.

4.3   Interpretation of the Dilepton Excess Yield

Already in the dilepton measurement in $^{12}C+$ ^{12}C at 1 [ea08] and 2 GeV/u [ea07] an overshoot over the expected contribution from the η meson was measured. The η component is estimated using the average between the TAPS data at 1 and 2 GeV (see Figure 3.3). After the subtraction of the η component. The $^{12}C+$ ^{12}C data were compared to a superposition of p+p and n+p collisions (see Figure 4.4(a)). After normalization to the π^0 yield all data set agree within errors and

can therefore be interpreted as a superposition of binary nucleon-nucleon colli-
sions [A$^+$10c]. The same comparison is done for the ^{39}Ar+KCl measurements
at 1.765 GeV/u (shown in Figure 4.4(b)), where an enhancement over the triv-
ial sources was measured [A$^+$11a]. Consequently, in contrast to the ^{12}C+ ^{12}C
system, ^{40}Ar+KCl can not anymore be seen as a superposition of independent
NN collision. Multi-body and multi- step processes and maybe even in-medium
modifications of the involved hadrons are required to interpret the measurement.
The enhancement in the 0.150 GeV/c^2 < M_{ee} < 0.500 GeV/c^2 is the so-called
low-mass dilepton *excess* and is the first evidence for medium effects measured at
such low energies. It scales similar to the π^0 with beam energy and exponentially
($A_{part}^{1.4}$) with the system size. Such behavior has been interpreted as being charac-
teristic of a production mechanism not driven by low-energy processes like pion
production and propagation involving the Δ and, maybe, even low-mass ρ excita-
tions as well as bremsstrahlung. For further investigations HADES measured the
lepton yield in ^{197}Au+^{197}Au at 1.23 GeV/u as well. These lepton measurements
will be show and discussed in Section 15.

In this context it is important to pin down the contribution of the η meson to the
dilepton yield obtained in ^{197}Au+^{197}Au. The measurements of TAPS data suffer
from large uncertainties, which will be directly transfered in the uncertainty of
the excess. Therefore, and to be independent of the TAPS measurements, the
goal of this work is to extract the η multiplicity. Since the π^0 can be measured
with the same methods, but also independently crosschecked with charged pions,
it will be used to understand systematics.
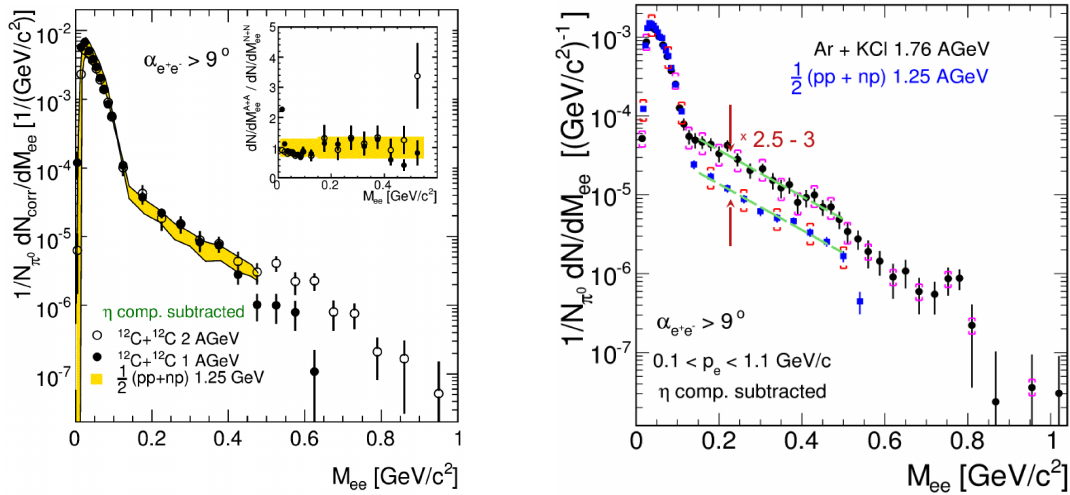
(a) ^{12}C+ ^{12}C at 1 and 2 GeV/u vs.
1/2(pp+np) at 1.25 GeV

(b) ^{40}Ar+KCl at 1.765 GeV/u vs. 1/2(pp+np)
at 1.25 GeV

Figure 4.4: Dilepton invariant mass spectra of heavy-ions collisions compared to
elementary reference. a)^{12}C+ ^{12}C [A$^+$10c] b) ^{40}Ar+KCl [A$^+$11a]

Part II
The HADES Experiment

Science never solves a problem without creating ten more.

George Bernard Shaw

The High Acceptance Di Electron Spectrometer (HADES) is located at the SIS18 at GSI Helmholtzzentrum for heavy-ion research. It is optimized for rare probes meaning, it has a low material budget (Section 10.1), a compact geometry, a fast read out (Section 6.7) and covers a high geometrical acceptance. The spectrometer is build symmetric around the beam-axis, and has nearly full azimuthal angle ϕ coverage and polar angle Θ coverage between $18°$ and 85 °. In Figure 4.5 an exploited view of the spectrometer is shown and all sub-detector systems are indicated.

HADES has the capability to detect leptons and various hadron species, with measurements of time-of-flight, momentum and energy loss (Details see Section 7). For the lepton analysis additionaly the RICH and the SHOWER detector are used. The centrality and orientation of a collision can be reconstructed with the help of a Forward Wall detector. In the following section the sub-detector systems will be explained in detail, and the genreal analysis methods will be given. A complete overview of the detector and further informations are given in [A+09c].
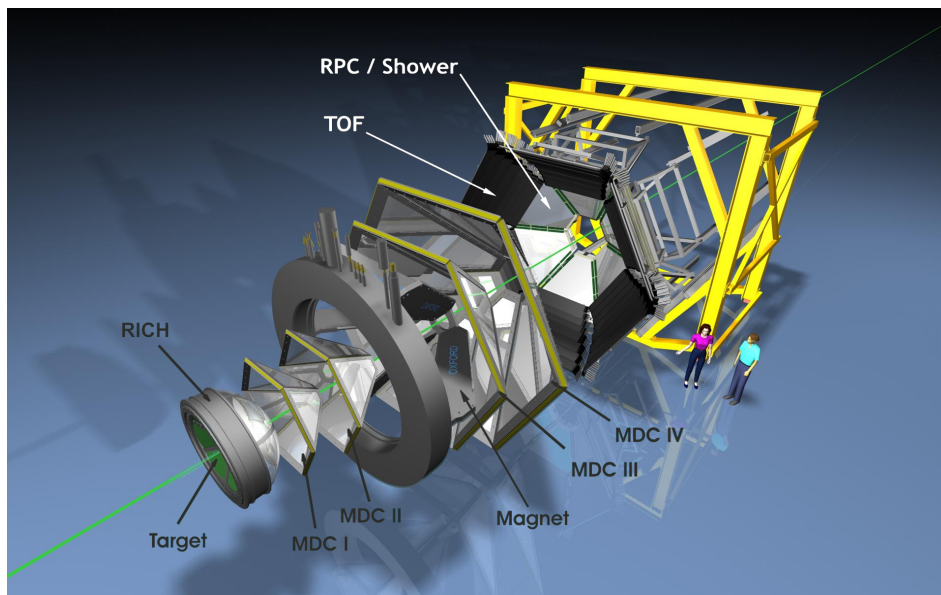

Figure 4.5: Exploited view of the HADES spectrometer. [SS07].

29

5   GSI Accelerator Facility

Besides the heavy-ion program, GSI has various other research pillars like atomic, plasma and biophysics. To serve all those different fields the facility has a large accelerator complex, shown in Figure 5.1. First atoms need to be ionized to be accelerated. This is realized in GSI in four different ion sources: ECR^{13}-, Penning-, Multicusp- and $MEVVA^{14}$-Ionsources [Bro04], located on the left side of Figure 5.1. The ions get pre-accelerated in the $UNILAC^{15}$ [Kru72] to 20% of the speed of light, and are either already used in the Experimental Hall I for creation and study of super heavy elements (atomic number Z >107) or send to the heavy-ion synchrotron synchrotron. The SIS18 (indicated with yellow color) has a circumference of 216 m. An unique feature of this accelerator is the possibility to accelerate most of the existing elements, starting from protons and ending up at heavy-ions like ^{197}Au and even ^{238}U. The SIS18 can serve up to four different experiments with ions that have almost 90% of the speed of light [SEK+10]. GSI has the possibility to store the ions in the experimental storage ring ERS (shown in orange) or use the fragment separator FRS (shown in green). Ions used for the HADES experiment are directly extracted from the SIS18 accelerator and collide with a fixed target located in the Experimental Hall II. In Figure 5.1 HADES is indicated with a pictograph in the lower right. In the future the FAIR facility will extend the current accelerator facilities. Details regarding FAIR will be given in Chapter 16.2.
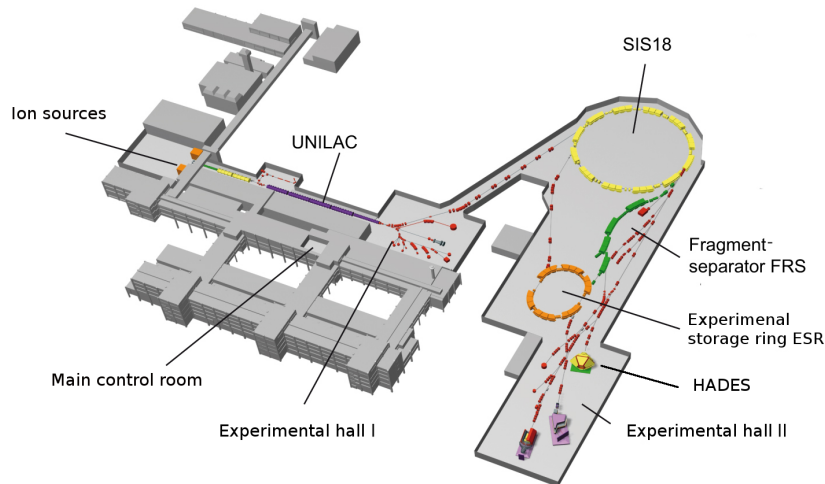

Figure 5.1: GSI accelerator facility

---

[13]electron cyclotron resonance
[14]metal vapor vacuum arc
[15]Universal Linear Accelerator

6 HADES - Experimental Setup

HADES features a wide physics program with several measurement campaigns performed in the past years. Various reactions such as N+N, N+A, A+A, π^-+N and π^-+A at beam energies of a few GeV/u have been measured. In Table 6.1 all measured systems and their collision energies are summarized. Note that for the π-beam campaign in 2014 only the momentum of the beam is given. Details of the π-beam can be found in [LEF$^+$13]. In the years 2010-2012 the spectrometer was upgraded to handle higher multiplicities expected from larger collision systems, such as ^{197}Au+^{197}Au. Besides the replacement of the data acquisition (DAQ) and the read out electronics (see Section 6.7), the former time-of-flight system ToFino was replaced by resistive plate chambers RPC (see Section 6.3.2 and [AP$^+$04]). The MDC plane I was renewed as well. In the following the sub-detector systems of HADES will be described. The analysis performed in this work is based on the ^{197}Au+^{197}Au collisions at 1.23 GeV/u, taken by HADES in April 2012.

Year	Collision System	Energy/Momentum
2002	^{12}C+^{12}C	1.0 GeV/u
2004	^{12}C+^{12}C	2.0 GeV/u
2005	^{39}Ar+^{41}KCl	1.76 GeV/u
2006	p+p	1.25 GeV
		2.2 GeV
		3.5 GeV
2007	d+p	1.25 GeV
2008	p+^{93}Nb	3.5 GeV
2012	^{197}Au+^{197}Au	1.23 GeV/u
2014	π^-+^{184}W	1.7 GeV/c
2014	π^-+^{12}C	1.7 GeV/c
		0.659 GeV/c
		0.69 GeV/c
		0.748 GeV/c
2014	π^-+^{28}PE	0.8 GeV/c
		0.659 GeV/c
		0.69 GeV/c
		0.748 GeV/c
		0.8 GeV/c

Table 6.1: HADES measurement campaigns 2002-2014.

6.1   RICH Detector

The hadron-blind gaseous Ring Imaging Cherenkov detector (RICH) is designed to identify electrons and positions and is the innermost sub-detector system. The particle identificationis based on the Cherenkov effect[Che34]. If a charged particle with a velocity $\beta > c/n$, where n is the refractive index, traverses a radiator medium, Cherenkov light is emitted with an angle $cos(\Theta_c) = 1/(\beta \cdot n)$. The layout of the RICH detector is shown in Figure 6.1. It is governed by the need for a low material budget along the particle trajectories, in order to minimize external pair conversion (see Section 10.1), multiple scattering and the limited space between target and tracking detectors. The radiator gas perfluorobutan (C_4F_{10}) offers a suitable to supress Cherenkov threshold (Lorentz factor $\gamma_{thresh} = 1/\sqrt{1-n^{-2}} = 18$) to suppress Cherenkov radiation from muons and hadrons at a momentum p < 1.8 GeV/c. It is enclosed in a thin carbon fiber shell at forward angles (thickness = 0.4 mm) and by the photon detector entrance window made of CaF_2 in backward direction. The produced light is reflected with a spherical mirror (curvature radius R = 872 mm) made out of carbon. The photosensitive CsI cathodes consisting of six Multi-Wire Proportional Chambers (MWPC), are operated with CH_4 and equipped with an individual pad readout. The photon detector is placed upstream of the target to spatially decouple the registration of the Cherenkov light from charged particle tracks emitted from the target. Detail of the read out electronics of the RICH can be found in [KBF$^+$99]. More detailed information on the various RICH components can be found in [Z$^+$99, L$^+$03, FGMKW03, FGH$^+$99].
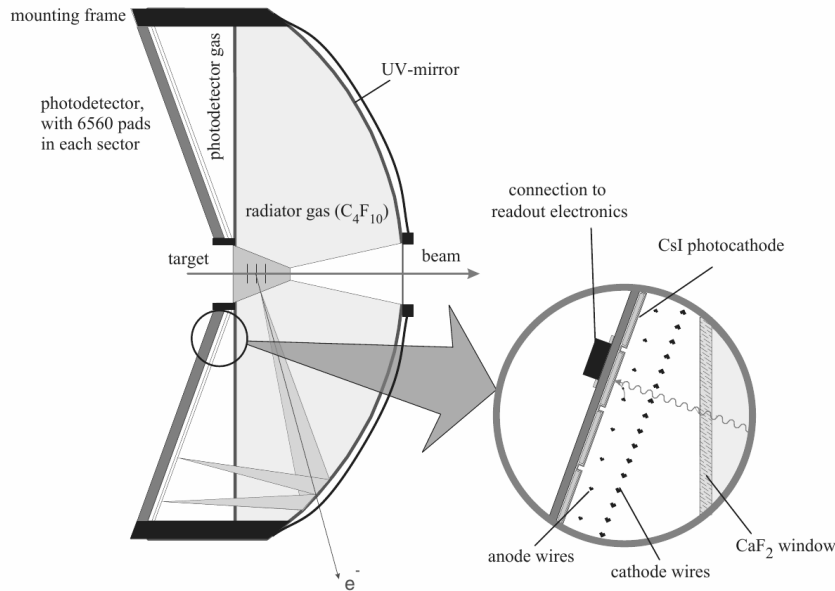

Figure 6.1: Schematic layout of the RICH, consisting of a carbon shell mirror, a CaF_2 window and a photon detector. Figure taken from [Tar10]

6.2   Tracking System

The HADES tracking system consists of 4×6 trapezoidal planar Multiwire Drift Chambers (MDC) symmetrically arranged in six identical sectors surrounding a superconducting toroidal magnet (ILSE). Extended design studies, prototyping and finally the production of the 24 MDCs of four different sizes, were conducted by GSI Darmstadt, LHE/JINR Dubna, FZ Dresden-Rossendorf, IPN Orsay and University of Frankfurt [GKM+98, BBC+02, M+04, KDE+04]. Two planes (I-II) of drift chambers are located in front of, and two (III-IV) behind the magnetic field region (See Figure 6.2(a)). A field-free region around the target, inside the active volume of the RICH detector and inside the MDCs is required.

(a)   (b)
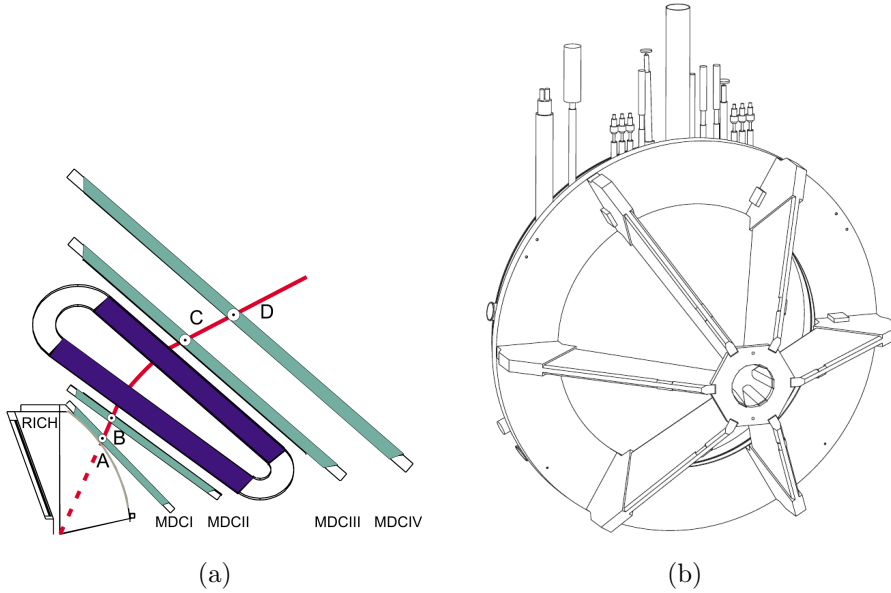
Figure 6.2: Tracking system (a) Schematic layout of the Tracking system. Two planes (I-II) of drift chambers are in front of and two (III-IV) behind the high magnetic field region. A possible track (red) and corresponding vectors (A,BC,D) are indicated. (b)Technical Drawing of the HADES magnet (ILSE)

6.2.1   Magnet

The magnetic field is generated by a liquid helium-cooled superconducting magnet, which is shown in Figure 6.2(b). It consists of 6 coils that surround the beam axis and a circular support structure. Cooling is achieved via single phase ^{4}He at 2.8 bar and at T=4.7 K. The magnetic filed strength inside the coils is $B \approx 3.5$ T; it stays below $B \approx 0.9$ T between the coils. Although the field strength is rather low, super conducting coils are necessary to keep the construction compact [A+09c]. Most importantly toroidal field geometry provides a field-free region around the target and inside the active volume of the RICH.

6.2.2   Multiwire Drift Chambers

The track reconstruction itself is performed by the 24 Multiwire Drift Chambers. Each has the form of a symmetric trapezoid and covers 60° of azimuthal ϕ angle. Four modules form a sector, where the sizes range from 88 cm × 80 cm to 280 cm × 230 cm (height × larger baseline). A module is composed out of six drift cell layers. All layers are oriented in 5 different stereo angles (2 × 0°, ± 20°, ± 40°), to increase the spatial resolution in the polar angle direction (See Figure 6.3(a)). From plane I to IV, the cell sizes increases from 5x5 mm^2 to 14x10 mm^2 to achieve a constant granularity. The total number of drift cells is about 27 tousand. Drift cells consist of 6 cathode wires and 2 field wires. The wires are made out of aluminum (besides Plane IV, which is Au-plated) and have a thickness of 80 μm and 100 μm respectively. The voltage applied to the wires depends on the gas mixture of the chamber and will be investigated in Section 7.1. In Figure 6.3(b) the principle of operation of a chamber is illustrated. Charged particles (shown as arrows) ionize the gas in the drift cells along the track. The created primary electrons cause secondary electrons while drifting and create a so-called cluster. The electron cluster drifts towards the sense wires, where it cause an avalanche, which is finally read out. Furthermore, the created ions induce additional signals to the sense wire. Together with the 12 μm thin entrance foil and the helium-based gas mixtures, the drift chambers are optimized to a minimum radiation length below $5{\cdot}10^{-4}$ X_0. Details of the track reconstruction will be given in Section 7.

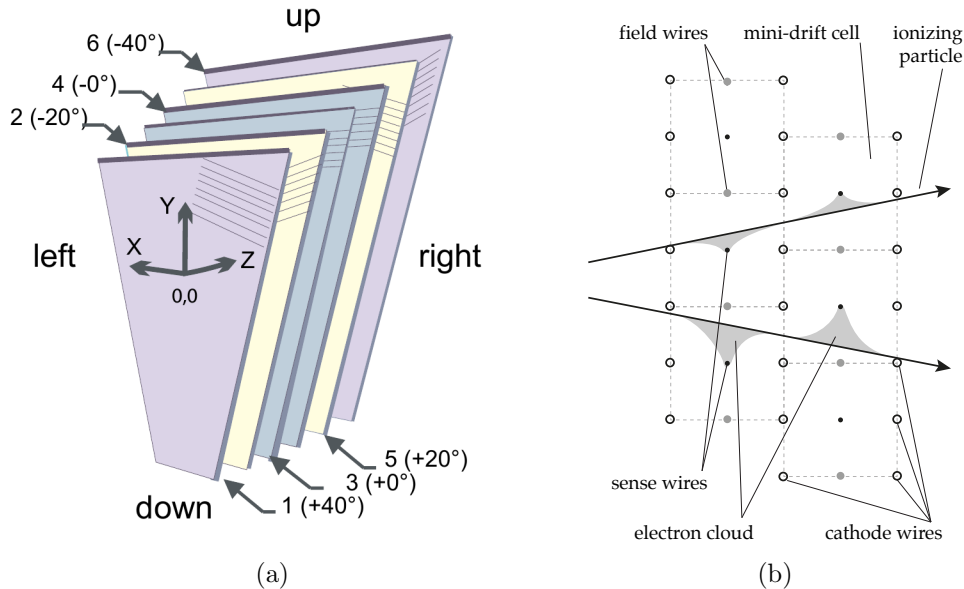(a)   (b)

Figure 6.3: (a) Schematic view of the six anode wire frames inside a HADES MDC, representing the six stereo angles. (b) Schematic drift cells working principle [M$^+$04, Kar15]

6.3 Time-of-Flight and META System

The time-of-flight of produced particles is measured using a diamond counter in located front of the target, giving the start signal, and two scintillator walls. The TOF-Detector covers large polar angles $\Theta = 18° − 45°$ and the resistive plate chambers (RPC) small polar angles $\Theta = 45° − 85°$. Together the detectors from the META[16] system. Besides time-of-flight measurements they are also used for centrality determination of the collision [Kar15].

6.3.1 Start and Veto Detectors

During the beam time in 2012 a set of two beam detectors was used. The start detector, located 2 cm in front of the Au target, is made of mono crystalline diamond material. It has a size of 4.7 mm × 4.7 mm, and a thickness of 50 μm. The thickness of the detector was optimized to keep the interaction probability in the detector material very low. The achieved value is 0.26%. The conducted extensive tests of the diamond material showed that the radiation damage reduces the signal amplitude significantly [PGG$^+$14]. Here is additionally has demonstrated that a heavily damaged diamond detector delivers very fast signals and the precision of the time measurement stays below 60ps (σ). For few week production beam time a dedicated segmentation has been developed. A double sided multi strip detector, shown in Figure 6.4(a) with a thickness of 65 μm and active area of 4.46 mm × 4.46 mm is metalized with 16 front strips and 16 back strips each of width 200 μm and 85 μm spacing between them. The strips are arranged orthog-
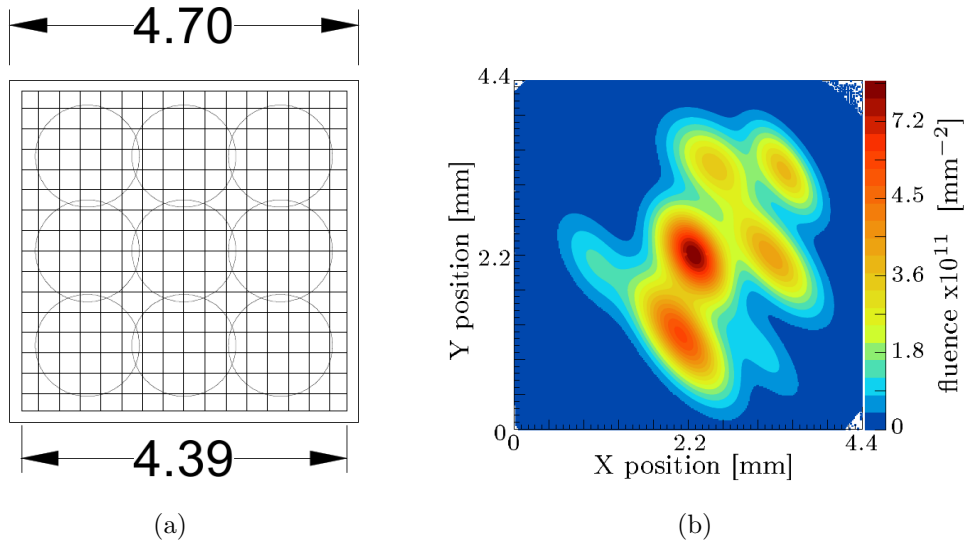

| (a) | (b) |

Figure 6.4: (a) Diamond with 16 x- and 16 y-stripes. 9 disjunct beam spots are utilized on the diamond. (a) Fluence map.

[16]Multiple Electron Trigger Array

onally to provide 256 pixels with dimensions of 285 μm x 285 μm to encode x-y position of each beam ion. The detector is installed in vacuum on X-Y movable holder in order to allow for changes of the detector position when the radiation damage reached a level when the signal amplitude dropped below factor of about 5. During the experiment the detector has been irradiated at seven different positions as visible on the measured fluence map shown in Figure 6.4(b). The Veto detector is made of polycrystalline material, is located 70 cm downstream of the target and has a thickness of 100 μm. The START and VETO detector are used together with the Forward Wall used for the beam alignment process. Further details of the diamond detectors can be found in [PFKW10, PGG$^+$14].

6.3.2   TOF-Detector

The time-of-flight wall consists of 6 identical sectors. Each sector consists out out of 64 strips made out of plastic scintillators, that are grouped together in 8 modules. It covers polar angles between 44° and 85°. The length (L) of the stripes increases polar angles reaches values from 1475 mm to 2365 mm. The segmentation of the detector was chosen such that the probability of a double hit in the same stripe is less than 20% for ^{197}Au+^{197}Au at 1 GeV/u [Sch95]. The time resolutions of the detector is better than 150 ps. For the measurement of charged particles, the scintillation mechanism is used. Charged particles produce light by passing through the detector material, due to the excitation of atoms and their reversion back into the ground state. The produced light travels to photomultiplier tubes at both ends of the strip (called "a" and "b"), where it is converted into an electronic signal and read out. The Amplitude of the signal is called A$_a$ or A$_b$ respectively. The times t$_a$ and t$_b$ are the time interval between the signal generated in the multiplier the time signal from the start detector. The time-of-flight (tof), the position within a stripe (x) and the energy loss (dE) of the particle can be extracted:

$$tof = \frac{1}{2}(t_a + t_b - \frac{L}{v_{group}})\tag{14}$$

$$x = \frac{1}{2}(t_a - t_b) \cdot v_{group}\tag{15}$$

$$dE = k\sqrt{A_a \cdot A_b}e^{L/\lambda_{at}}\tag{16}$$

Here, v$_{group}$ is the group velocity of light in the rod, λ_{at} the attenuation length and k a material dependent Proportionality constant. More details on the time-of-flight measurement are discussed in Section 7.

6.3.3   RPC-Detector

In the inner polar angle region between 18° and 45° the resistive plate chamber (RPC) is installed. RPCs are gaseous parallel-plate avalanche detectors with a time resolutions less than 70 ps. The RPC elements consist out of three aluminum electrodes with glass electrodes in between. Between the electrodes is a 0.3 mm wide gap, which is filled with a standard RPC gas mixture [FP02]. As a result of the small width, high electric fields are created. The RPC system consists out 11116 strip-like RPCs cells, which are located in six sectors. A sector (shown in Figure 6.5(a) is subdivided in three columns, where each column has 32 rows of cells. The stripes are placed in two partly overlapping layers to improve the measurement via redundancy. This geometry gives information on the x and y position of the hit, with a high precision of 10 mm. Details about RPCs in [SC81] and for the HADES RPC in [P$^+$04, K$^+$14].

6.4   Pre-Shower Detector

In the inner polar angles (Θ 18° <45°) the 6 modules of a Pre-Shower detector are installed, placed directly behind the RPC detector. The main task of this detector is to provide an additional separation power for electrons and hadrons at high momentum region. The Pre-Shower detector employs an electromagnetic shower measurement. It consists out of three gas chambers and 2 led converters the are placed alternating. In Figure 6.5(b) lepton identification via electromagnetic shower measurement is shown. A charged lepton (e$^\pm$) passing through the led, emits bremsstrahlungs photons which directly convert into an lepton pair. These new leptons again emit bremsstrahlung and so on. On contrary a $\pi^\pm$ will not create such a shower and can then be rejected in the analysis. The created electron shower drifts trough the gas chambers and induces charge on the
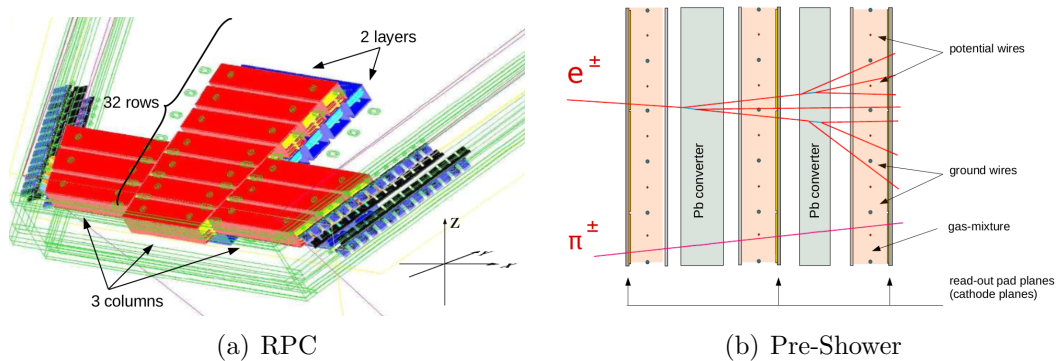

(a) RPC   (b) Pre-Shower

Figure 6.5: (a) Internal structure of a HADES RPC sector and the reference coordinate system. Layers, coulombs and rows and are indicated. (b) Side view of the Pre-Shower detector, with an example electromagnetic shower pattern from a lepton and from a pion.

cathode plates, which are then read out. In contrast to a full calorimeter (as discussed in Section 16.1) the leptons are not stopped completely, so the shower detector is only used for particle detection but not for energy measurements. Further details are given in [B$^+$04a]

6.5 δ-Electron Shield

Knock-out electron, which are also called δ-electrons, are ionizing radiation. They can be caused for example by knockout of orbiting electrons from an atom. Those electrons are background because they are not coming from the heavy-ion reaction, but from Coulomb interactions of highly-charged ions with the target, the veto detector, the mylar exit foil of the RICH and other materials. The shield is used to minimize δ-electrons within the inner MDCs, even so it increases the material budget. It is made out of Polypropylene (C_3H_3), and has a density 0.91 g/cm^3 and an effective thickness of 5 mm. The material is optimized to trade between shielding and additional electromagnetic conversions. Simulations with GEANT give a reduction factor of 3.3 for the inner MDC I and II, from 1.4 e^- per sector to 0.4 e^- per sector [KK$^+$11].

6.6   Gold Target

For the measurement campaign a segmented gold target (shown in Fig 6.6) is used. It is made out of 15 foils with 4.5 mm distance in between. The single foils have a diameter of 3 mm and are placed on kapton stripes, which have a thickness of 7 μm. They are placed on a holder made out of carbon. The segmentation of the target is optimized to minimize external conversions from γ produced in the heavy-ion collision. Due to its emission angle, the interaction with following target stripes is reduced significantly. The same reason motivates the usage of material with low atomic number Z (See Section 10.1).
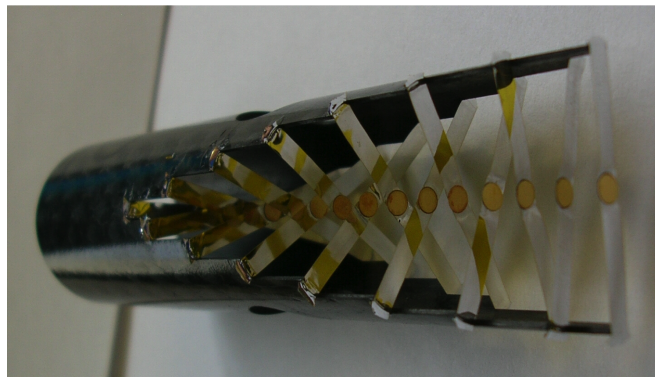

Figure 6.6: Segmented Au target that was used in the APR12 measurement campaign. The Au-foils in the middle are connected by the nearly transparent kapton stripes with the holder.

6.7   Data Acquisition and Trigger

The setup of data acquisition systems (DAQ) is a crucial point in modern nuclear physics. One of the main requirements for rare probes like dileptons is a high interaction rate and therefore a fast data acquisition that can handle a high bandwidth. Additionally, the identification and tracking of particles requires fast and highly granular detectors, that send large amounts of data. Both lead to very high data rates that have to be transported within the read-out system of the detector. In many cases, trigger conditions are set to reduce the amount of data. The HADES setup uses a trigger on a minimum multiplicity in the META system, measured with a coincidence of the start signal. A central trigger ensures that all sub-system are read out simultaneously. Each detector system sends signals which are then processed and digitized by front-end electronics. Afterwards, they are forwarded to a computing farm and prepared for long-term storage, reconstruction, and analysis. In Figure 6.7 the HADES read-out system is shown. For the HADES DAQ upgrade, numerous new electronic modules have been developed. For the ^{197}Au+^{197}Au beam time the typical event rate was 13 kHz, and the resulting data rate was 250 MByte/s. The read-out was handled by four servers sharing the load. details about the HADES DAQ can be found in [Mic12].
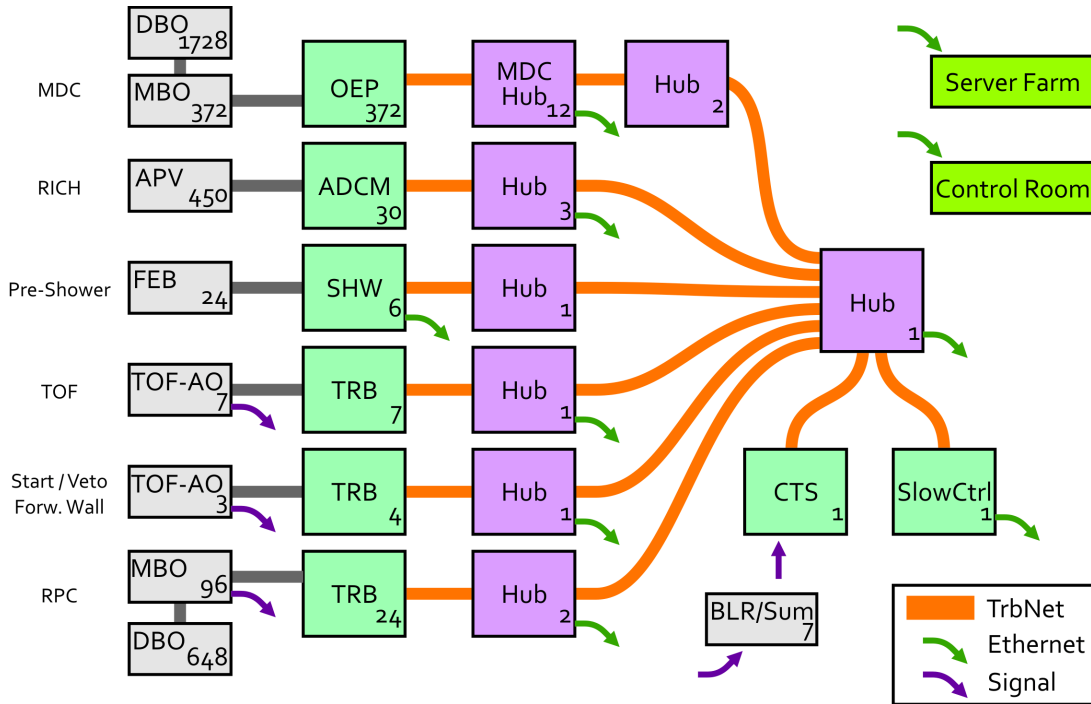

Figure 6.7: A schematic view of the HADES DAQ setup. Color code: Network hubs: purple, read-out boards: green, additional front-end electronics: gray. The small numbers indicate the amount of boards of each type in the DAQ system [Mic12].

7   Particle Identification

In the measured central ^{179}Au+^{179}Au collisions up to 140 charged particles are produced. This corresponds to a double hit probability of $\approx 10\%$ for the MDCs, which is challenging for the track reconstruction algorithms. In Figure 7.1 an event display of a measured ^{197}Au+^{197}Au collision is shown. The magnet coils are visible and can be used for orientation. The other detector components are not shown for clarity. Only fired wires are visible, where the yellow ones are assigned to a track while the cyan ones are not. Reconstructed tracks are shown in green, and their hits in the META system are indicated as yellow points. In the following chapter the steps from the measured signals to the physical observables (β, momentum and dE/dx) are explained.
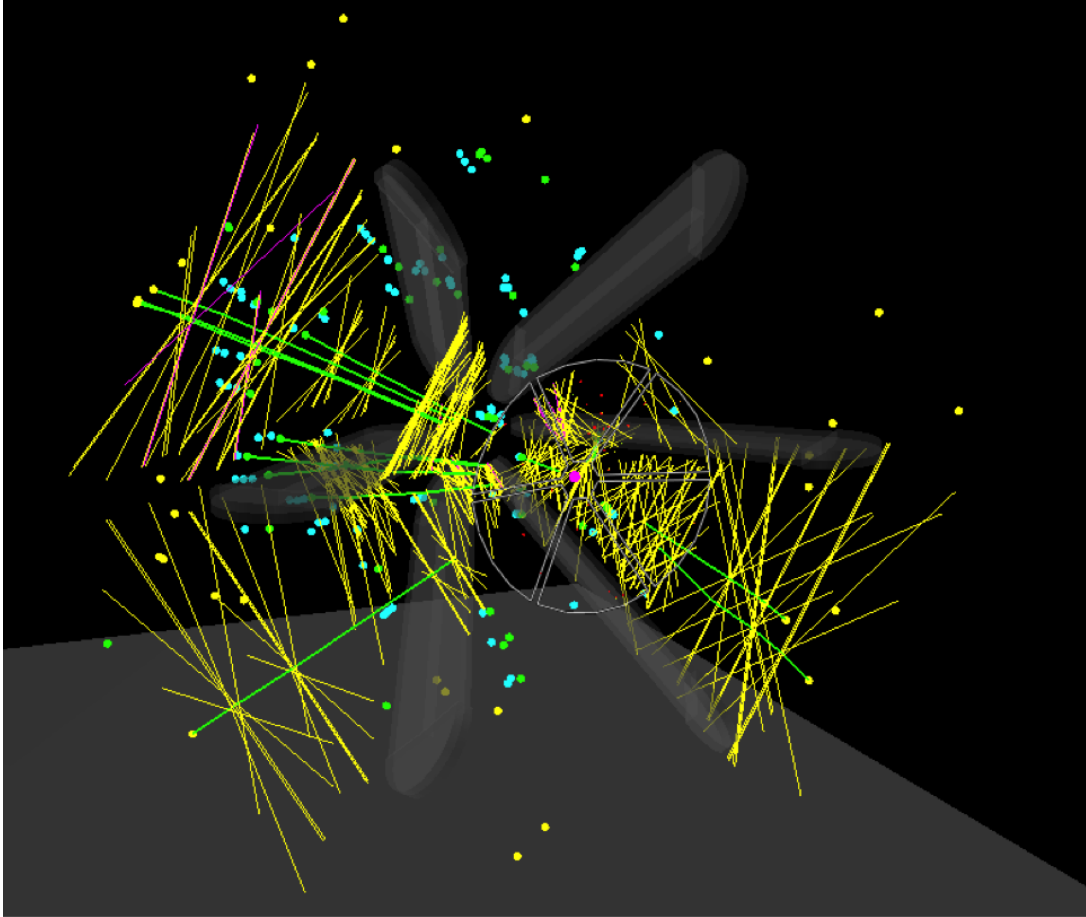

Figure 7.1: Event display of a measured ^{197}Au+^{197}Au event at 1.23 GeV/u. The coils of the magnet are shown in gray. Yellow lines are fired wires, that have been used for the track reconstruction. The green lines show the reconstructed particle candidates, which have hits in the META system (yellow dots). All other sub-detector components are not shown for better visibility

7.1   Calibration of the MDCs

In the following section the measurement method and calibration of the MDC data will be discussed. The calibration can be divided in 2 parts called "Cal 1"and "Cal 2". Time measurements in the MDCs are performed relative to a common stop signal. Therefore the signal of the TDC[17] (t_{TCD}) is converted into a drift time (t_{drift}):

$$t_{drift} = \text{offset}(ns) - t_{TDC}(ch) * \text{gain}(ns/ch),   \tag{17}$$

by using calibration coefficients: *gain* and an *offset*, The gain converts the measured TDC channel number into ns, and is an internal feature of the used ASIC TDCs. The offset is used to normalize the drift time: particles flying closest to the anode wire define the shortest possible drift time, which is set to "zero". The measured time is integrated and fitted with two 0th order polynomials to find the offset for each signal[18]. In Figure 7.2(a) this method for one signal in one drift cell is shown. Since it is not clear if the closest point here is already a "zero-distances"track, the procedure is repeated iteratively until the residuals between the measurements are located around 0. On the right side of Figure 7.2(b) the effect for the correction can be seen for all drift cells of one chamber. This procedure is called Cal 1 parametrization.
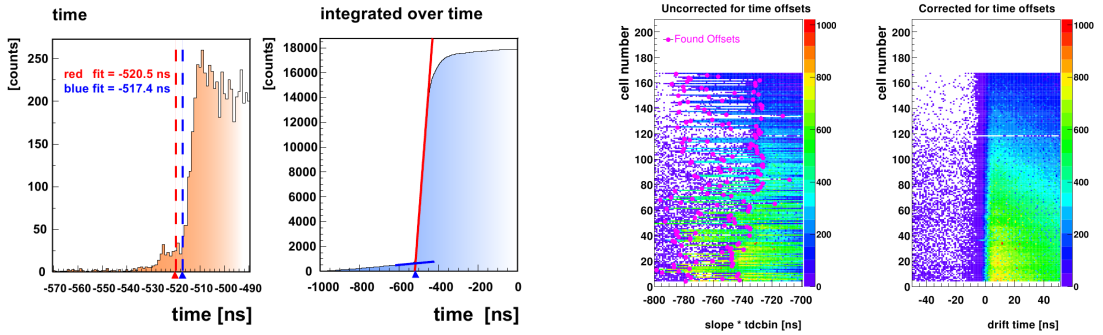
(a) The drift time spectra (left) is integrated (right). With 2 straight lines, from signal (red) and background (blue), the offset of the calibration is determined [Mar05].

(b) Drift time as function of drift cell number, before (left) and after (right) calibration [Mar05].

Figure 7.2: Cal1 parameter determination

For the track-position determination it is necessary to convert the corrected times of the Cal 1 procedure into a distance from the wire. Therefore the drift velocity is needed. The drift velocity depends on the electrical field, on the properties of the gas mixture, the temperature and the pressure of the gas. To extract precise

---

[17]Time-to-Digital Converter

[18]Signal means all measured ToT before the common stop

41

distances from the wire it is important to know all these parameters to extrapolate the effective drift velocity. Temperatures of the gas, temperatures of the read out electronics and furthermore the gas pressure of the different chambers are monitored. In April 2012 the gas for MDC plane I was an Argon-CO_2 mixture (70:30) and Argon-Isobutan (84:16) for plane II-IV. The drift velocity as function of the electric field (E) is not constant but a function $v_{Drift}(E)$. GARFIELD-simulations[GAR11] are used to extract this function at given gas properties. This method is called Cal 2.

In the measurement campaign in April 2012 the MDC gas properties and the operation high voltage changed during the beam time. The output (pressure, temperature) of the CSS[19] monitoring device was converted into a "root tree"and then analyzed. Furthermore, the change of the high voltage of the drift field was extracted from an ORACLE database. The changes in the high voltage were large compared to changes of other properties, that stayed rather constant. In Figure 7.3 an example of this procedure is shown. Here s is the number of the sector and m the number of the module, starting from 0. For example m2s3 is the 4th module[20] of the 3rd MDC plane. The purple distributions show small (<50 V) differences. Those are caused by small currents in the order of a few mA (See Figure 7.4). The MDC chamber ramps down the voltage by few V until the current vanishes. The red parts corresponds to an archiver failure of the read out. The system was disconnected and reconnected and therefore the value was set to
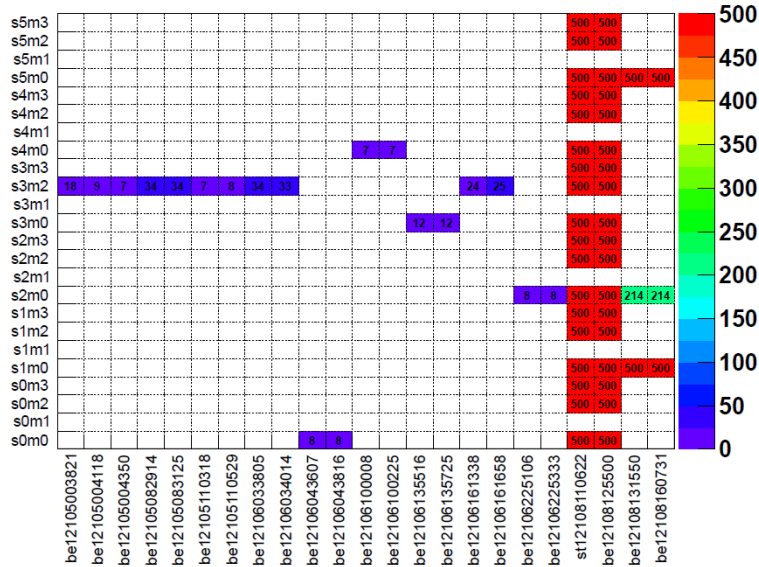

Figure 7.3: Difference in the high voltage (in comparison to the event before) as a function of the analyzed file (x-axis) and the position in the MDCs in detector coordinates (y-axis). For illustration purposes the maximum value is set to 500V.

---

[19]Control System Studio

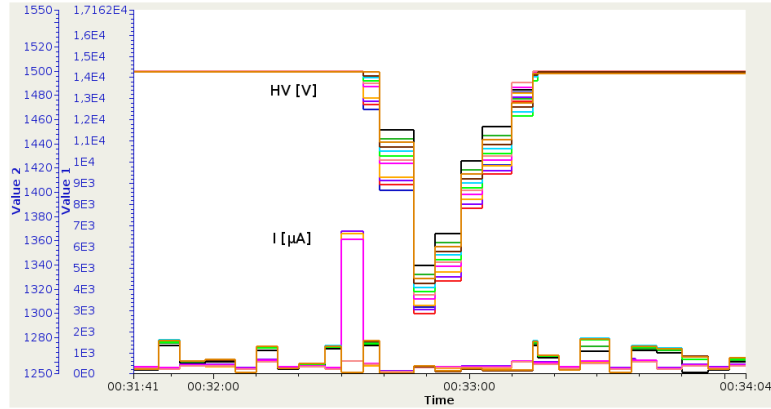[20]First module is at 0° in ϕ angle

Figure 7.4: Voltage (upper curves) and leakage current (lower curves) of individual wire layers as a function of time, for MDC m2s3, demonstrating the active over current protection via automatic HV ramp procedure upon a detected current spike.

-9999 V. These are no real changes of the high voltage and therefore this changes are need taken into account for the parameters. A scan for different chambers was performed and the high voltage setting were determined. Cal 2 tables were created for different HV settings. An additional set for complete chambers with lower (1250 V, 1400 V) voltages was created as well. The method is described in detail in [Mar05].

7.2   Track Reconstruction

After the calibration of the MDCs the position of the hit points of a track are known. These points contain, besides the spatial place of the point, also the information about the direction of the particle. In general the 3D information of a track is reduced to a hit in different projection planes. To minimize the number of wrongly assigned tracks, the inner (MDC I and II) and outer (MDC III and VI) (approximately straight) track segments are reconstructed independently with a so-called Cluster Finder and a Segment Fitter Algorithm. Scanning over all target positions the Cluster Finder

Figure 7.5: Cluster Finder Algorithm. The number of hits is shown as function of the position.

Algorithm searches for overlapping fired wires in the inner MDC chambers (See Figure 7.5), and combines them into a part of a track. Behind the magnetic
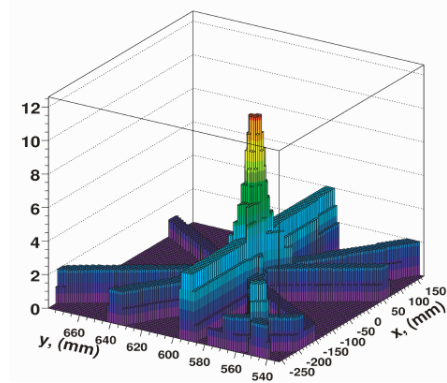
43

field hit points on the outer MDCs are fitted with straight line as well. The intersection of these fit lines defines the so-called "kick-plane". The kick-plane describes the assumption that the particle trajectory is not bent but just gets a kick relative to a dedicated plane. The segments are combined together by the Segment Fitter Algorithm. Figure 7.6 shows the procedure. Track that are not used in the vertex finding are later used for analysis of particles which decay via weak interaction that are typical off-vertex, like Λ and K_s^0 [Sch15].
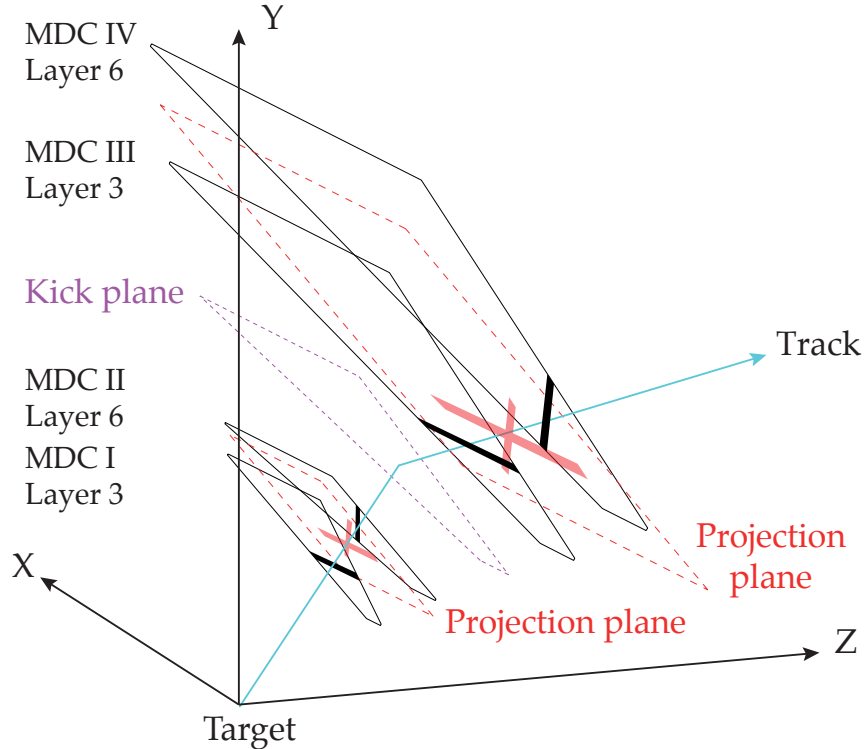
Figure 7.6: Reconstruction of tracks with the Cluster so-called Finder and a Segment Fitter Algorithm. The black trapezoids indicate one MDC chamber, with fired wires (all wires are summed up as one black stripe). Between the MDCs the virtual projection plane is shown in red together with the clusters obtained from the Cluster Finder. The kick-plane used in the Segment Fitter Algorithm is shown in purple. Figure taken from [Mar05]

7.3   Momentum Measurements

After reconstruction of the particle track, its momentum is determined based on the Lorentz force:

$$\vec{F}_L = q(\vec{v} x \vec{B}) \tag{18}$$

where $\vec{v}$ is the velocity of the particle and $\vec{B}$ the magnetic field along the particle's trajectory. The particle changes its flight direction. Integrated over the whole

flight path s, the total change of momentum $\Delta \vec{p}_{tot}$ is:

$$\Delta \vec{p}_{tot} = \vec{p}_{out} - \vec{p}_{in} = \int d\vec{p} = \int \vec{F} dt = \int q((\vec{v}) \times \vec{B}) ds = -q \int \vec{B} \times d\vec{s} \quad (19)$$

where, $\vec{p}_{out}$ and $\vec{p}_{out}$ is the outgoing and incoming momentum (relative to the magnetic field) of the particle. One can see from Equation 19 that the change of the momentum is independent of the particle momenta. The corresponding deflection angle $\Delta\Theta$ between the in and outgoing particle momenta is given by:

$$\sin\left(\frac{\Delta\Theta}{2}\right) = \frac{\Delta \vec{p}_{tot}}{2|\vec{p}_{tot}|} \quad (20)$$

In HADES the momentum is obtained using a Runge-Kutta tracking algorithm. It solves the equations of motion in an iterative procedure. It uses a start momentum obtained by a spline method. The equations of motion are solved at the orange points indicated in Figure 7.7. The resulting momentum is used as a start parameter for the Runge-Kutta tracking algorithm. It uses the momentum from the Spline Method to calculate the next hit point and finally reconstruct the full track momentum in a recursive method. The resulting trajectory is compared to the real hit points and the procedure is repeated with the new start momentum
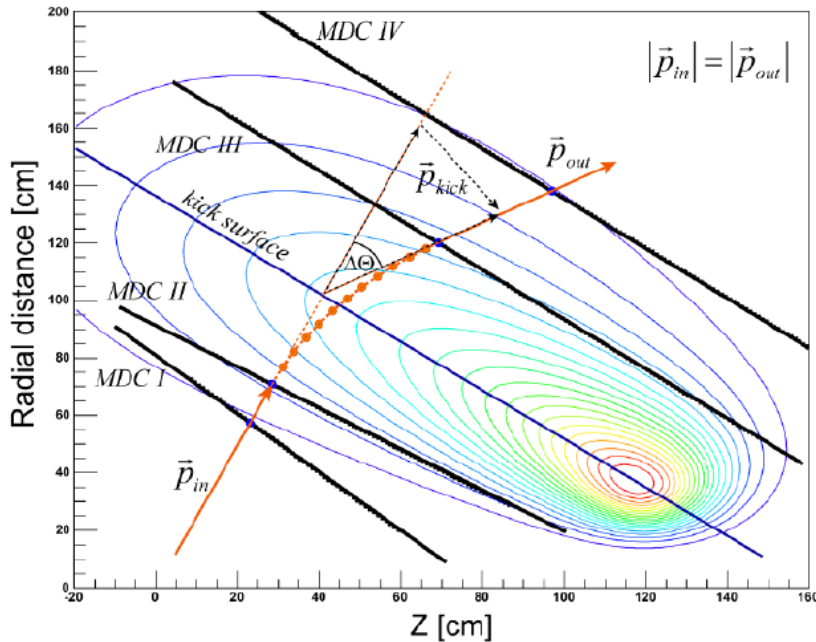

Figure 7.7: Schematic Picture of momentum determination. The magnetic field lines (contour plot) are shown in radial distance ($\sqrt{(x^2 + y^2)}$) as a function of the distance in z (beam-axis) is shown. Four MDCs are shown in black. The orange curve shows the flight path of the particle. The kick-plane is indicated in blue. Figure taken from [Sch08]

until it converges. If after 11 iterations no minimum is reached the track is neglected in further analysis as its momentum is not determined. The quality of fitting to the tracks is given by the value χ^2_{RK}. Details of the method are given in [Rus06, Sch08]. Besides the momentum, the polarity $\frac{|p|}{p}$ of the particle can be determined by this procedure.

7.4   Time-of-flight measurement

In addition to the momentum of the particle the velocity, needs to be known. To calculate the velocity, the time-of-flight has to be measured. In general a velocity is calculated as:

$$\bar{v}_{\Delta s} = \frac{\int_{t_1}^{t_2} ds}{t_2 - t_1} = \frac{\Delta s}{\Delta t} \tag{21}$$

where t_1 and t_2 describe start and end time and s the path od the particle. Both the time and the positions are known from the signals measured in the start and the META system. Velocities are expressed as fraction of speed of light:

$$\beta = \frac{v}{c} \tag{22}$$

The relativistic Lorentz factor γ is given by:

$$\gamma = \frac{1}{\sqrt{1 - \frac{v^2}{c^2}}} \tag{23}$$

and can be used together with the calculated momentum to determine the particle mass:

$$m = \frac{p}{\beta\gamma}. \tag{24}$$

Furthermore, by equating the Lorentz and the centrifugal force the relation between mass and charge can be obtained:

$$\frac{m}{Z} = \frac{p}{\beta \cdot \gamma \cdot c}. \tag{25}$$

Due to uncertainties from the measurements of the time-of-flight systems velocities higher than the speed of light can occur. To avoid those imaginary masses the squared mass is used for further calculations:

$$\frac{m^2}{Z^2} = \frac{p^2}{\beta^2 \cdot \gamma^2 \cdot c^2}. \tag{26}$$

In Figure 7.8 the momentum $\times$ charge distribution versus the velocity is shown. Since the resolution for the two different META detectors are different, the distributions are shown separately. The different particles species are visible in different

bands, and their theoretical curves are shown in black. The leptons, which are the relevant particles for this work, are located at high velocities and low momenta. The mass over polarity distribution is shown in Figure 7.8 for TOF (left panel) and RPC (right panel). The signals of the measured particles are indicated. The better resolution of the RPC directly translates to a smaller width of the peak. Particle identification in general is realized via 2 dimensional selections in the velocity versus momentum × charge plane. The lepton identification used in this work is described in Section 8.2.

(a) TOF

(b) RPC

(c) TOF

(d) RPC
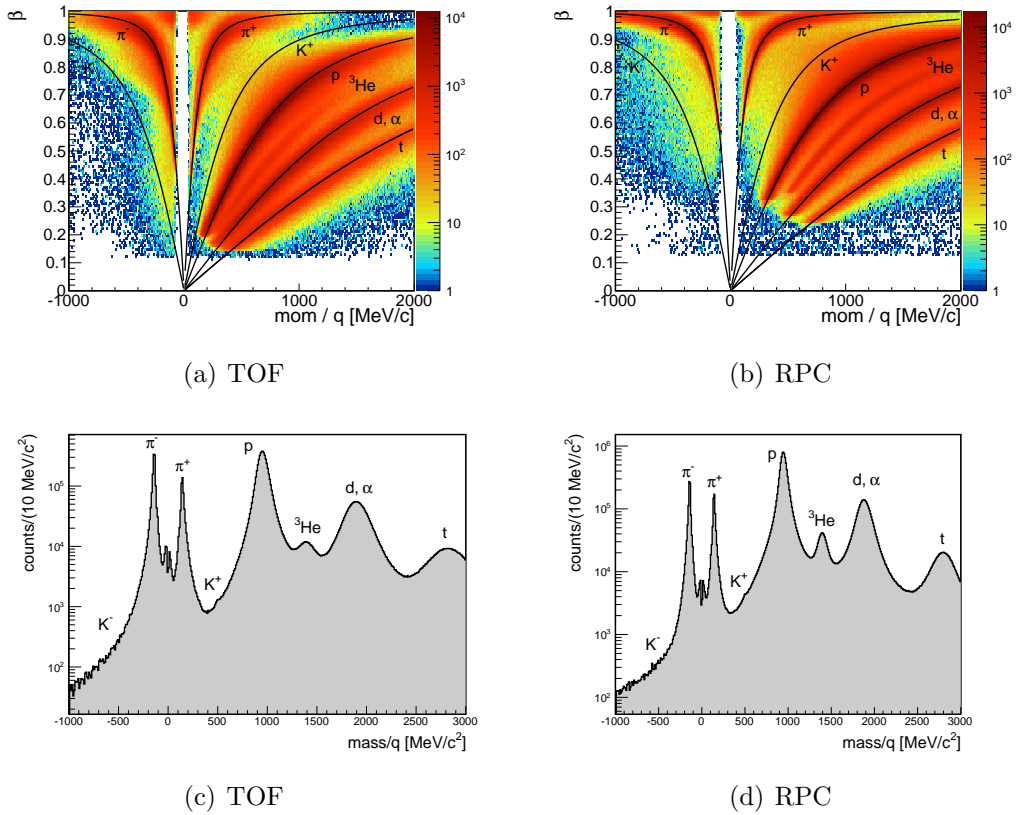
Figure 7.8: Upper row: velocity versus momentum × charge distribution for TOF (left) and RPC (right) region. Theoretical particles curves as indicated in black. Lower row: mass over polarity for TOF (left) and RPC (right) region. The particles species are indicated at each peak. Figures taken from [Sch16]

7.5   Determination of the Energy Loss of Particles

Particle identification can also be performed by measuring the specific energy loss dE/dx) of particles in material. The energy loss of a particle with the energy E, traveling a distance x, is given by the Bethe-Bloch formula [BA53, Blo33]:

$$-\frac{dE}{dx} = \frac{4\pi}{m_e c^2} \cdot \frac{nz^2}{\beta^2} \cdot \left(\frac{e^2}{4\pi\epsilon_0}\right)^2 \cdot \left[\ln\left(\frac{2m_e c^2 \beta^2}{I \cdot (1 - \beta^2)}\right) - \beta^2\right] \tag{27}$$

where v is speed, z the charge of the particle that is stopped by material with electron number density n and mean excitation potential I and where ϵ_0 is the vacuum permitivity, e is the electron charge and m_e is the rest mass of the electron. HADES uses this method in the TOF detector and in the MDC chambers. In Figure 7.9 the specific energy loss in the MDCs versus momentum of the particle measured in the different META detectors is shown. The same representation for the energy loss in the TOF detector can be found in 7.9(c). Theoretical curves are indicated in black and labeled with the corresponding particle. The energy loss is used for additional particle separation and increases the purity of the identification. Details can be found in [Sch16].

(a) MDC dE/dx (TOF)
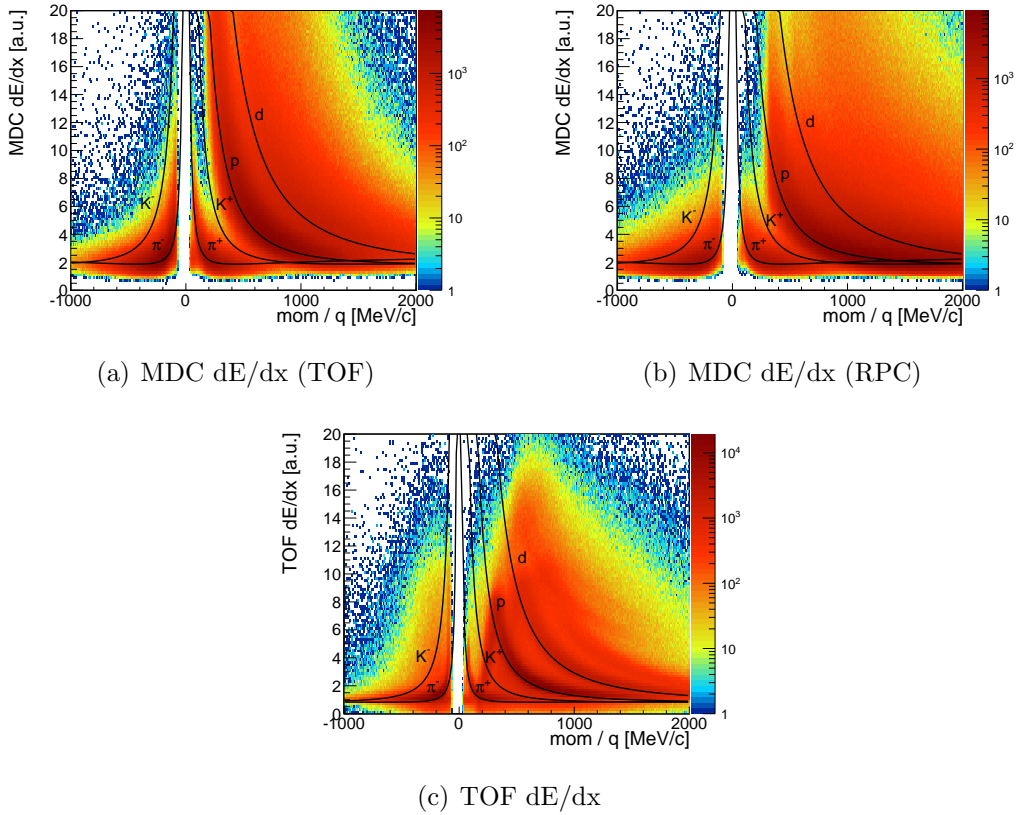

(b) MDC dE/dx (RPC)

(c) TOF dE/dx

Figure 7.9: Energy loss versus momentum $\times$ charge distribution in (upper row) the MDCs (lower panel) TOF detector. Theoretical particles curves as indicated in black. Figures taken from [Sch16]

Part III
Reconstruction of Neutral Mesons

*A pessimist sees the difficulty in every opportunity;
an optimist sees the opportunity in every difficulty.*

Winston S. Churchill

Neutral particles can not be detected directly in HADES, since the current spectrometer setup has no calorimeter. However, photons can be detected though external conversion, i.e. lepton pair production close to an atomic nucleus. The pseudoscalar meson (π^0 or η) decays into two real photons or via Dalitz decay. In the first case both photons need to convert in material into a lepton pair. This process is called *double photon conversion*, and shown in Figure 7.10(a). In the second case only the real photon needs to convert. The other photon is virtual and therefore decays instantaneously into a lepton pair. This process is referred as *Dalitz photon conversion*, and shown in Figure 7.10(b). The direct decay of the meson in four leptons, which is a decay via two virtual photons is also taken into account. Since this process is suppressed by an order of magnitude the analysis strategy is not optimized for it. The vertex resolution for lepton pairs is in, of the order of cm, which not good enough to cleanly isolate the various converter parts in the event reconstruction. Therefore no specific vertex cuts are applied and and a cumulated conversion effect is used.
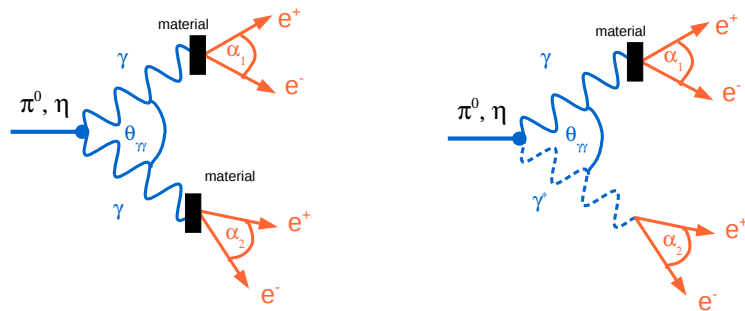
(a) Double photon conversion   (b) Dalitz photon conversion

Figure 7.10: Schematic diagrams of four-lepton final states of meson decay. The meson (blue straight line), decays into two real photons (blue solid wavy line) or via Dalitz decay. The virtual photon (blue dashed wavy line) of the Dalitz decay decays instantaneously, into a lepton pair (orange arrows). The real photons convert in material (black boxes) as well into a lepton pair. Selections on the indicated angles (α_1, α_2 and $\Theta_{\gamma\gamma}$) are used to extract the signal.

8   Analysis Strategy

The HADES analysis is performed within the HYDRA[21] framework [Gar03, Col], which is based on the ROOT data analysis package [Pro96]. A data base (implemented in ORACLE) initializes geometry, setup and calibration parameters. Description of the general analysis strategy can be found in [Sch08, Mar05, Gal09]. In this work the reconstruction is realized in four steps: event selection (Section 8.1), lepton identification (Section 8.2) and topological selection of real and virtual photons (Section 8.3) as well as of mesons (Section 8.4). Variation of topological criteria allows to estimate the systematic uncertainties of the method, as it will be discussed later in Section 11.2. Due to the missing vertex selection in the reconstruction the processes leading to the four lepton final states are indistinguishable. All corrections are therefore applied as effective average corrections. It is assumed that the reconstruction efficiencies $\epsilon_{tot} = \epsilon_{rec} \cdot \epsilon_{PID}$ for all three four-lepton processes are similar. The main parameters that effect the reconstruction are the momentum of the leptons and the opening angle between them. The Pluto event generator is used to prove that the phase space distributions of the decay processes $\pi^0 \to \gamma\gamma$ and $\pi^0 \to \gamma\gamma^*$ are similar. Figure 8.1(a) shows $m_\perp$

(a)   (b)
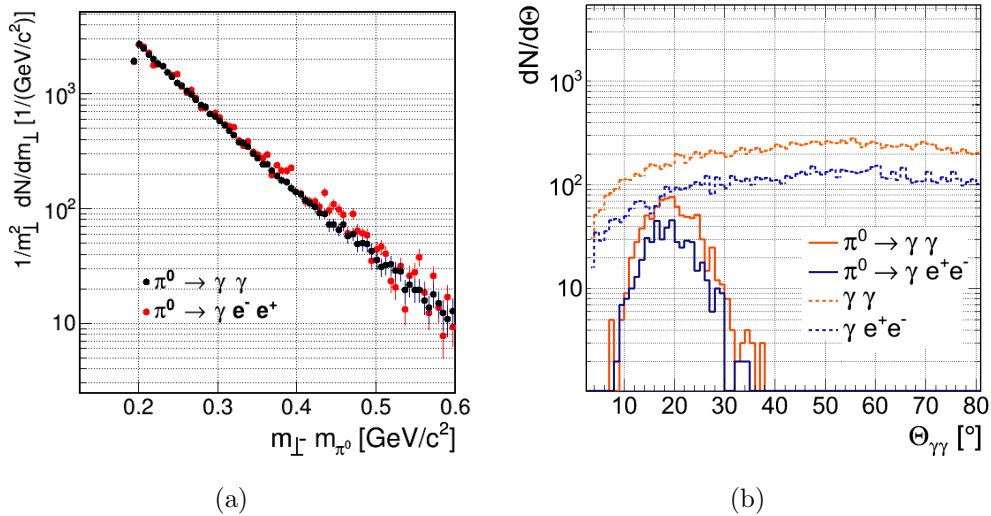
Figure 8.1: Main parameters for the reconstruction of neutral pions. (a)Y integrated $m_\perp$-m_{π^0} for $\pi^0 \to \gamma\gamma$ (black circles) and $\pi^0 \to \gamma e^+e^-$ (red circles). Both spectra are obtained asking for the decay products to be in the acceptance of the detector ($18° < \Theta < 85°$ and $p > 25$ MeV/c). (b) Opening angle distribution between real (and virtual) photons $\pi^0 \to \gamma\gamma$ (orange solid curve) and $\pi^0 \to \gamma e^+e^-$ (blue solid curve) show a similar distribution and favor angles $10° < \Theta_{\gamma\gamma} < 40°$. In contrast uncorrelated photons, e.g. those coming from different sources show a broad distribution. See also Section 9.3

---

[21]**HADES** s**Y**stem for **D**ata **R**eduction **A**nalysis

spectra, where the decay products have to be in the acceptance of the detector. One can see that both distributions agree in shape. The other property that affects the reconstruction efficiency is the distribution of the opening angle between the real (and virtual) photons. This distribution is shown in Figure 8.1(b). The distributions of $\pi^0 \rightarrow \gamma\gamma$ (orange solid curve) and $\pi^0 \rightarrow \gamma e^+ e^-$ agree.

The number of neutral mesons M_m per event (with $m = \pi^0, \eta$) can be calculated as follows:

$$M_m = \frac{N_m^{rec}(p_\perp, Y)}{\langle BR_{eeee} \rangle \cdot \epsilon_{ACC} \cdot \epsilon_{rec} \cdot \epsilon_{PID} \cdot N_{evts}}, \tag{28}$$

where $N_m^{rec}(p_\perp, Y)$ is the number of reconstructed mesons and N_{evt} is the number of analyzed events. Analogue to [ABB+13] the factor $\langle BR_{eeee} \rangle (M_m, H, p_\perp, Y, (x, y, z)|_c)$ is an *average effective branching ratio* in channels containing lepton pairs or photons, given in Table 1.1. Conversion probability in the detector material is obtained from GEANT simulations, where $(x, y, z)|_c$ is the conversion vertex (Section 10.1). $\epsilon_{ACC}(p_m, \Theta_m)$ is the geometrical acceptance (of the 4 lepton multiplet), $\epsilon_{rec}(p_\perp, Y, (x, y, z)|_c)$ the reconstruction efficiency, and ϵ_{PID} the efficiency of particle identification. These factors will be discussed in Section 10.

8.1   Event Selection

The HADES event selection is optimized to select 43% of most central inelastic nuclear interactions in ^{197}Au+^{197}Au collisions as efficiently as possible, by reducing the contribution of events from reactions of the beam with other material than the target, for example the start detector. This is done with coincidence measurements between various detector subsystems and constraints on the reconstructed event vertex.   In Figure 8.2 the reduction of the number of events
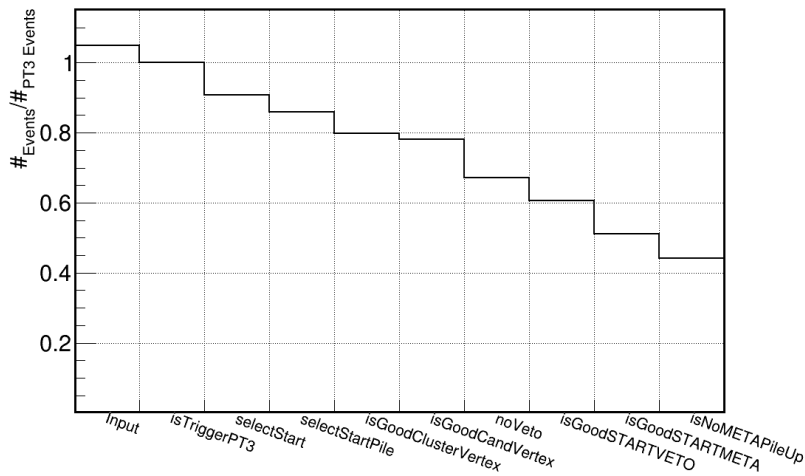

Figure 8.2: Effect of the event selection criteria on the number of used events. For details see text.

that pass the selection criteria is shown. The `Input` events are all events collected during the ^{197}Au+^{197}Au measurement ($7.0 \cdot 10^9$ events). The online event selection is based on a hit multiplicity of more than 20 hits in the TOF detector, which is called PT3 trigger (`isTriggerPT3`). All further selections are applied to the PT3 triggered events. A coincidence with a single hit in the start de-
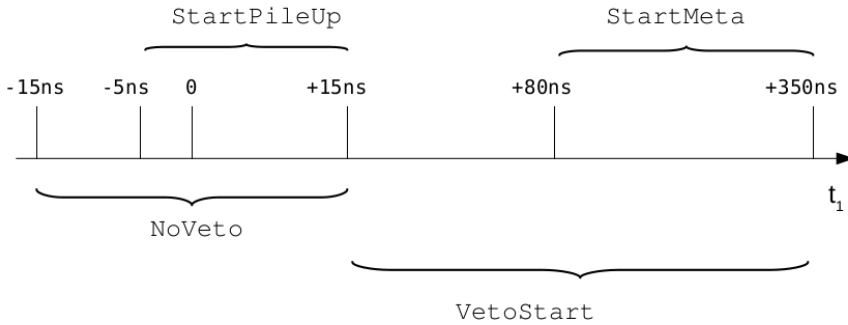

Figure 8.3: Coincidence measurements for event selection [Sch16]

tector is required (`selectStart`) and the event is removed if double hits occurs (`selectStartNoPileup`). Furthermore, a reconstructed vertex within the target region (z > -65mm) is needed. The vertex can be reconstructed using at least one reconstructed track (`isClusterVertex`) or at least two identified particles (`isCandVertex`). Both criteria act similar and they complement each other. Coincidence measurements of various detector subsystems (Schematic view in Figure 8.3) are used to remove pileup[22] events and events where no reaction with the Au-targets occurred. The `noVeto` condition removes events where after 10 ns a reaction with the veto detector is recorded. Coincidence measurement of start and veto (`isGoodSTARTVETO`) requires that no hit in veto is measured between 15-350 ns. A similar function exists as well for start and META (`isGoodSTARMETA`) which requires that detector hits are measured between 80-350 ns. A similar effect is reached by the `noMETAPILEUP` function. Here the number of tracks in the MDC is compared to the number of hits in the META detector. If their ratio lies outside the physically possible correlation the event is rejected. Event selection reduces the number of events to 43% of the PT3 events ($2.94 \cdot 10^9$).

Glauber simulations [G$^+$53] are used to convert the measured multiplicities to centrality classes. The used trigger conditions corresponds to a maximum impact parameter of 10 fm, equivalent to 43% most central collisions. The centrality as function of the number of META hits is shown in Figure 8.4(a). In Figure 8.4(b) the total cross section as a function of the impact parameter is shown. Centrality classes of 10% are indicated with different colors.

---

[22]events where more than one nucleon-nucleon collision has happened
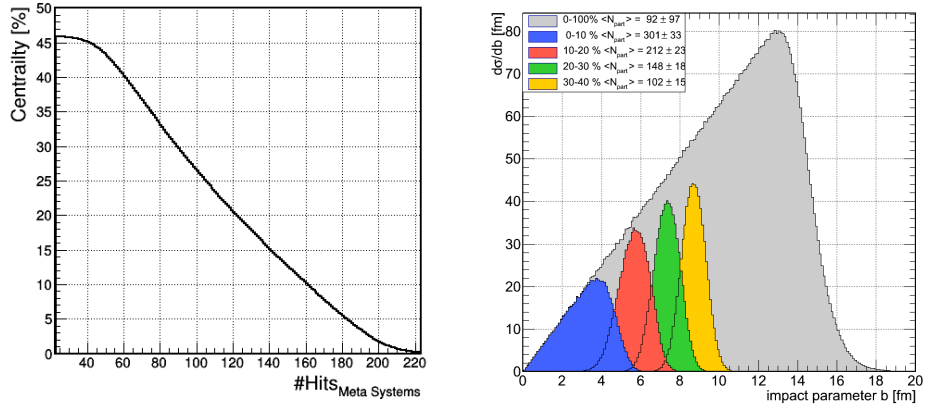
(a) Centrality (as fraction of the total cross section in %) as function of number of META hits

(b) Cross sections as a function of impact parameter b.

Figure 8.4: Multiplicity estimation using Glauber calculations. Different centrality classes are indicated with different colors [Kar15].

8.2   Lepton Identification

In order to reduce computing time, an event pre-selection is done by storing only events containing at least four-lepton candidates. A candidate has to have a reconstructed inner and outer MDC track segments and a hit in the META system. $\chi^2_{RK} < 1000$ is selected to have a full reconstructed track (see Section 7.2). Lepton identification is based on energy loss (dE/dx) in the MDC detector and a momentum dependent velocity measurement in the META detectors. The energy loss in the MDCs is calibrated and parameterized like the known Bethe-Bloch distribution [BA53, Blo33] and the expected behavior for leptons is calculated. Candidates with an MDC energy loss larger than 10 MeV are unlikely to be leptons and therefore are rejected (Figure 7.9). Figure 8.5 shows velocity vs. momentum distribution of the candidates. All candidates with momentum smaller than 750 MeV/c and reconstructed mass smaller than 70 MeV/c^2 are assumed to be leptons. These criteria give a high efficiency of the lepton sample (will be discussed in Section 10). One can clearly see impurities coming from charged pions (π^+, π^-) at lower β and higher momentum in both systems, in particular in the RPC. Besides electron track selection criteria further topological pair cuts are applied in order to reduce impurities coming from hadrons (π^+, π^-, p) and random combinations of lepton pairs. This will be explained in more details in the following chapter. Due to the limited granularity of the MDC, only pairs with an opening angle larger than 1.5° can be identified as two separate tracks. Typical opening angles of lepton pairs from conversion are on the order of 1° (see Figure 8.7). Therefore, in this analysis, sharing of fired wires in the inner MDC is allowed, which means two tracks can be identified using the same
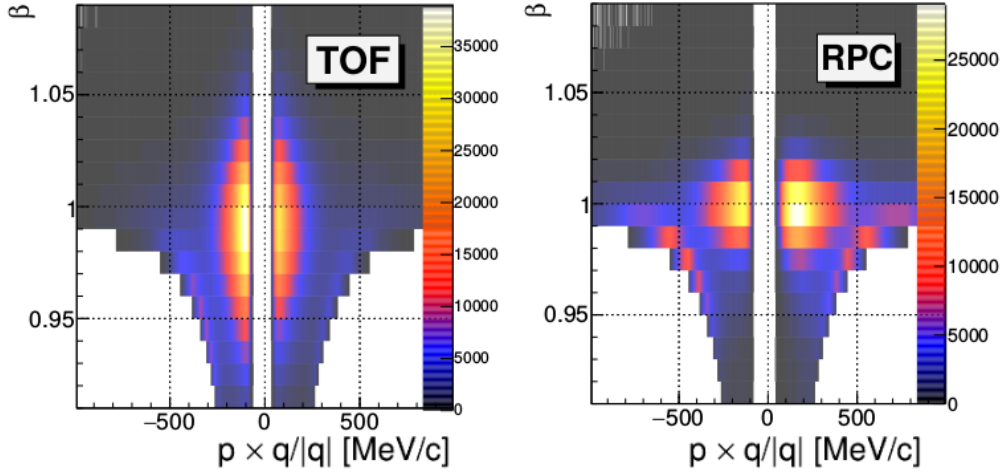
Figure 8.5: Velocity as functions of momentum × |charge| for ToF region (left) and RPC region (right).

fired wire in the MDC. In the outer MDCs sharing is not allowed since the angle between the leptons is opened up while traversing the magnetic field, due to their opposite charge. This further allows that, even if the hits are shared in the inner MDCs, an opening angle can be reconstructed. The drawback of this is a loss of precision of the conversion vertex resolution. The reconstructed vertex in the radial ($r = \sqrt{x^2 + y^2}$) vs. z-plane is shown in Figure 8.6. The left panel of Figure 8.6 shows the distribution corresponding to the case where sharing of tracks in inner segment of the MDCs is not allowed. At z < 0 mm the target region can be seen.
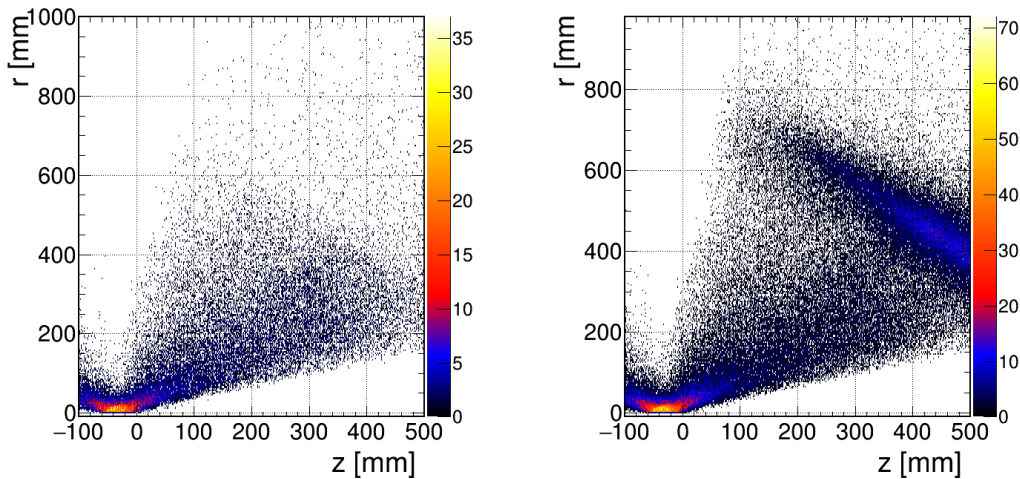
(a) Sharing of inner MDC segment not allowed   (b) Sharing of inner MDC segment allowed

Figure 8.6: Vertex (radial vs. beam-axis) distribution of reconstructed lepton pairs after application of all cuts for π^0 identification.

Figure 8.6(b) shows the same distribution, but sharing of wires from two tracks is allowed the inner segment of the MDCs. The target region is visible again, but at large values of r and z a second structure appears. This structure is a result of photons that convert outside of the target region, i.e. the mirror of the RICH detector. Most of the pairs that are created retain an opening angle smaller than 1.5 as there is no material with which they can interact. Therefore, they are seen as a single track in the inner MDC. Allowing the tracks to share the inner MDCs increases the usable conversion material by a factor three (details see Section 10.1). However, leptons produced by conversion in RICH material cannot emit enough Cerenkov light in the radiator to be identified as a lepton. Therefore RICH information is not required for lepton candidates in this analysis.

8.3   Reconstruction of Real and Virtual Photons

Single lepton candidates are further combined into pairs. The algorithm, developed in this work, is shown in Appendix A. It selects the first four lepton candidates (l_i, with i= 1,2,3,4) and combines them in three (C_j, with j= 1,2,3) possible pairs (A,B), as shown in Table 8.1. The opening angles of the pairs are then compared to each other and the pair with the smaller angle is labeled as *close* pair (α_1), while the other pair is labeled as *open* pair (α_2). In the simulation pairs can be split into three categories: coming from a converted photon, coming from a virtual photon and e^+e^- pairs from uncorrelated sources. In Figure 8.7 a cocktail of these pairs is shown. The cocktail is obtained by analyzing UrQMD simulations that where propagated through the detector using GEANT and reconstructed similarly to real data. In the left panel in Figure 8.7 the opening angle

Lepton	C_1	C_2	C_3
l_1	A	A	A
l_2	A	B	B
l_3	B	A	B
l_4	B	B	A

Table 8.1: Possible combinations of 4 leptons.

of the close pairs is shown, while the right panel shows the one from open pairs. Contributions from double photon conversion favor small opening angles, where α_1 and α_2 are smaller than 5°. For the Dalitz photon conversion the close pair favors as well $\alpha_1 < 5°$, while the open pair reaches larger angles. This pattern can be interpreted such, that close pairs coming from the conversion of the real photon, while the open pair comes from the virtual photon of the Dalitz decay. The main background processes are misidentified hadrons and uncorrelated leptons. Both background processes show a maximum at low angles in case of the close pair. These are mainly contributions from conversion and Dalitz pairs, which are combined with either two leptons coming from an open lepton pair (for example from vector-meson decays) or a lepton and a misidentified hadron. Misidentified hadrons will be discussed further in Section 9.2. The used topological selection criteria, based this simulation, are $\alpha_1 < 4.5°$ and $\alpha_2 < 10°$.

The algorithm checks if the first combination C_1 full fills the selection criteria and stores the pairs in a double-pair object, and continues with a new event.
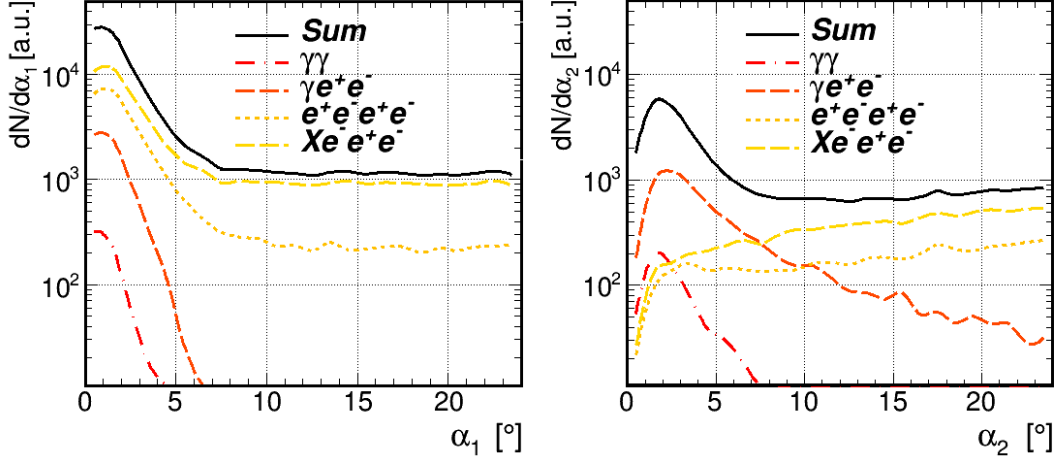
Figure 8.7: Opening angle distribution for close lepton pairs (left) and open lepton pairs (right) obtained from UrQMD simulations. The black curve is the sum of the cocktail. Contributions from double photon conversion are shown in red dashed-dotted curve ($\gamma\gamma$) and those from Dalitz photon conversion (γe^+e^-) are shown in orange dashed curve. In this cases both pairs stem from the same meson. The yellow dotted curve ($e^+e^-e^+e^-$) shows uncorrelated leptons and the yellow dashed curve ($Xe^-e^+e^-$) contributions where at least one lepton candidate is a misidentified hadron.

At this point the charge of the leptons is checked and only if a pair consists of a positive and a negative lepton it is used in the like sign spectrum. If the topological requirements are not full filled the second combination C_2 is checked. Respectively after this, the third combination C_3 would be checked, and if all possible combinations do not full fill the criteria the pairs are rejected from the analysis. If more than four lepton candidates are in the event, the procedure is repeated with a new combination of leptons, where one lepton is replaced with a one not used before. Using this method only one double-pair object can be reconstructed per event. This assumption is reasonable, since the total efficiency of the analysis is in the order of 10^{-8} (discussed in Section 10), which makes the occurrence of two correct pairs unlikely. The selected double pairs are stored and their properties are analyzed. Furthermore the close and open pair are used to create the mixed-event background, which will be discussed in Section 9.

8.4   Meson Reconstruction

The opening angle between the (real and virtual) photons ($\Theta_{\gamma\gamma}$, Figure 8.8) could be used for further identification of the meson. Due to momentum conservation, γ's need to be 180° in CMS. In the case of low momenta the opening angle between the photons strongly depends on the mass of the particle which decays. Since the π^0 has a mass of 135 MeV/c^2, $\Theta_{\gamma\gamma}$ is in the range of $5° < \Theta_{\gamma\gamma} < 45°$. For η mesons the $\Theta_{\gamma\gamma}$ angle is between $40° < \Theta_{\gamma\gamma} < 140°$. The background which mainly consists out of uncorrelated (real and virtual) photons has a flat distribution. Nevertheless, tight selections in this angle will modify the shape of background in the invariant mass spectra. Therefore no selection on this angle is applied in the differential analysis.
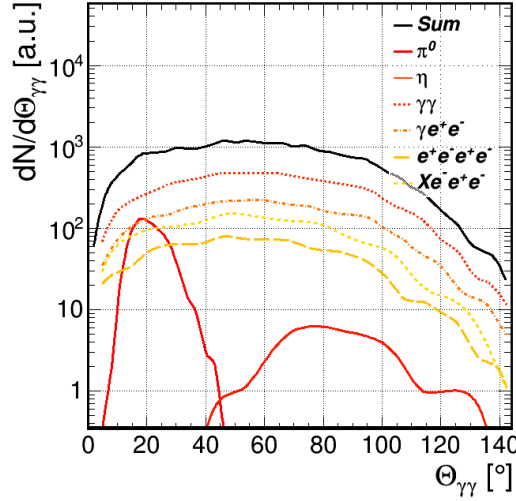
Figure 8.8: Opening angle distribution between the real and virtual photons ($\Theta_{\gamma\gamma}$), obtained from UrQMD simulations. The total cocktail is shown in black. The double pairs coming from π^0 (left) and η (right) are shown as red sold curves. The background consists out of uncorrelated photons ($\gamma\gamma$, dotted red line), uncorrelated Dalitz (γe^+e^-, dotted orange line), uncorrelated leptons ($e^+e^-e^+e^-$, dashed orange line) and misidentified leptons ($Xe^+e^-e^+$, yellow dotted line).

9   Four-lepton Multiplet Analysis

Since the results in this work are obtained using lepton double pairs, the objects will be labeled with $e^+e^-e^+e^-$. The two photon invariant mass $M_{\gamma\gamma}$ is equivalent to the four-lepton invariant mass $M_{e^+e^-e^+e^-}$. The uncorrected invariant mass spectra are also called *raw*. Unless indicated otherwise, raw specta are shown with statistical uncertainties only. Figure 9.1 shows the four-lepton invariant mass spectrum for π^0 (a) and η (b) for same-event data and mixed-event samples. In case of the π^0, the signal to background ratio was improved using a selection on $\Theta_{\gamma\gamma}$: $10° < \Theta_{\gamma\gamma} < 40°$. The mixed-event spectrum is created, using real and virtual photons. Technically this is realized using two buffers where the close and open pairs, which are (real and virtual) photons, are stored separately. Each close pair is mixed with an open pair to create the mixed-event spectrum (see Section 9.4). Variation of the buffer size were tested and did not create any systematic uncertainties. The mixed-event spectrum is normalized outside the expected peak positions[23] and is used as an estimate of the combinatorial background in the invariant mass spectrum. The ratio of the same to mixed event spectra are shown in the lower panels and show an excess (deviation from 1) at the expected π^0 and η mass. In both cases, the background obtained by event mixing describes the spectra outside of the peak regions reasonably well. The ratios

(a) π^0 (b) η
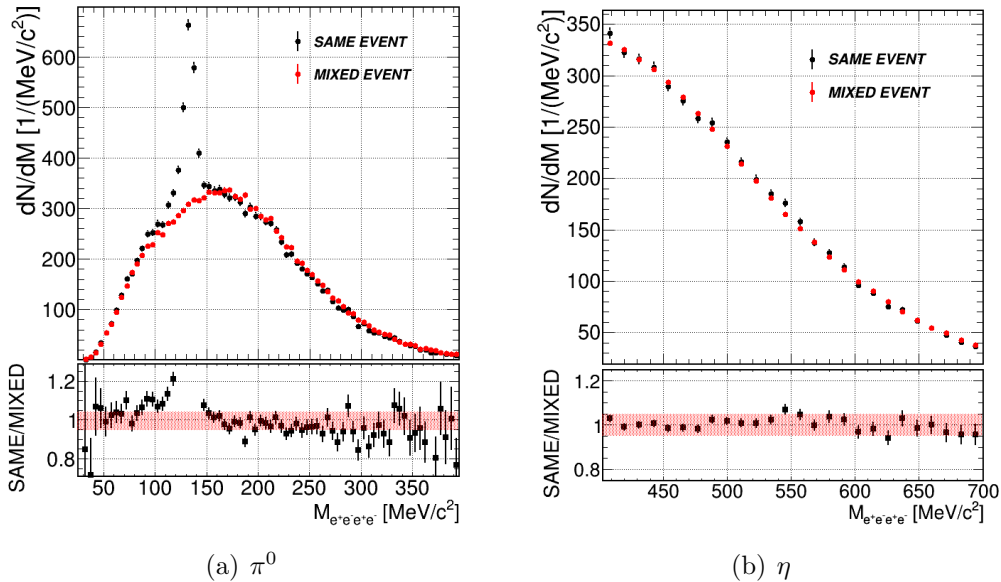
Figure 9.1: Four-lepton invariant mass spectra (black) using topological selections for π^0 (a) and η (b) mesons, together with the mixed-event background (red). The lower panels show the respective ratios of same event/mixed-event. The red band indicates 5% differences.

---

[23]peak region π^0: 100-200 MeV/c^2, peak region η: 500-600 MeV/c^2

show that the differences outside the peak regions are in the order of 5%. For the π^0 a clear peak is visible at the nominal value ($M_{e^+e^-e^+e^-} \approx 135$ MeV/c^2). A clear structure however is absent for the η. Nevertheless, additional yield above the combinatorial background is visible around $M_{e^+e^-e^+e^-} \approx 550$ MeV/c^2.

9.1   Comparison with Monte Carlo Simulations

Hundred million UrQMD events were produced, propagated through the detector using GEANT, reconstructed using realistic digitizers, and identified using identical selection criteria as applied to the real data.
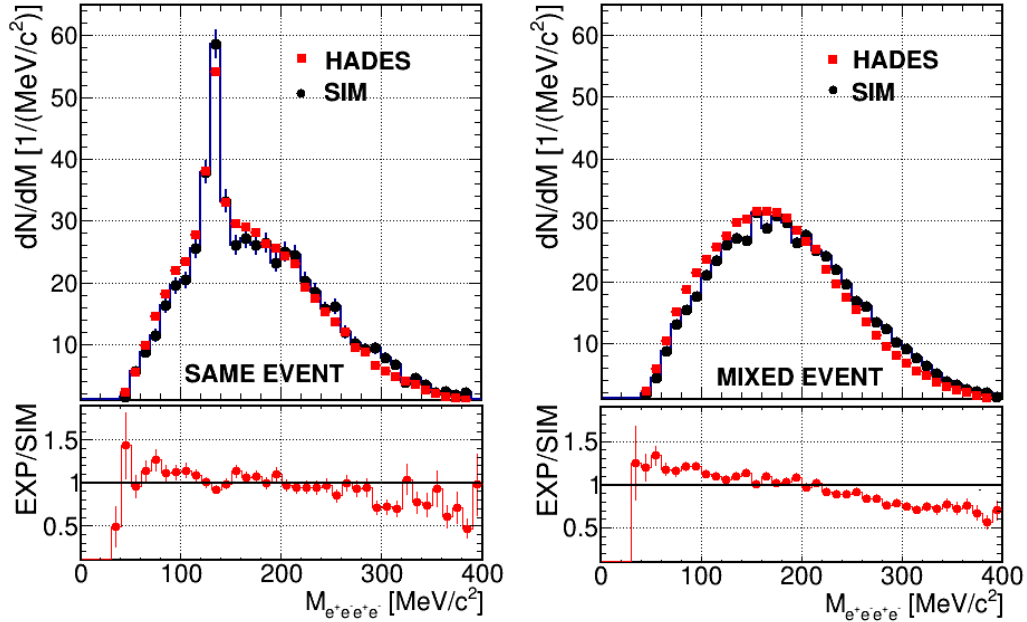
Figure 9.2: Four-lepton invariant mass spectra after application of all topological selection for π^0 for real data (red squares) and for simulation (black circles). Details see text.

Figure 9.2 shows a comparison between the measured data and the simulated data. In the upper left panel, the comparison of the same event spectra is shown. Please note that the measured spectrum is normalized to the integral of the simulated one and the binning is changed in order to allow for a better comparison. The lower left panel shows the ratio of experimental data to the simulation. In the right panel the respective distributions of the mixed event are shown. In both cases the shape of the simulated spectrum agrees within the uncertainties but is shifted towards higher invariant masses. This effect is in the order of 40%-50% and can be explained by comparing the momentum distribution of the lepton candidates that contribute to the invariant mass spectrum (Figure 9.3). Lepton candidates from simulation show a shift towards higher momenta. Pions

simulated in UrQMD show a harder spectrum compared to the observation in measurements [Sch16]. Assuming that each lepton has a slightly higher momentum in simulation compared to real data the shift of the invariant mass can be explained.

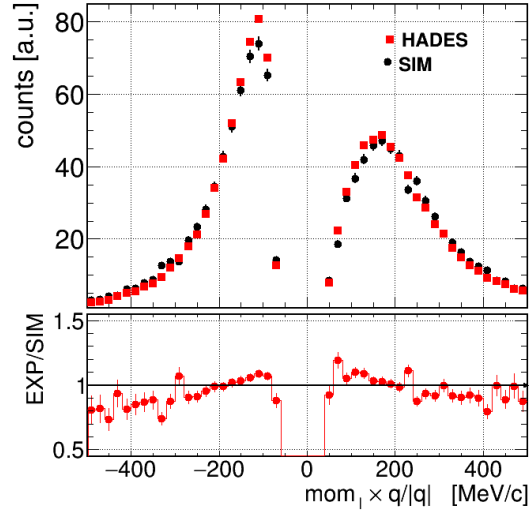Figure 9.3: Momentum distribution from simulated (black) and measured (red) lepton candidates.

9.2   Determination of Purity

Misidentified hadrons contribute to the background and influence the shape of the invariant mass spectrum. Since the chosen lepton selection is not strict, a
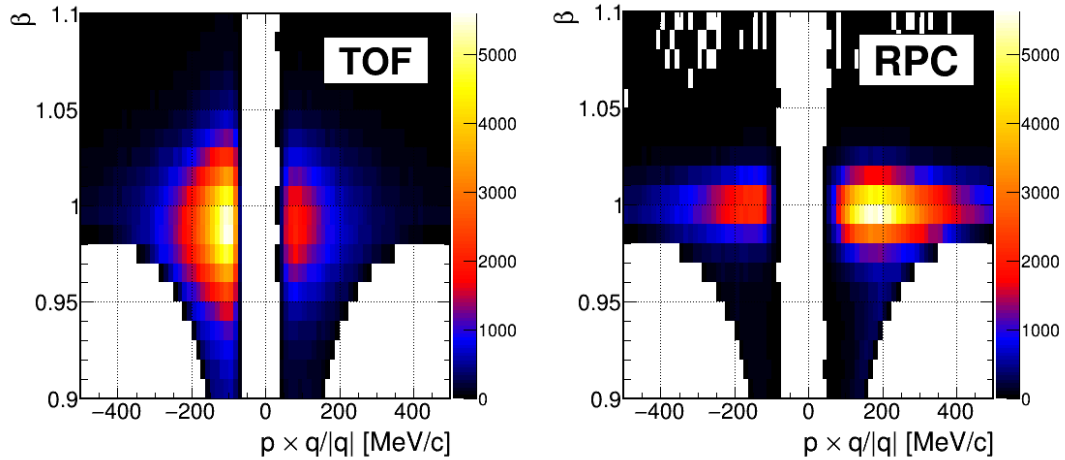

Figure 9.4: Velocity (β) as function of momentum $\times$ q/|q| for TOF region (left) and RPC region (right).

significant amount of charged pions is accepted at the single candidate level. The purity of the spectrum is increased using topological cuts, which are optimized for lepton pairs. In Figure 9.4 the velocity vs. momentum distributions for lepton candidates that passed the topological meson identification cuts for π^0 are shown. The contamination of misidentified hadrons can be estimated by using the UrQMD simulation (see Figure 9.5). The contaminated spectra are structureless, which agrees with the assumption of an uncorrelated process, that can be modeled with a mixed-event method. Stricter lepton selection could increase the purity further, which would on the other hand lead to a reduction of the signal. In order to maximize the efficiency, additional cuts are not applied.

(a) π^0 (b) η
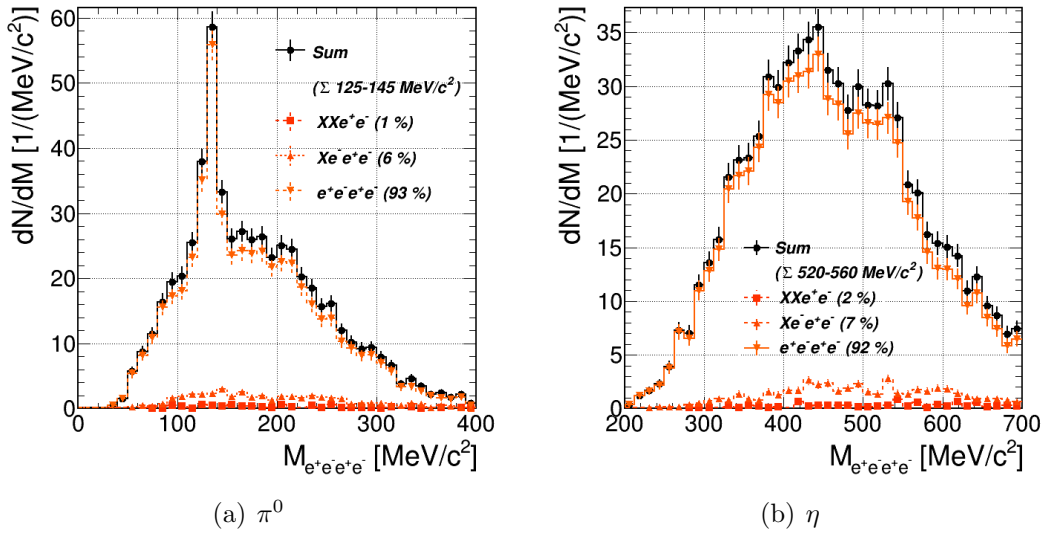
Figure 9.5: Purity estimations using simulation for π^0 (a) and η (b) mesons. The pure lepton samples ($e^+e^-e^+e^-$) are indicated with orange upside down triangles. The purity is higher than 90% for both mesons in the peak region (π^0: 125-145 MeV/c^2, η: 520-560 MeV/c^2). The spectrum with one misidentified hadron is labeled with $Xe^-e^+e^-$ (red triangle), where X can stand for any misidentified hadron with positive or negative charge. Less than 2% of the sample is contaminated with more than one misidentified charged π^0 (XXe^+e^-, red squares).

9.3   Estimations of the Combinational Background

The main background contribution under the π^0 peak in the invariant mass spectrum comes from photons that are emitted in uncorrelated processes. In Figure 9.6 a schematic drawing of a possible process is shown. Two photons, coming from different "mother" particles, convert into a dilepton pair, and are combined in a four-lepton multiplet. In the following this will be called an *uncorrelated photon pair*. Similarly, the lepton pairs coming from the virtual photon of the Dalitz decay can be combined with another lepton pair, which will be called in the following an *uncorrelated Dalitz pair*. The probability of this wrong combination is 85% per event (see Appendix B). In Figure 9.7 the four-lepton invariant mass

spectra from UrQMD simulations are shown. The left panel contains the invariant mass spectrum after application of topological selection criteria for π^0. Pairs coming from π^0 contribute with 40% to the total rate in the signal region. As expected, the main background in the signal region comes from uncorrelated photon pairs as well as from uncorrelated photon Dalitz pairs. In total 48% of the signal region are coming from them. Subtracting the signal part one can see that these correspond to (49%/59%) 80% of the total background. 4% of the counts come from uncorrelated leptons (See Section 8.3) and 7% from misidentified hadrons (See

Figure 9.6: Schematic diagram of uncorrelated background.

Section 9.2). All background contributions are structureless distributions, which confirming that they originate from uncorrelated sources. A similar picture for the selection of η candidates is shown in Figure 9.7(b). Due to the lower production cross section the η signal is much smaller compared to the π^0. Only 5% from the count rate in the signal region are two photon conversion and Dalitz photon conversion. The background components are identical to the one from the π^0 spectrum. The assumption that the main background comes from uncorrelated processes is confirmed by the simulations.

(a) π^0

(b) η

Figure 9.7: UrQMD simulations of four-lepton invariant mass spectra after applying all topological selections for π^0 (a) and η (b) mesons, together with the cocktail of the contributing sources. The black curve is the sum of the cocktail contributions. The values in the brackets are the relative contribution of the cocktail components in the peak region. The two solid curves show the contribution from the signal ($\pi^0(\eta) \rightarrow \gamma\gamma$ (red circles), $\pi^0 \rightarrow (\eta)\gamma e^+e^-$ (red triangles)). The background are uncorrelated photon pairs ($\gamma\gamma$, red triangles) as well as uncorrelated photon Dalitz pairs (γe^+e^-, orange square).

9.4   Mixed Event Background

One of the methods to describe the uncorrelated background is the mixed event technique. Photons from different events are by definition uncorrelated and can be used to describe the background. To ensure similar conditions like in the same-event spectra only events with similar properties, such as centrality and phase-space, are mixed. In this case the used centrality classes are those shown in Figure 8.4. In this work the event mixer procedure is taken from [L'H94]. Systematic uncertainties of that method are described in Section 11.2. The mixed-event background is normalized in the regions outside the expected meson peak region: 0-100 MeV/c^2 and 150-250 MeV/c^2 for the π^0 meson and 350-500 MeV/c^2 and 600-750 MeV/c^2 for the η meson. Since there is no a-priori optimal choice for the normalization domain, variations in the intervals in which the normalization are performed are considered as a systematic uncertainty. Additionally to normalizing simultaneously at left and right side of the peak, the spectra are normalized only to the left side or to the right side. In Figure 9.8 the cocktail of the mixed-event spectrum generated using simulated data is shown. In the left panel the spectra using π^0 selection is shown and on right panel the one from η selection. Only uncorrelated pairs of photons can, by definition, contribute to the spectrum. Like for the same event, uncorrelated photon pairs as well as uncorrelated photon Dalitz pairs are $\approx 80\%$ of the total background. Uncorrelated and misidentified leptons contribute in the order of $\approx 20\%$. This relative contributions agree for same event and mixed-event.

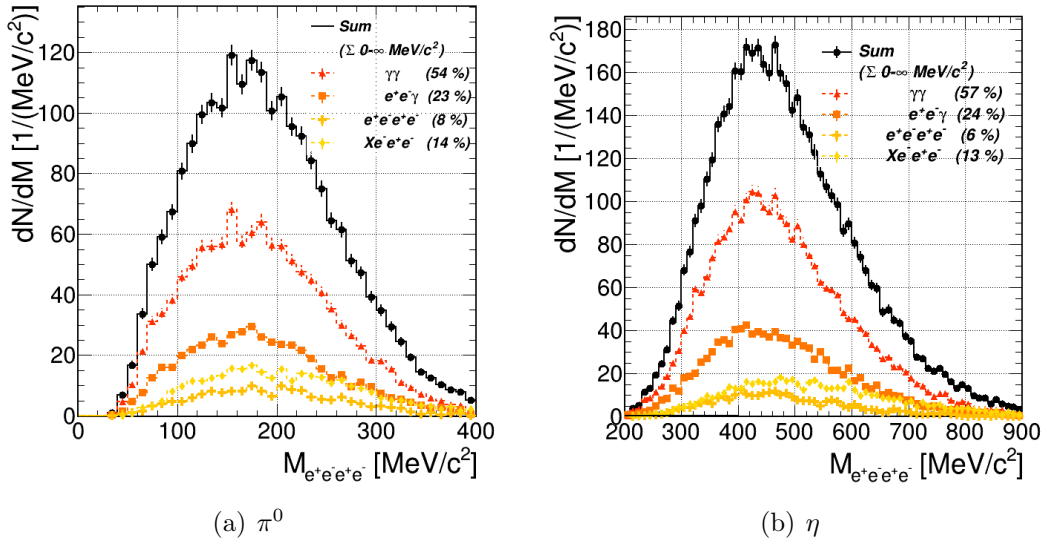(a) π^0 (b) η

Figure 9.8: Four-lepton mixed-event invariant mass spectra of simulated cocktail after all topological selection for π^0 (a) and η (b) mesons have been applied. The color code is identical to Figure 9.7

9.5   Raw Signal Reconstruction

Figure 9.10 shows signal spectra of the π^0 after mixed-event combinatorial background has been subtracted. In order to extract the peak properties the data is fitted with a mathematical function. Since the π^0 can be described as a two photon resonance the shape of the signal can be described with a Breit-Wigner function

$$p(E) = \frac{1}{2\pi} \frac{\sigma}{(E-\mu)^2 + \sigma^2/4} \tag{29}$$

where E is the center-of-mass energy that produces the resonance, μ is the mass of the resonance, and σ is the resonance width. To verify that assumption measured data from the π^0 is fitted with a Gaussian (Figure 9.9(a)) and a Breit-Wigner (Figure 9.9(b)) function. Due to the higher quality (χ^2/NDF) of the fit using the Breit-Wigner function, it is used for the signal extraction. The position of

(a) Gaussian function   (b) Breit-Wigner function
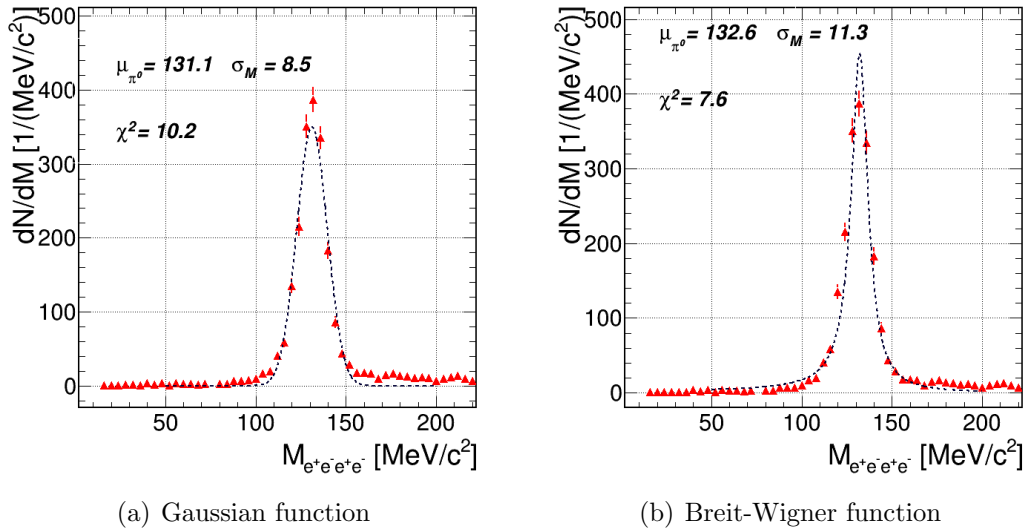
Figure 9.9: Four-lepton invariant mass spectra of simulated π^0, fitted with Gaussian (a) and Breit-Wigner (b) functions

the π^0 peak is $\mu_{\pi^0} = 133.7$ MeV/c^2 with a width of $\sigma = 11.6$ MeV/c^2. The peak is shifted by 1.3 MeV/c^2 with respect to the nominal mass of 134.98 MeV/c^2. The width is larger than the nominal value of 7.82 eV/c^2 [LMC$^+$11] due to the momentum resolution of the detector. The mass shift is caused by the missing energy loss correction for leptons. The statistical uncertainties are described in Appendix C. Systematic variation of the normalization of the background gives significantly smaller uncertainties ($_{sys}$ in Equation 30) than the statistical ones and can therefore be neglected in the following. The number of reconstructed π^0 is estimated by integrating the spectra in a $\pm 3\,\sigma$ region around the peak position:

$$N_{\pi^0} = 4606 \pm 130_{stat}(+5-6)_{sys} \tag{30}$$

The signal to background (S/B) ratio of the pion yield is ≈0.4 and the significance
((S+B)/B) of 35. Figure 9.10(b) shows the η four-lepton invariant mass spectrum
after subtraction of the mixed-event background. A peak with a significance of 3
is visible at $\mu_\eta = 548.0$ MeV/c^2 and a width of $\sigma = 23$ MeV/c^2. The peak position
is shifted by 0.9 MeV/c^2 compared to the nominal η mass of $\mu_\eta = 547.9$ MeV/c^2.
The width of the η is comparable to the one measured in p+Nb[ABB$^+$13]. The
signal yield is obtained by integrating the data in a 3 σ region using a Breit-
Wigner fit:

$$N_\eta = 424 \pm 133_{stat}(+3-1)_{sys} \tag{31}$$

(a) π^0 (b) η
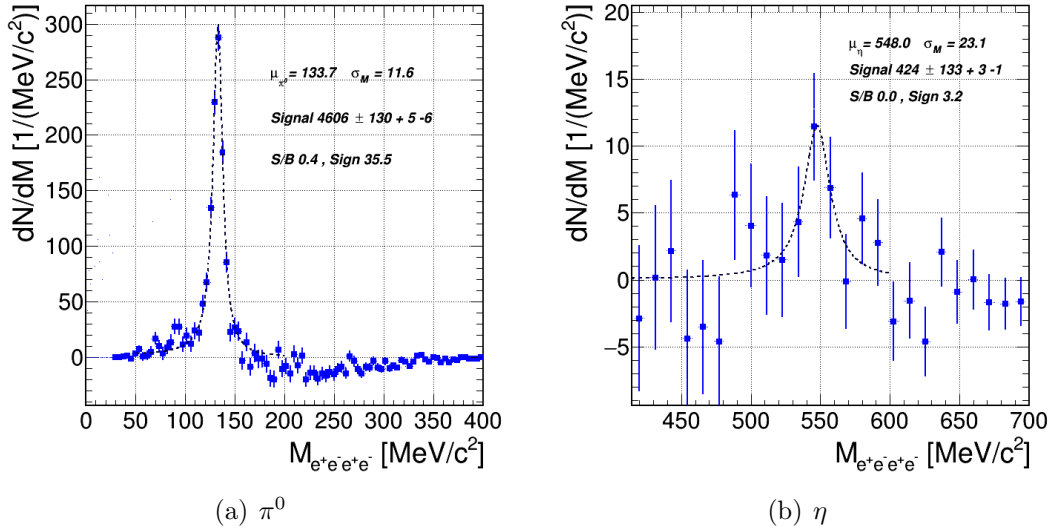
Figure 9.10: Four-lepton invariant mass spectra after subtraction of mixed-event
background for π^0 (a) and η (b) mesons, fitted with a Breit-Wigner function.

10   Corrections of the Raw Yield

The reconstructed raw spectra need to be corrected for detector imperfections like
the detection efficiency of the sub-detector systems together with the efficiency of
the used selection cuts (see Section 8.4). The limited geometrical acceptance also
has to be taken into account. Furthermore, the spectra need to be corrected for
the conversion probability P_{conv}. In this case, *conversion probability* describes the
probability that a photon converts into a lepton pair that can be reconstructed
in the spectrometer. Therefore the conversion probability, depends on the mass
of the decaying meson m_M, the phase space position $(p_\perp, Y)$ and the conversion
point $(x, y, z)|_c$.

10.1   Photon Conversion Probability

The decay of a photon into a lepton pair in vacuum is not possible due to momentum and energy conservation laws, even though it would be allowed from the quantum numbers. Energy conversation dictates that:

$$E_\gamma = E_{e^+} + E_{e^-}, \tag{32}$$

where E_γ is the energy of the photon, and $E_{e^\pm}$ the energies of the leptons. Further also the momentum of the photon must be conserved:

$$p_\gamma = p_{e^+} + p_{e^-}, \tag{33}$$

where p_γ is the momentum of the photon, and $p_{e^\pm}$ the momenta of the leptons. Even if the electron and positron move in the same direction, their total momentum cannot be as large as the momentum of the photon. Therefore, energy and momentum can not be conserved at the same time. Another body must take part in the reaction, meaning pair production can only occur when the photon passes nearby a massive particle such as an atomic nucleus. The recoil of the massive particle satisfies momentum conservation without carrying off a significant amount of energy, so the assumption that all of the energy of the photon goes into the electron-positron pair is a valid approximation. The cross section for this process depends on the atomic number Z of the material in which the interaction occurs and the incident photon energy E_γ. In this work, the GEANT simulation package was used to determine the conversion probability. The total cross section per atom for the conversion of a γ into an (e^+e^-) pair is parametrized as:

$$\sigma(Z, E_\gamma) = Z(Z+1) \left[F_1(X) + F_2(X)\,Z + \frac{F_3(X)}{Z} \right], \tag{34}$$

where $X = \ln(E_\gamma/m_e c^2)$. $F_n(X) = \sum_{n=0}^{5} c_n X^n$ where c_n are least-square fit parameters taken from data [Tul87]. The parameterization describes the data for nuclear charges between $1 < Z < 100$ and photon energies in the range from 1.5 MeV $< E_\gamma <$ 100 GeV. In a compound material the element i in which the interaction occurs is chosen randomly according to the probability:

$$p_{conv}(Z_i, E_\gamma) = \frac{n_i \sigma(Z_i, E_\gamma)}{\sum_i [n_i \cdot \sigma_i(E_\gamma)]}. \tag{35}$$

The calculation was preformed with photons from π^0 and η decays created with the Pluto event generator and propagated through the detector using GEANT. The mesons are generated in full phase space. Only if all four leptons hit material in the acceptance of the spectrometer the photons count as converted. In Figure 10.1 the conversion probability p_{conv} (in %) as function of different phase space components is shown. Detector efficiencies are not taken into account at this point.
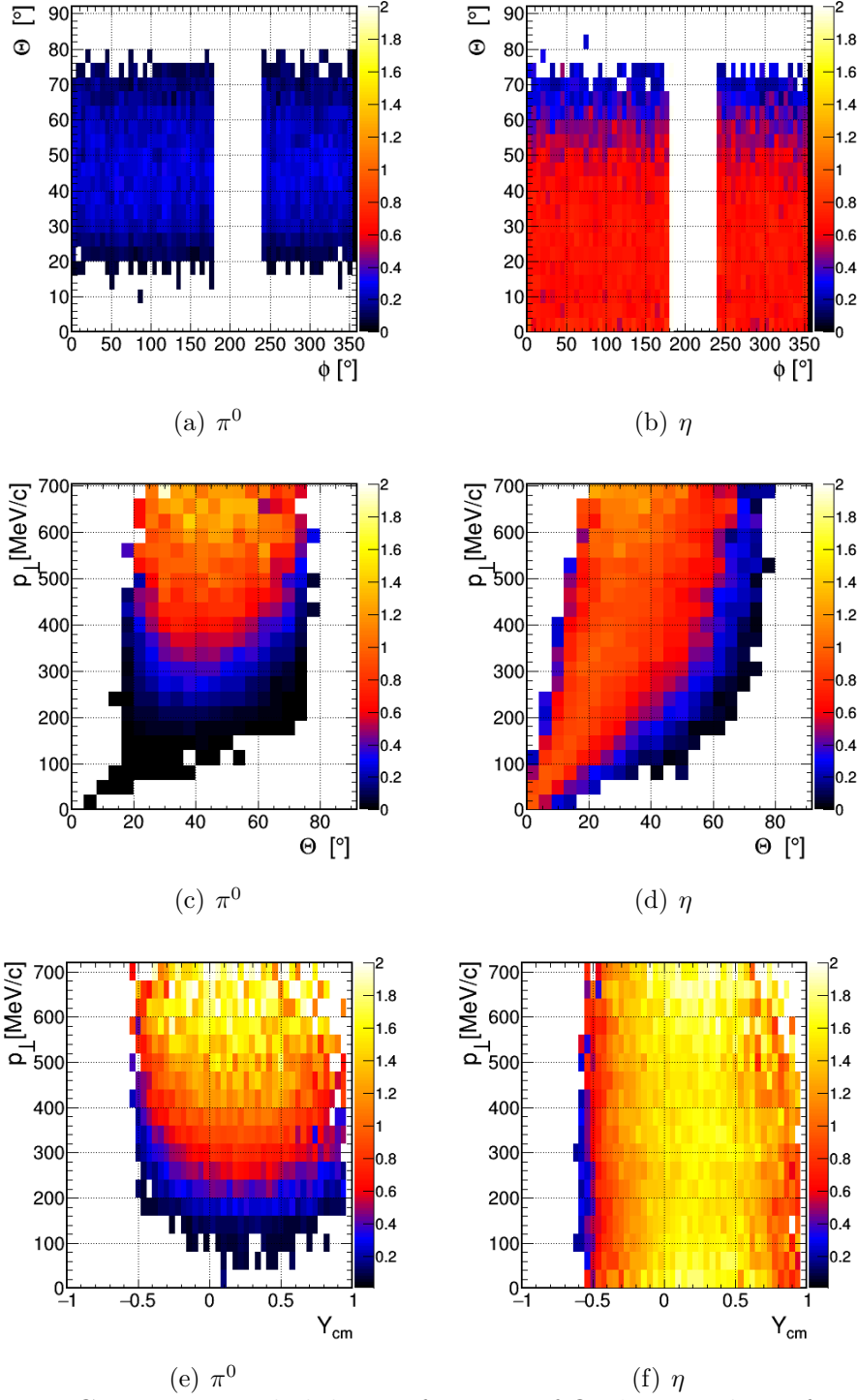
(a) π^0

(b) η

(c) π^0

(d) η

(e) π^0

(f) η

Figure 10.1: Conversion probability as function of Θ, ϕ, $p_\perp$ and Y_{cm} from π^0 (left column) and η (right column) decays.

The upper row shows the conversion probability in laboratory coordinates Θ and ϕ for π^0 (10.1(a)) and η (10.1(b)). In this representation the geometrical acceptance of the detector setup is visible. The distribution is for both cases structureless in azimuthal angle. Since the MDC chamber that covers $180° < \phi < 240°$ was not present in the $^{197}Au + ^{197}Au$ measurement it is excluded explicitly. The distributions are shown for the π^0 and η meson. Therefore, also regions where single particles do not have acceptance can be reached, like $\theta < 18°$. This effect is strongly pronounced for η, where the conversion probability at $\theta = 0°$ is non-zero due to the large opening angles $\Theta_{\gamma\gamma}$ (see Section 8.4) between the photons. In the second row of Figure 10.1 the conversion probability is shown as function of Θ and transverse momentum $p_\perp$. For the π^0 (Figure 10.1(c)) the conversion probability depends strongly on the transverse momentum of the meson. Using kinematics one can calculate that decay of a π^0 in rest leads to a photon momentum of $<p_\gamma> \approx 70$ MeV/c. These photons will convert into leptons with $<p_l> \approx 35$ MeV/c, which can not be detected in the HADES spectrometer due to strong deflections caused by magnetic field. As momentum of the π^0 grows, the acceptance increases. As shown in Equation 34 the conversion probability depends linearly on the momentum. The η meson has a higher mass and therefore the average momentum of the leptons increases to $<p_l> \approx 130$ MeV/c, which is high enough to be detected. In Figures 10.1(e) and 10.1(f) the conversion probability is shown in phase-space coordinates $(p_\perp, Y_{cm})$. The structures visible in the conversion probability distributions coming from momentum dependence of the process in combination with the geometrical acceptance is clearly visible.

In Figure 10.2 the projection of the conversion point of the photon in the radial $(r = \sqrt{x^2 + y^2})$ and z plane is shown. Various detector materials are indicated with different colors. Each material has a unique medium number which is associated by the simulation process (see Appendix E). The medium numbers are used to identify the conversion points. The uncertainties in the material budget are taken into account separately for the different materials. In the right panel of Figure 10.2 the RICH mirror with its characteristic round shape can be recognized (brown). The blue colored region shows conversion in the RICH radiator gas C_4F_{10}. Behind the mirror the δ-electron-shield (see Section 6.5) is visible. Parts of the MDCs are visible as well (cyan). Comparing to the other sources the contribution from the MDCs to the total conversion probability is minor and therefore not taken into account. The left panel is a "close-up" of the target region. One can see the segmented gold target (dark purple) and the target holder (light purple) made out of kapton. Furthermore, the beam pipe made out of kapton and steel (blue) and parts of the RICH support structure (green) can be identified. The conversion probability (in %) for the main contributing components is given in Table 10.2. Furthermore, the uncertainties of the material budget ΔP_{conv} are listed. This uncertainty directly affects the conversion probability and is therefore used to estimate the systematic uncertainties of the signal correction.
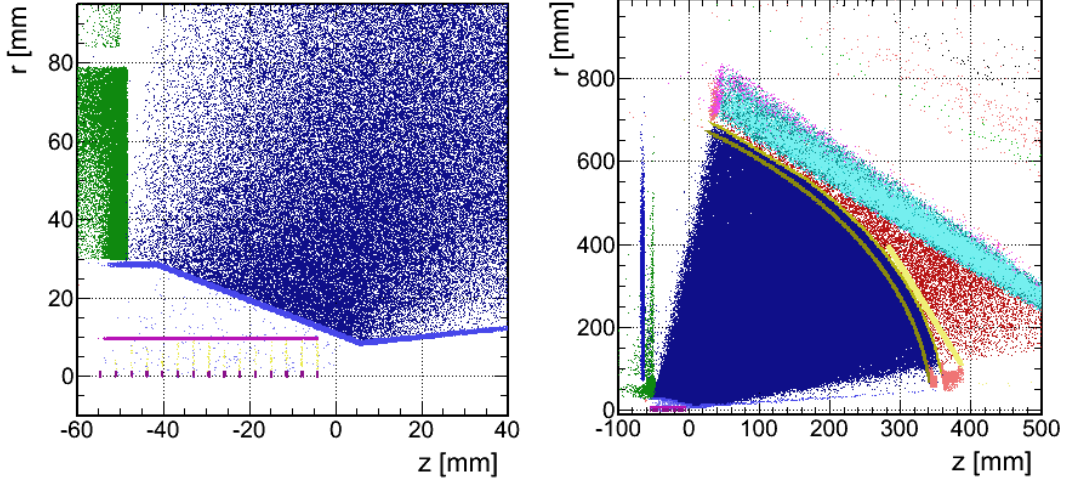
Figure 10.2: Vertex (radial,beam-axis) distribution of simulated leptons coming from photon conversion. Left zoom in in the target region, right full inner detector region. More details see text.

The total conversion probability for photons originating from π^0 is 0.78 % $\pm$ 0.12% and 1.55 % $\pm$ 0.23% for η respectively. The average effective branching

Object	Material	P_{conv} [%] (π^0)	P_{conv} [%] (η)	ΔP_{conv} [%]
Gold target	Au	0.14	0.34	1
δ-shield	C	0.07	0.06	1
Beam pipe	Fe	0.08	0.14	5
Radiator gas	C_4F_{10}	0.26	0.49	10
Mirror	C	0.16	0.30	10
Sum		0.78	1.55	15

Table 10.2: Conversion probability in geometrical acceptance for different materials. The GEANT number is given in the second column (See Appendix E).

ratio $\langle BR_{eeee} \rangle$ for the signal correction depends on the conversion probability and the branching ratios of the respective decay channels and is calculated as follows:

$$\langle BR_{eeee} \rangle = BR_{\gamma\gamma} \cdot P_{conv}^2 + BR_{\gamma e^+ e^-} \cdot P_{conv} + BR_{e^+ e^- e^+ e^-}, \qquad (36)$$

where P_{conv} is the conversion probability and BR_{eeee} (eeee are from $\gamma\gamma, \gamma e^+ e^-, e^+ e^- e^+ e^-$) are branching ratios in channels containing lepton pairs or photons, given in Table 1.1. Using Equation 36 the integrated average effective branching ratio is $\langle BR_{eeee}^\pi \rangle = 1.85 \cdot 10^{-4}$ and $\langle BR_{eeee}^\eta \rangle = 1.72 \cdot 10^{-4}$

10.2 Estimation of Signal Acceptance

The acceptance of an unstable meson can only be defined in terms of the acceptance of its decay products. Besides the pure geometrical coverage ($18° < \Theta_m < 85°$) of the spectrometer, the magnetic field influences the acceptance as well. In Figure 10.3(a) an event display of a simulated conversion pair is shown. The
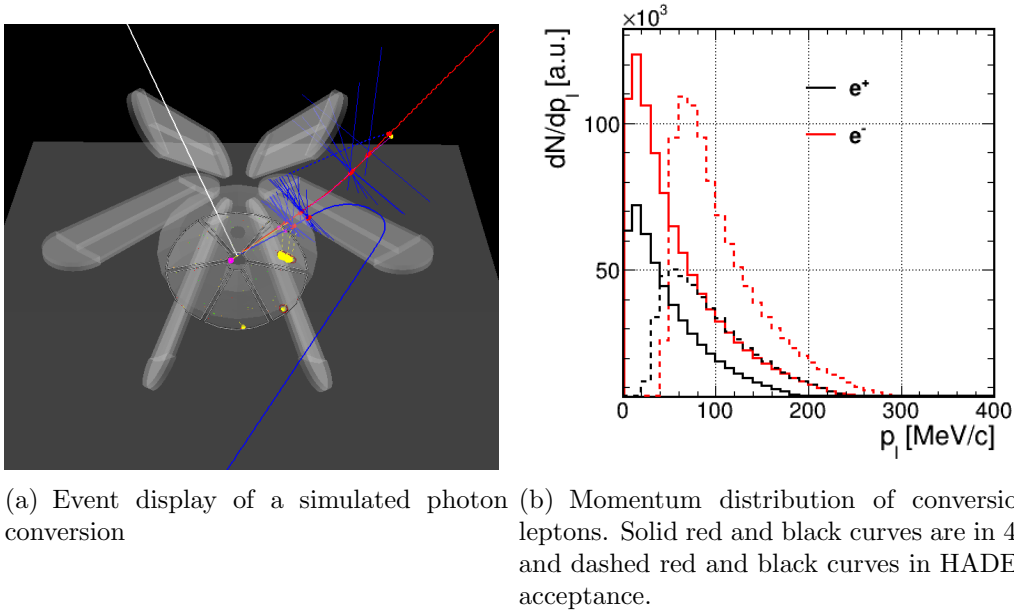

(a) Event display of a simulated photon conversion

(b) Momentum distribution of conversion leptons. Solid red and black curves are in 4π and dashed red and black curves in HADES acceptance.

Figure 10.3: Acceptance of decay products

positron (red trajectory) flies trough the spectrometer while the electron (blue trajectory) is bent out by the magnetic field before reaching the outer MDCs.

Pairs like this can not be reconstructed because of the missing acceptance of one of the decay/conversion partners. Figure 10.3(b) shows the momentum distribution of conversion leptons (e^-: red curves, e^+: black curves) in the full phase space (solid curves) and in the HADES acceptance (dashed curves). Note that the distributions are normalized to their integral for better visibility. Electrons with momentum smaller than 50 MeV/c and positrons with momentum smaller than 25 MeV/c are outside the acceptance. In Figure 10.4 the momenta distribution for the reconstructed four-lepton multiplets are
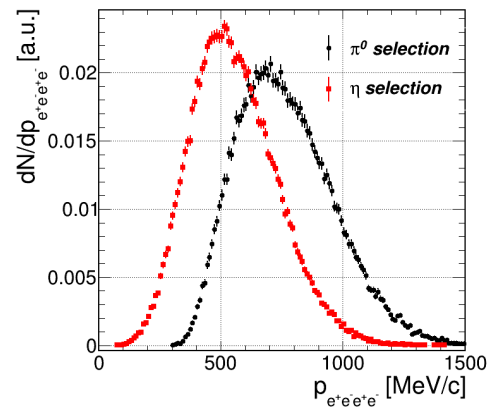

Figure 10.4: Momentum distribution of 4 lepton multiplet

shown. The black circles are multiplets after applying the topological selection for π^0 and red circles are those after η selection criteria. The transverse momentum of π^0 needs to be lager than ≈ 300 MeV while the transverse momentum of η larger than ≈ 50 MeV.

The momentum distribution of the meson is driven by its production mechanism. In general pion production can be described with mainly two components. More details of the pion production will be discussed in Section 11. Those mechanisms lead to different effective temperatures of the pion spectra. Due to isospin symmetry, expected temperatures of the π^0 should be the average of the temperatures of π^+ and π^-. In Figure 10.5 the phase space $(p_\perp, Y)$ distributions from Pluto

(a) π^0 in full phase space

(b) π^0 reconstructed

(c) η in full phase space
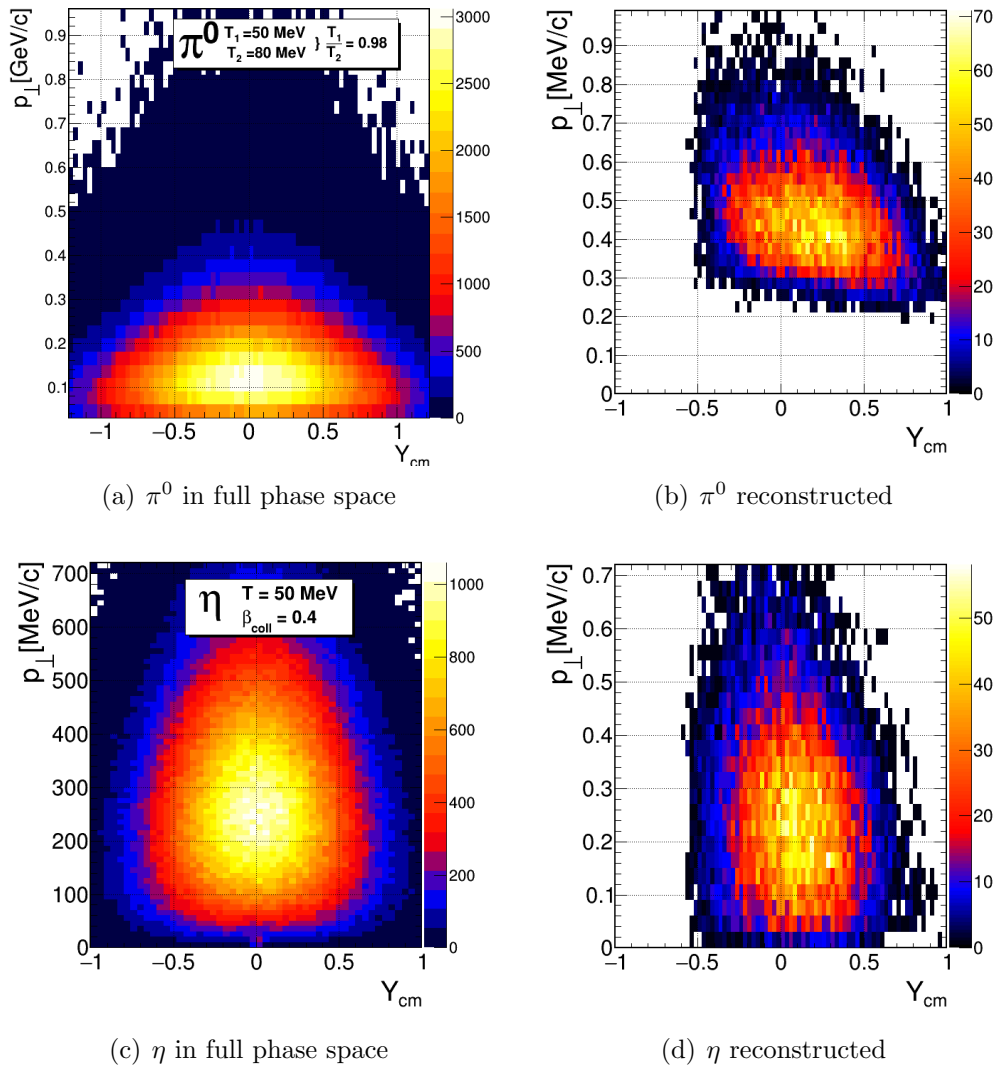
(d) η reconstructed

Figure 10.5: Simulated phase space in comparison with reconstructed phase space

simulations (left column) are shown in comparison with the reconstruction from real data (right column). For the π^0 (upper row) one can see that only a small part of the total yield is reconstructible. The analysis is only performed in the

region of 300 MeV/c $<$ p$_\perp$ $<$ 700 MeV/c and -0.3 $<$ Y$_{cm}$ $<$ 0.7. This region corresponds to only 10% of the produced yield. Therefore, the measured yield needs to be extrapolated to the full solid angle. For a systematical understanding of the method, the parameters ($T_1, T_2, T_1/T_2$ and β_{coll}) were varied. In Appendix D different variations are listed and for each combination the acceptance was estimated. The variance of the distribution is used as systematic uncertainties. For η the procedure was analogous, and corresponding figures are shown in the lower row of Figure 10.5. The obtained values are ϵ_{Acc}= 0.092 $\pm$ 0.02 for π^0 and ϵ_{Acc}= 0.629 $\pm$ 0.043 for η.

10.3   Estimation of Tacking Efficiency using Embedding

For the efficiency estimation of the sub detectors the particles need to be propagated through detector material and reconstructed, based on realistic detector response. Furthermore, tracks must be reconstructed in a realistic environment, namely in either a simulated or measured nuclear collision. The final detection of the mesons is strongly suppressed by the conversion probability and the acceptance. Reconstruction of π^0 and η using the conversion method from simulated nuclear collisions requires a large sample of simulated events. In most of the simulated events π^0 and η can not be detected because either one of the photons did not convert in the detector material or one of the four leptons is not accepted. To overcome this, leptons, with the properties of conversion leptons, are embedded into the collision events. The lepton pair properties like opening angle and the momentum are estimated according to known distribution (see Equation 34) within the Pluto event generator. They depend on the mass of the mother particle and the atomic number Z of the participating nucleus. These two parameters are used as input to the simulation. The decay of the mother meson and the conversion in a single dedicated material are simulated in Pluto. To understand the systematic uncertainties two different scenarios are implemented. In one case the whole
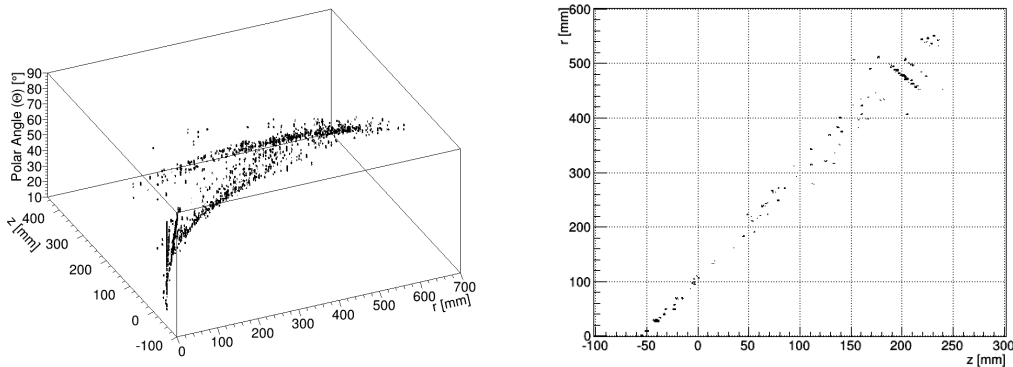
(a) Three dimensional distribution (Θ,r,z) for target segment one at z =-5 mm

(b) Two dimensional projection of 10 polar angle bins (here Θ_γ = 50-60°) for target segment one

Figure 10.6: Vertex distribution of embedded leptons.

material budget is assumed to be made from gold ($Z = 79$) and in the other case is it completely made from carbon ($Z = 6$). Details about the systematic uncertainties of that method can be found in Section 11.2. Uniformly distributed photons are simulated and their vertex distribution as a function of the target segment, transverse momentum ($p_\perp$) and polar angle (Θ) are extracted. In Figure 10.6(a) an example of such a three dimensional histogram (target segment one, z = -5 mm) is shown. Figure 10.6(b) shows a projection of ten polar angle bins (here $50 < \Theta < 60°$). The vertex (r,z) of a lepton pair with a given polar angle is then randomly generated according to the probability distribution of the two dimensional histogram. Each r is randomized with an azimuthal angle (ϕ) between 0 and 360° and then transformed into Cartesian coordinates. The procedure is repeated for each lepton pair independently. The simulated leptons are then embedded in events of three days (107, 108 and 109) of the APR12 run.
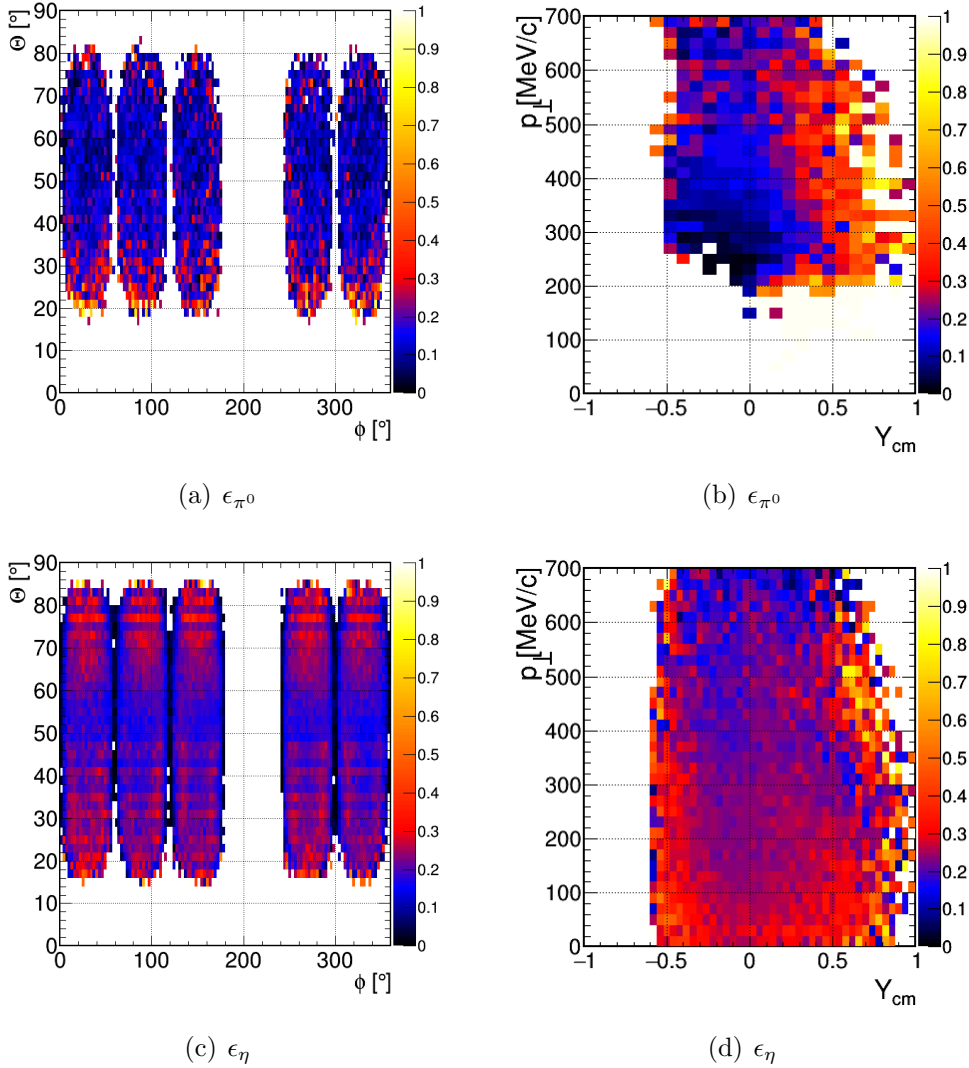

(a) ϵ_{π^0}

(b) ϵ_{π^0}

(c) ϵ_η

(d) ϵ_η

Figure 10.7: Efficiency ϵ, a function of Θ, ϕ, $p_\perp$ and Y_{cm} from π^0 (left column) and η (right column) decays.

The total efficiency (ϵ_{tot}) is calculated in $\Theta, \phi/p_\perp, Y$ dimensions, by dividing the number of reconstructed mesons (which means four reconstructed leptons coming from the same candidate) by the number of accepted mesons. A meson is called accepted when it triggers passes the active material in all MDC chambers of one sector. The total efficiency includes the tracking efficiency (ϵ_{rec}) as well as the identification efficiency (ϵ_{pid}). In Figure 10.7 the total efficiencies ($\epsilon_{tot} = \epsilon_{rec} \cdot \epsilon_{pid}$) in laboratory frame and in $p_\perp, Y$ coordinates are shown. The efficiency for the π^0 (upper row) is uniform in geometrical coordinates (10.7(a)), but depends strongly on the momentum (see i.e. [Gal09]). The low momentum leptons have a lower reconstruction efficiency due to multiple scattering. In contrast, the tracking efficiency for the η is uniform in $p_\perp, Y_{cm}$ due to the higher momentum of the leptons. In Table 10.3 the total efficiencies obtained for the different mesons and the different assumptions for conversion materials are listed. In the last row the average of both assumptions for conversion materials is given and the variance of the values is used as systematic uncertainty for the reconstructed yield.

	Z	ϵ_{rec}	ϵ_{pid}	ϵ_{tot}
π^0	6	0.460	0.393	0.181
	79	0.470	0.392	0.185
	mean			0.183 ± 0.010
η	6	0.487	0.508	0.247
	79	0.440	0.530	0.233
	mean			0.240 ± 0.030

Table 10.3: The total efficiency ϵ_{tot} of π^0 and η reconstruction assuming different conversion materials

11 Corrections of Raw π^0 Spectra

In order to extract the effective slope parameter and the reconstructed meson yield, the corrections have to be applied to the measured data differentially in $m_\perp, Y_{cm}$. The transverse mass of a particle with mass m_M is:

$$m_\perp = \sqrt{m_M^2 + p_\perp^2} \tag{37}$$

Under the assumption that production of the particles will occur only when the fireball reaches equilibrium in temperature, volume, and μ_B, kinetic gas theory can be applied [BS07, Max67, Rei08]. The transverse mass spectra can be plotted in the so-called Boltzmann representation :

$$\frac{1}{m_\perp} \frac{dN}{dm_\perp dY} = C(Y) \exp \frac{(m_\perp - m_M)c^2}{T_B(Y)} \tag{38}$$

where m_M is the mass of the meson, $T_B(Y)$ the inverse slope parameter and C(Y) a constant. The inverse slope provides information on the temperature at which inelastic interactions no longer occur, the so-called chemical freeze-out. The transverse mass spectra of π can be described with two slope parameters, which are interpreted by two different production mechanism. While the majority of the spectrum is coming from decay of resonances (lower $m_\perp$), only a small fraction is produced thermally (higher $m_\perp$) [Sch16]. Particles at lower transverse masses ($m_\perp < 200$ MeV/c^2) have steeper slope, particles at higher transverse masses ($m_\perp > 200$ MeV/c^2) show a more shallow slope. The spectrometer has only a limited acceptance and leptons with momentum lower then 50 MeV/c are bent out of the acceptance by the magnetic field. An extrapolation to unmeasured regions is impossible without a bias from underling models. Particles with higher transverse mass are not affected by this. In the following, the integrated spectrum is divided in differential phase-space bins in transverse mass $m_\perp$ and rapidity in the center of mass system Y_{cm}. The phase space coverage, in M_{eeee} as function of Y_{cm}

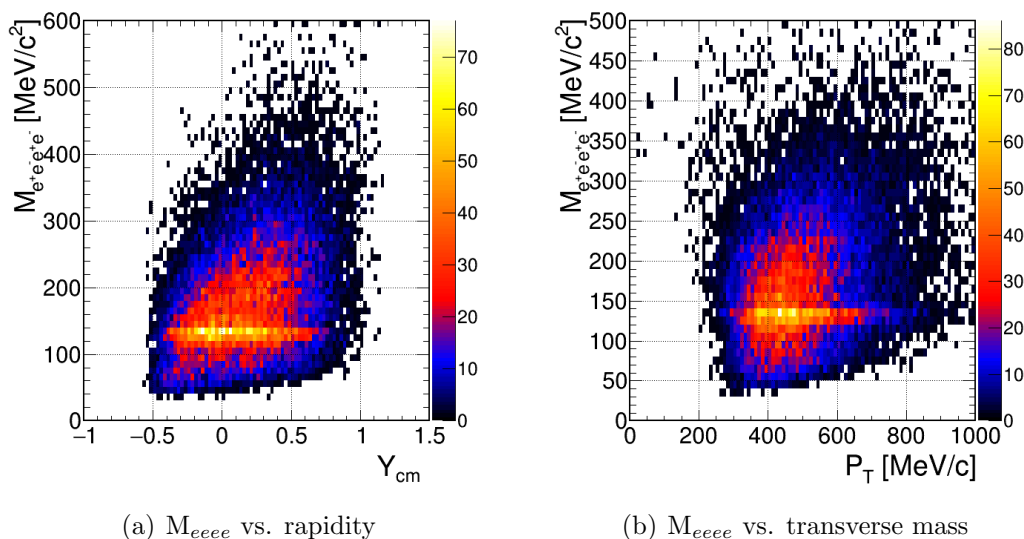(a) M_{eeee} vs. rapidity   (b) M_{eeee} vs. transverse mass

Figure 11.1: Phase space coverage of four-lepton multiplet in invariant mass as a function of rapidity (a) and transverse mass (b).

representation, is shown in Figure 11.1(a). At an invariant mass of ≈ 135 MeV/c^2 the π^0 mesons are visible as a horizontal band. This band covers a rapidity range from -0.4 < Y_{cm} < 0.7. A similar structure is visible for M_{eeee} as function of transverse momentum distribution, shown in Figure 11.1(b). The coverage is from 300 < $p_\perp$ < 700 MeV/c. The integrated spectrum is divided in ten rapidity bins of width = 0.1 and eight transverse mass bins of 50 MeV/c. In Figure 11.3 the invariant mass spectra together with results of the mixed-event background for the mid-rapidity bin (Y=0.77) are shown. The invariant mass spectra for the other rapidity bins can be found in Appendix F. The mixed-event method describes the background satisfactory in each $m_\perp$ bin. After subtraction of the

background, the resulting signal peak is fitted with a Breit-Wigner distribution and integrated in a ± 3 sigma window around the mean peak position. The resulting yields (Figure 11.4(a)) are corrected with the conversion probability factor P^*_{conv} (Figure 11.4(b)) and efficiency ϵ (Figure 11.4(c)) and plotted in the $m_\perp$-m_0 representation. The statistical uncertainties can be found in Appendix C. The systematic uncertainties for the efficiency are shown in Figure 11.4(c) as shaded boxes. In Figure 11.2 the transverse mass spectra are shown for the different rapidity bins (from backward to forward rapidity - up to down). Bins with a statistical uncertainty larger than the signal are excluded. Those are located at the edge of the acceptance (see Figure 11.4(a)). The resulting $m_\perp$ spectra are fitted with a single slope exponential function to obtain the inverse slope parameter. The total yield is calculated by integrating the corrected $m_\perp$ yields for each rapidity bin.
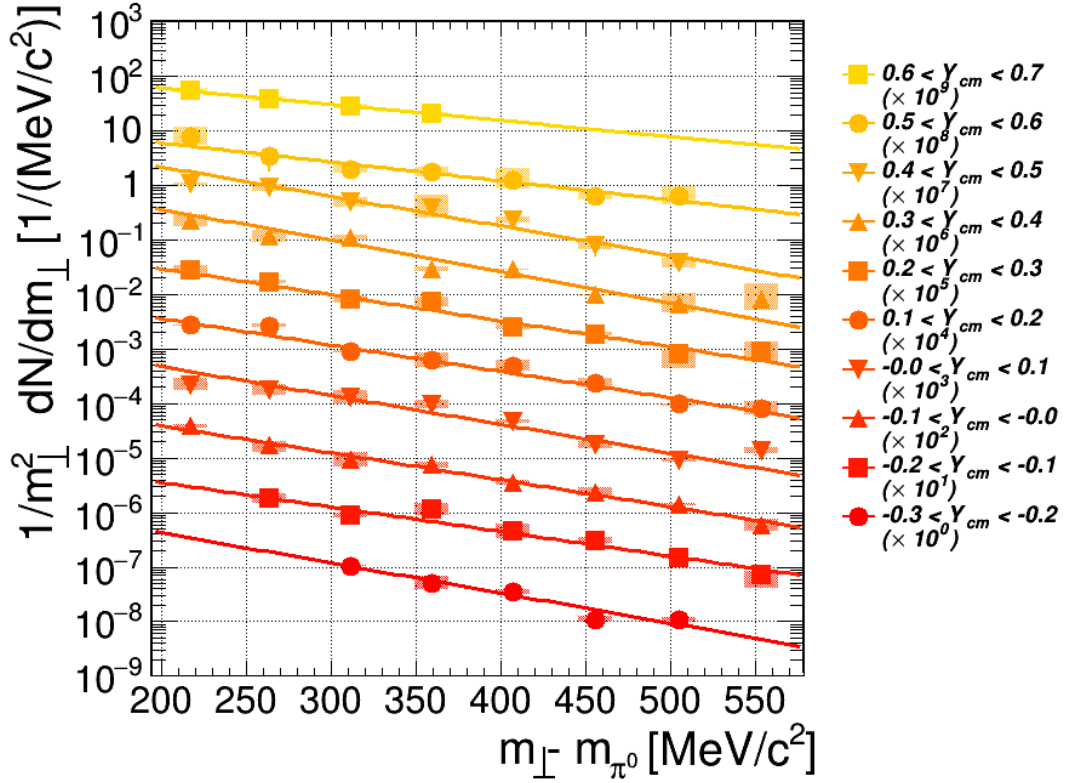

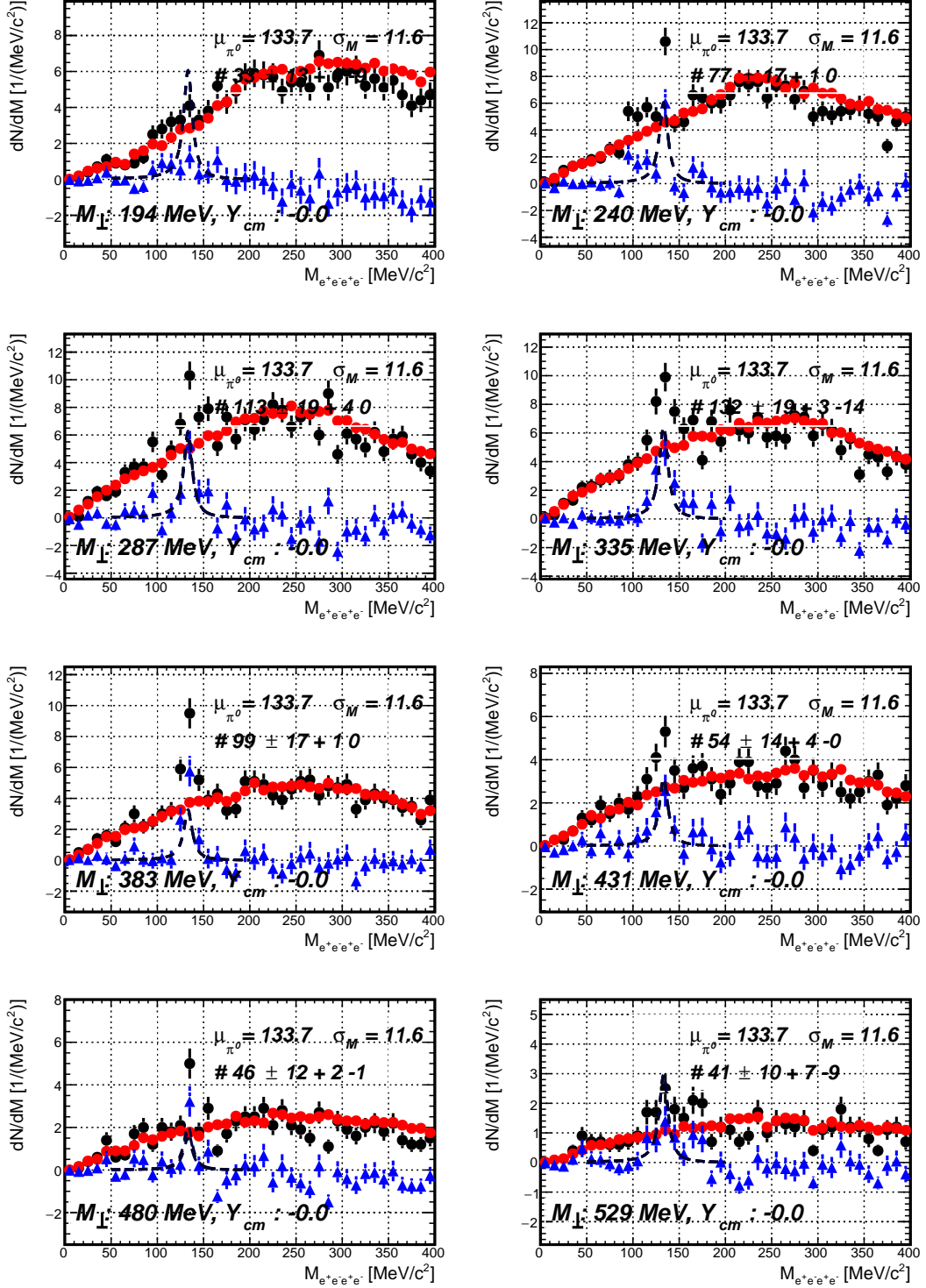Figure 11.2: Differential π^0 spectra in Boltzmann representation fitted with a single slope exponential function.

Figure 11.3: Phase space dependent four-lepton invariant mass spectrum with mixed-event background (red)
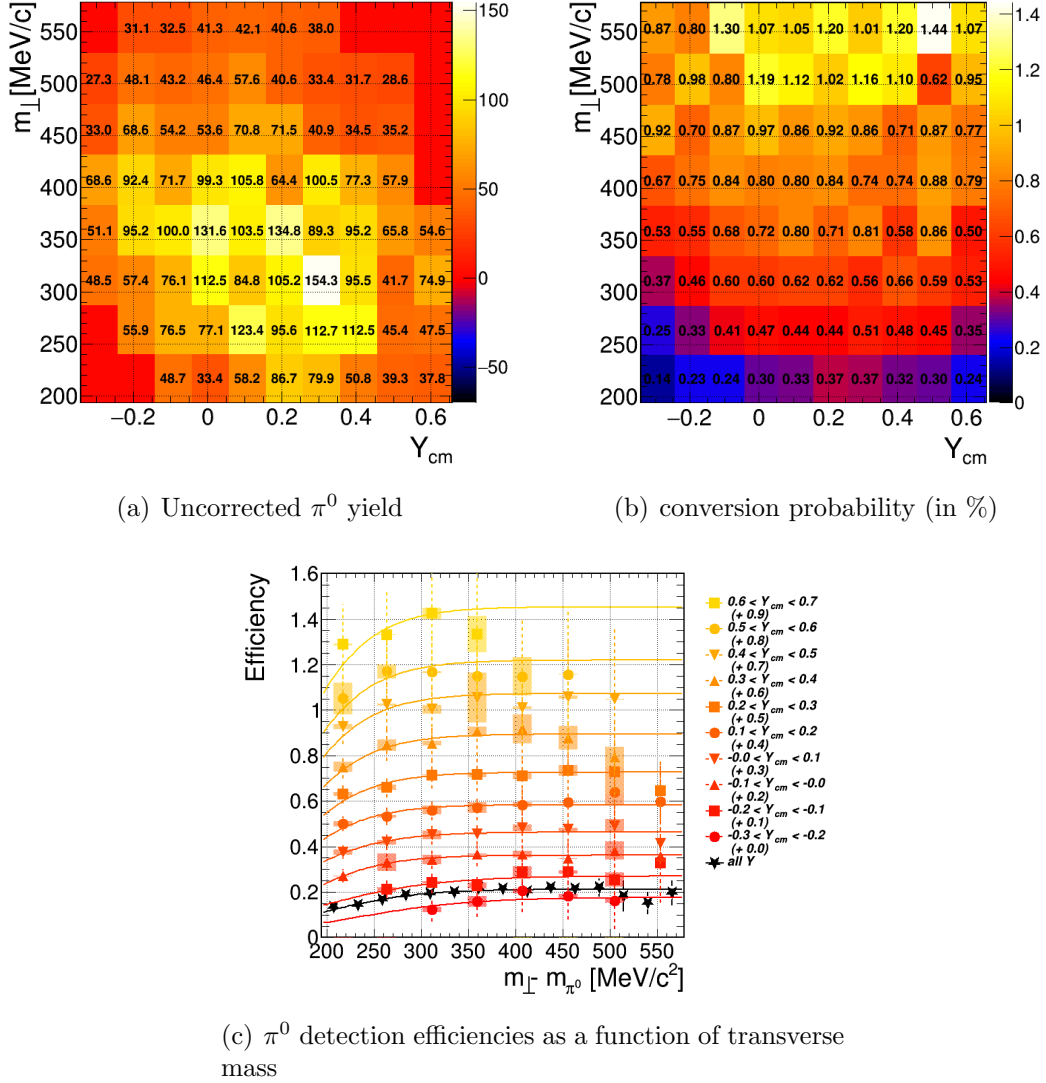
(a) Uncorrected π^0 yield

(b) conversion probability (in %)

(c) π^0 detection efficiencies as a function of transverse mass

Figure 11.4: Phase space coverage in $m_\perp$ vs. Y plane. (a) uncorrected counts of π^0 (b) conversion probability (c) reconstruction efficiency

11.1   Reconstruction of π^0 Inverse Slope parameter

For the extraction of the inverse slope parameter the corrected $m_\perp$ spectra are fitted with a single slope exponential function. At low $m_\perp < 200\text{-}300$ MeV/c^2, the main production mechanism for pions is Δ resonance decay. This slope can not be extracted due to missing acceptance. To obtain a valid fit range the quality of a single slope fit is estimated using a χ^2 distribution and p-value test of the fit as quality criteria (See Figure 11.5). Using the fit range with the χ^2 value closest to 1 and the highest p-value leads to an inverse slope distribution shown as a function of rapidity in Figure 11.6. The closed circles are the measured data.

The open circles are reflected around mid rapidity. The effective temperature T_{eff} for an isotropically emitting thermal source describes mid rapidity and can be depicted with this simple dependence:

$$T_B(Y) = \frac{T_{eff}}{\cosh(Y)}, \tag{39}$$

where $T_B(Y)$ is the inverse slope parameter in each differential $m_\perp$ spectrum. The inverse slope parameter spectrum in Figure 11.6 is fitted with a $1/cosh(Y)$ distribution. The resulting T_{eff} is 84.7 ± 1.8 MeV. The systematic uncertainties are shown as red boxes and will be discussed in the following section.
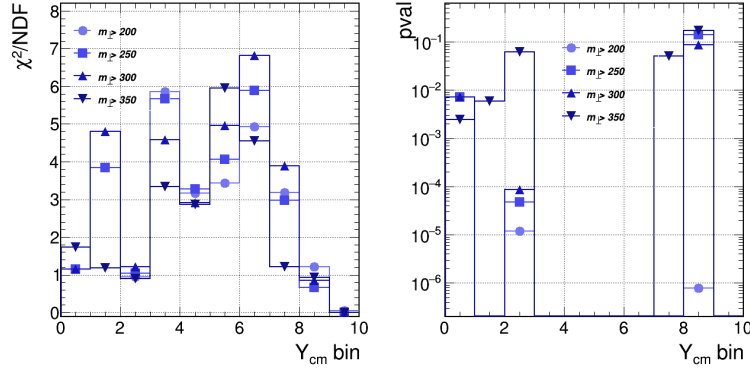

Figure 11.5: Quality criteria for the phase space differential one slope fit to the $m_\perp$ of π^0 spectra
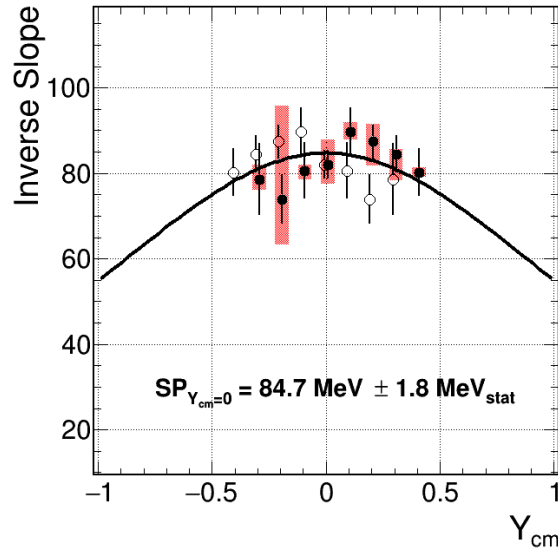

Figure 11.6: Inverse slope parameter as function of rapidity. Solid curve represents $1/\cosh(Y_{cm})$ fit.

11.2   Systematic Uncertainties of the Inverse Slope Parameter

Systematic uncertainties are uncertainties that can not be minimized by increasing size of the data sample. In this analysis the used selection criteria, the corrections for acceptance and efficiency and the uncertainties in the material budget, and therefore the conversion probability, are the main contributions these uncertainties. The uncertainties of the correction for the raw yield are calculated point-by-point, while the chosen binning and topological selection criteria are estimated for the integrated yield. The systematic uncertainty of the average effective branching ratio is calculated point-by-point according to the following formula:

$$\Delta BR_{eeee} = BR_{\gamma\gamma} \cdot (1 \pm \Delta P_{conv})^2 + BR_{\gamma e^+ e^-} \cdot (1 \pm \Delta P_{conv}) + BR_{e^+ e^- e^+ e^-}. \quad (40)$$

where ΔP_{conv} is the uncertainty of the material budget listed in Table 10.2 and BR_{eeee} (coming from $\gamma\gamma$, $\gamma e^+ e^-$, $e^+ e^- e^+ e^-$) are branching ratios in channels containing lepton pairs or photons, given in Table 1.1. The systematic error of the efficiency is also estimated point-by-point using the Z=6 embedding as minimum and the Z=79 embedding as maximum value (see Chapter 10.3). The point-by-point systematic error is shown in Figure 11.4(c) as shaded areas around the points. The raw yields are corrected with the minimum/maximum correction and fitted with a single slope exponential fit, similar to equation 38. The resulting $m_\perp$ fits are shown in Figure 11.7(a) as dashed lines. The obtained inverse slope parameters are shown in Figure 11.6 as red boxes and fitted with a $1/\cosh(Y)$ distribution which leads to T_{eff} with an error of +4.1 MeV and -6.1 MeV. In addition, the contributions to the systematic uncertainty are estimated by variation of the bin size and the identification criteria as described in Section 8.2. In Figure 11.8 the reconstructed four-lepton invariant mass M_{eeee} as a function of the topological
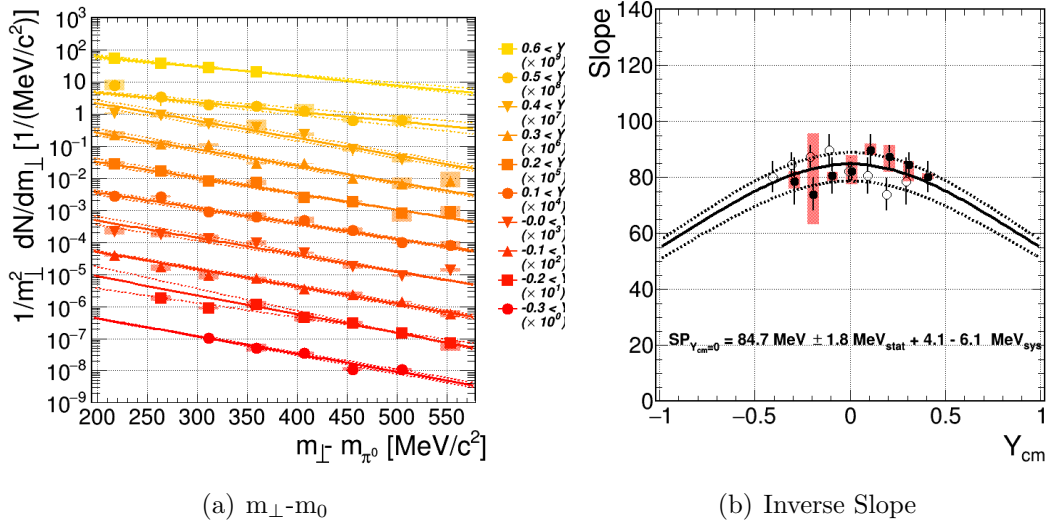

(a) $m_\perp$-m_0

(b) Inverse Slope

Figure 11.7: Systematic of ϵ_{Eff} and P_{conv}

observables is shown. On the left panel (Figure 11.8(a)) the invariant mass is shown as function of the opening angle between the leptons α_1, α_2. The "band" at an invariant mass of $M_{eeee} = 135$ MeV/c^2 corresponds to the reconstructed π^0 yield. The smaller opening angle α_1 is varied by one degree, while the lager opening angle α_2 is changed by 2.5 degrees. The opening angle between the reconstructed photons $\Theta_{\gamma\gamma}$ is shown in Figure 11.8(b). Since no cut was applied to $\Theta_{\gamma\gamma}$ the angle is not varied. The lepton identification criteria is varied as well. The number of bins in the four lepton invariant mass spectra, as well as the bin size of the $p_\perp$ are varied, too. Table 11.4 summarizes the various variation and the resulting T_{eff} values. The differences between the values are smaller than the systematic errors coming from the efficiency and conversion probability correction and can therefore be neglected.
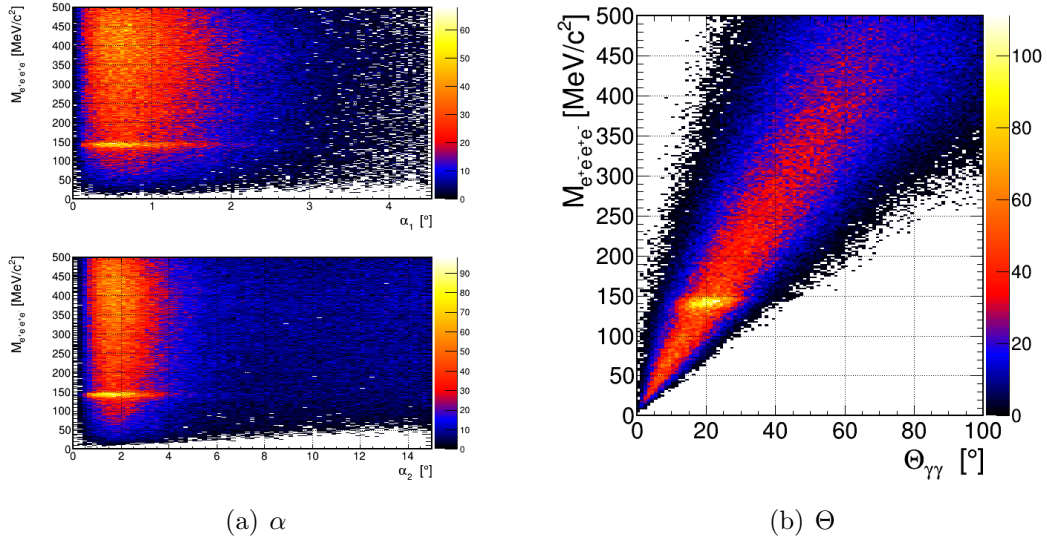

(a) α (b) Θ

Figure 11.8: Reconstructed invariant mass as function of α (a) and Θ (b). For the reconstruction the topological selection for π^0 is used.

α_1 [°]	α_2 [°]	m_l^2 [MeV^2]	N$_{Bins}$ M$_{inv}$	Bin size p$_\perp$ [MeV/c^2]	T_{eff} [MeV]
4.5	10.0	5000	100	50	83.9 ± 1.9
3.5	7.5	5000	100	50	83.0 ± 1.9
5.5	12.5	5000	100	50	83.5 ± 2.0
4.5	10.0	4000	100	50	86.0 ± 2.2
4.5	10.0	3000	100	50	83.0 ± 2.2
4.5	10.0	5000	125	50	84.4 ± 1.9
4.5	10.0	5000	75	50	84.3 ± 1.9
4.5	10.0	5000	100	75	89.4 ± 1.7

Table 11.4: Variation of the topological selection

11.3   Reconstruction of Meson Yields

To extract the total number of π^0 per event, an extrapolation to the full phase space is needed. This can be achieved by fitting the corrected data in a Boltzmann representation (see Equation 38) and extrapolating to the unmeasured region. In Figure 11.2 the $m_\perp - m_0$ spectra of the π^0 are shown. Due to the limited acceptance of low-momentum leptons, the transverse mass $m_\perp - m_0 < 200$ MeV/c^2 can not be covered. In this uncovered region pions are expected to show a different slope compared to the measured region. Therefore, an extrapolation in the unmeasured regions is not possible without introducing uncertainties. The efficiency and conversion probability corrected data are plotted as a function of rapidity in Figure 11.9 as black circles. Point-by-point systematic errors (shaded red areas around the points) are obtained similar to the systematic uncertainties of the slope, described in Section 11.2. The open circles are data points reflected with respect to mid-rapidity. The overlapping of the reflected and the measured yields confirms the symmetry of the yield. They are fitted with Gaussian distribution, which is the simplest assumption. In a full thermally produced yield the width of the dN/dY distribution can be described as:

$$\sigma_{Gauss} = \sqrt{\frac{T_{eff}}{m_0 c^2}}.\tag{41}$$

Using the obtained T_{eff} the expected width of the dN/dY is 0.78 ± 0.23.
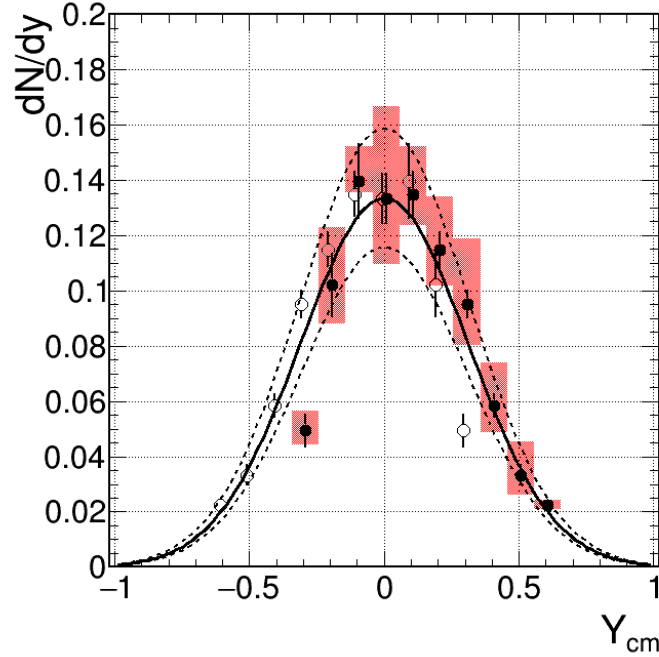

Figure 11.9: Corrected yield as a function of rapidity fitted. Black solid curve: Fit of a Gaussian function to the spectrum. Black dashed curves, fit to the systematical varied points.

The width of the fit shown in Figure 11.9 is $0.31 \pm 0.01_{sys}$. The yield is measured only in a small acceptance region and the difference in the width is therefore expected. Integrating the data points the total yield in the acceptance region gives $\mathrm{Mult}_{Acc}^{\pi^0} = 0.88 \pm 0.03_{stat} \pm 0.16_{sys}$. The acceptance and its uncertainties are determined in Section 10.2. The yield extrapolated to full phase-space is

$$Mult_{4\pi}^{\pi^0} = 9.70 \pm 0.27_{stat} \pm 1.8_{sys} \pm 1.3_{extrap}. \tag{42}$$

Further systematic uncertainties are obtained by variation of the selection criteria and the bin size of the invariant mass, as well as the size of the $p_\perp$ bins analogous to the inverse slope systematic uncertainty determination. The resulting values (Shown in Table 11.5) agree within the uncertainties and can therefore be neglected.

α_1 [°]	α_2 [°]	m_l^2 [MeV^2]	N$_{Bins}$ M$_{inv}$	Bin size p$_\perp$ [MeV/c^2]	N$_{\pi^0}$ (PT3)
4.5	10.0	5000	100	50	9.73
3.5	7.5	5000	100	50	9.81
5.5	12.5	5000	100	50	9.88
4.5	10.0	4000	100	50	9.52
4.5	10.0	3000	100	50	9.26
4.5	10.0	5000	125	50	9.65
4.5	10.0	5000	75	50	9.81
4.5	10.0	5000	100	75	10.17

Table 11.5: Variation of the topological selection

Due to limited statistics a phase-space dependent analysis of the η meson can not be performed. The number of η mesons can be determined similarly to the integrated π^0 multiplicity. The result is:

$$Mult_{4\pi}^{\eta} = \frac{N_\eta^{rec}}{\epsilon_{tot} \cdot Acc \cdot p_{conv}^* \cdot N_{evts}} \tag{43}$$

Where p_{conv}^* is the conversion factor analogous to the one in Equation 36. The total yield results in:

$$Mult_{4\pi}^{\eta} = 0.107 \pm 0.005_{stat} \pm 0.028_{sys} \pm 0.007_{extrap}. \tag{44}$$

The systematic uncertainty is calculated taking the uncertainties from Section 11.2. Hence, the uncertainty values of the correction factors are, $P_{conv}^* = 15\%$, ϵ_{rec} and ϵ_{pid} together $= 5\%$ and $Acc_{pluto} = 15\%$. Since the systematic variation of the selection criteria does not show systematic uncertainties larger compared to the one from the correction method they can be neglected.

Part IV
Discussion and Outlook

> *The problem is not the problem.*
> *The problem is your attitude about the problem.*
> *Do you understand?*

Captain Jack Sparrow

In the following chapter the obtained HADES results will be compared with previous measurements from TAPS and KaoS collaborations, as well as with theoretical model calculations. In addition, the π^0 yield and transverse mass distribution will be compared with the charged pion results from the same measurement campaign [Sch16]. Finally, π^0 and η multiplicities have been used to create the dilepton cocktail using the Pluto event generator. The reconstructed dilepton spectra [Sel16, Har16a] in the ^{197}Au+^{197}Au collisions at 1.23 GeV/u will be discussed in Section 15.

An important issue to be taken into account when comparing results from various experiments is the centrality selection. Most of the experiments mentioned above measured in so-called minimum-bias events. Therefore, HADES results need to be extrapolated to minimum-bias collisions. The event class used in this analysis is 43% of ^{197}Au+^{197}Au most central collisions, which corresponds to a mean number participants of $A_{part} = 180$ (according to Glauber simulations from [Kar15]). In a minimum bias ^{197}Au+^{197}Au collision the number of participants is $A_{part} = 91.7$. Data from TAPS and KaoS showed that the number of produced mesons depends on the number of participants in the collision. The multiplicity section of neutral mesons follows a power law [R$^+$07]:

$$\frac{Mult_m}{A_{part}} = cA_{part}^{\tau-1} \qquad (45)$$

where c is a normalization constant, $\tau_{\pi^0} = 0.77\pm 0.1$ and $\tau_\eta = 1.15 \pm 0.20$. Equation 45 will be used to extrapolate the mean yield to the respective centrality class of the model calculations and data. The uncertainty of this procedure is given as sys$_{extrap}$. With this, the number of mesons in minimum bias collisions can be extrapolated to:

$$Mult_{b_{max}}^{\pi^0} = 5.75 \pm 0.16(stat) \pm 1.07(sys) \pm 0.79(acc) \pm 0.40(sys_{extrap}) \qquad (46)$$

and

$$Mult_{b_{max}}^{\eta} = 0.049 \pm 0.002(stat) \pm 0.013(sys) \pm 0.003(acc) \pm 0.007(sys_{extrap}) \qquad (47)$$

12   Comparison of π^0 Yield with Results of $\pi^\pm$

As pointed out earlier, HADES provides high-quality data on charged hadrons. Identification of charged pions, using their velocity information (details see[Sch16]), is performed in the 40% most central events. To validate the reconstructed π^0 multiplicity one can compare it with $\pi^\pm$. In Figure 12.1 the obtained centrality dependent dN/dy spectra are shown for π^- (left panel) and π^+ (right panel). Extrapolation to unmeasured phase-space regions using a Gaussian fit and integration over this spectrum gives the $M_{\pi^\pm}$ per centrality class. Due to isospin conservation the ratio of charged to neutral pions in a symmetric system (like ^{197}Au+^{197}Au) is fixed:

$$Mult(\pi^0) = \frac{Mult(\pi^+) + Mult(\pi^-)}{2}. \tag{48}$$

In Figure 12.2 the transverse mass spectra of charged pions are shown together with neutral pions in the Boltzmann representation. They are normalized to the number of analyzed events for comparison. Charged pions have a much lager acceptance 50 MeV/c^2 $<m_\perp - m_0<$ 800 MeV/c^2 and much higher statistics. In addition, following Equation 48, the average multiplicity of $\pi^\pm$ is shown with blue circles.

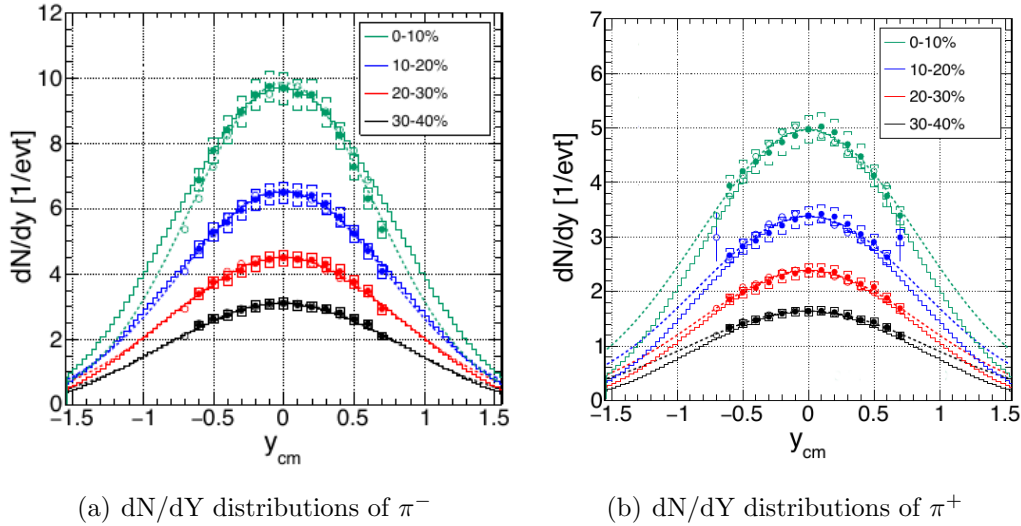(a) dN/dY distributions of π^- (b) dN/dY distributions of π^+

Figure 12.1: dN/dY distributions from charged pions for different centralities. Thanks to the large data sample statistical errors are not visible. Systematic error are shown as boxes. Full symbols show the measurements and open symbols show the reflection around mid-rapidity. The dotted curves are Gaussian fits, used for extrapolation. dN/dy distribution from UrQMD are shown with solid lines, and used to estimate systematic uncertainties from the extrapolation.

In the region where the acceptances for charged and neutral pions overlap (200 $<m_{\perp} - m_0<$ 800 M/c^2) the averaged $\pi^{\pm}$ agree with the measured π^0 distribution from this work. This agreement is a validation of the method and makes the results on the η production more solid. In Table 12.1 the yield and inverse slope parameter of $\pi^{\pm}$ in 40% most central events are listed together with those for π^0. Their average agrees with the values for neutral pions obtained from this work.

	π^-	π^+	$1/2(\pi^+ + \pi^-)$	π^0
T$_2$ [MeV]	88 $\pm$ 2	86 $\pm$ 2	87 $\pm$ 4	84.7 $\pm$ 6.1
Multiplicity (0-40%)	12.0 $\pm$ 0.71	6.7 $\pm$ 0.61	9.35 $\pm$ 1.32	10.11 $\pm$ 2.4

Table 12.1: Comparison of inverse slope parameter and multiplicity from charged and neutral pions
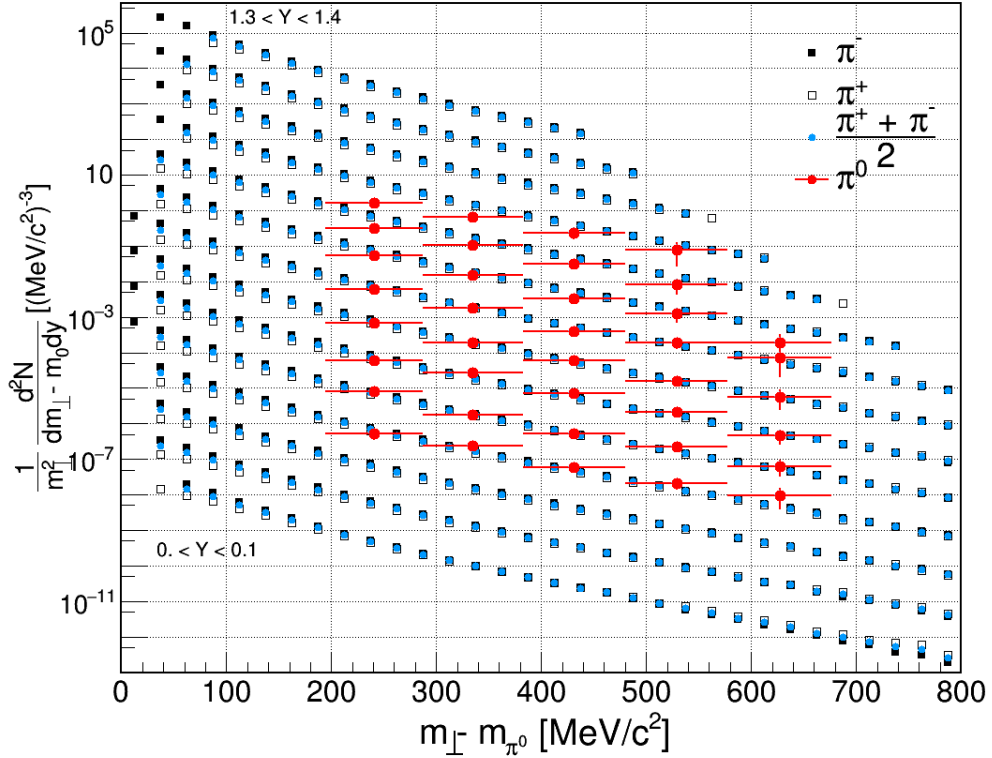

Figure 12.2: Comparison of $m_{\perp} - m_0$ distribution of π^0 and $\pi^{\pm}$ for rapidity ranges $0.0 < $ Y $ < 1.4$. Open squares are π^+, closed squares are π^-. Statistical errors are not visible. The blue circles are the average between $\pi^{\pm}$, while red circles are π^0 from this work.

13   Systematics of π^0 and η Production

Extracted π^0 and η yields are compared with the world data as shown in Figure 13.1. The multiplicity as a function of collision energies is shown for various collision systems. Data are taken from [ea97, AHMS03, W$^+$98, BPS$^+$94, A$^+$97, SP$^+$94, M$^+$97, M$^+$99]. The multiplicities for π^0 and η mesons from this work are shown as stars (π^0: red star, η: blue star). The obtained multiplicities agree with the predicted extrapolation curves.
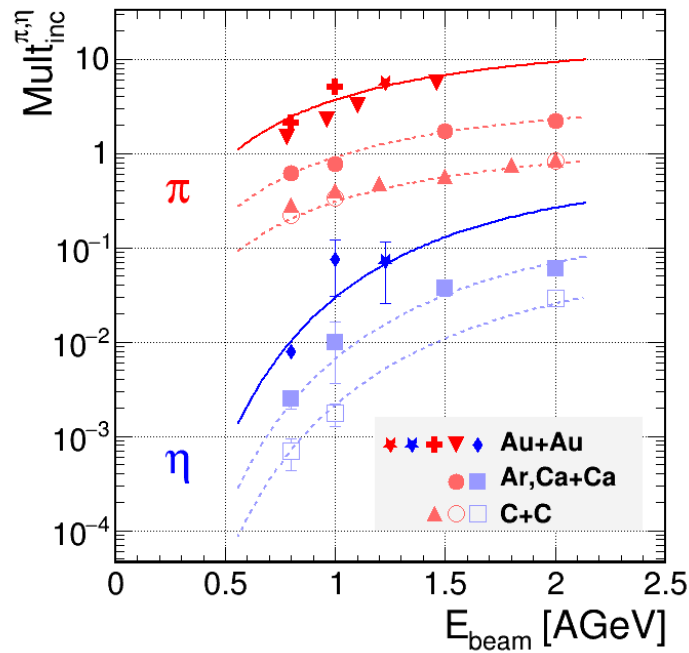

Figure 13.1: Production cross section for different systems and energies measured with the TAPS. The red symbols show the π and the blue the η yields. Triangles show the charged pion measurement from KaoS in ^{12}C+ ^{12}C and (upside down triangles) ^{197}Au+^{197}Au. The open symbols are the measurements in ^{12}C+ ^{12}C reactions. Closed red circles are π^0 measured in ^{40}Ca+ ^{40}Ca, and the blue closed squares are the respective η multiplicities. The red crosses are neutral pions from ^{197}Au+^{197}Au collisions and blue diamonds the corresponding η multiplicities. The HADES data are shown as stars in red for π and in blue for η

14   Comparison with Model Calculations

The results are compared to various model calculations. First they are compared to the statistical hadronization model, implemented in the THERMUS code [WCH09] which uses the mixed canonical ensemble, where strangeness is

exactly conserved while all other quantum numbers are calculated grand canonically. Second, a comparison is performed to the UrQMD transport code [B+98].

14.1   Comparison with Statistical Hadronization Model

The fit for statistical hadronization model was performed on 0-20% most central events. Therefore, the η yield is extrapolated to the corresponding centrality class: $\text{Mult}^{\eta}_{b_{max}<20\%} = 0.192 \pm 0.056$. All particle yields obtained in the $^{197}\text{Au}+^{197}\text{Au}$ measurement campaign were fitted simultaneously. The model predicts that a chemical freeze-out occurs at a temperature of $\text{T}_{chem} = (69 \pm 1)$ MeV and at the baryochemical potential of $\mu_B = (785 \pm 21)$ MeV. The strangeness correlation radius is $\text{R}_c = (2.5 \pm 0.5)$ fm, which is about half the total radius $\text{R}_v = (5.4 \pm 0.7)$ fm of the whole fireball, while the χ^2/NDF quality criteria of the fit equals to 1.6. Even though the fit agrees well with the measured yields, the multiplicity of the η meson is underestimated by factor of 2.5 ± 1.5. Besides the η also the K^+ and the ϕ yields [Sch16] seems to deviate stronger from the measured multiplicities. Yet all in all the fit provides a good description of the data and will be further scrutinized in the future.
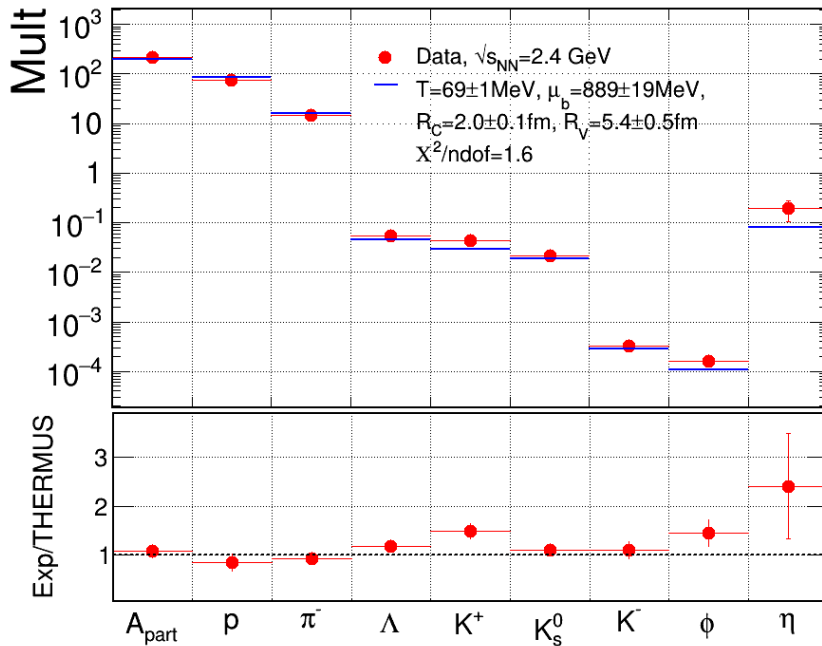

Figure 14.1: SHM comparison for $^{197}\text{Au}+^{197}\text{Au}$ at 1.23 GeV/u. Upper plot shows the measured yields of hadrons at freeze-out in $^{197}\text{Au}+^{197}\text{Au}$ reactions (filled red circles) and the corresponding THERMUS fit values (blue bars) as well as the obtained fit parameters. The lower plot shows the ratio of the experimental to the statistical hadronization model values.

14.2 Comparison with UrQMD

The multiplicities of the mesons are compared to those extracted from UrQMD transport model simulations. Within errors, the π^0 multiplicity agrees (see Figure 14.2), but the production of η mesons seems to be underestimated by the model. The production of the η mesons in this model is dominated by the decay of the $N^*(1535)$ resonance [O$^+$14]:

$$N^*(1535) \to N\eta \quad (BR : 42 \pm 10\%) \tag{49}$$

Decays of higher-lying baryonic resonances are not taken into account. The production cross section of $N^*(1535)$ is not very well constrained, this could explain the observed differences in the yield. Since neither the $N^*(1520)$ nor higher-lying N^* resonances have high-precision evidence to decay into $N\eta$, they are not included in the models. However, there is no physical constraint that would not allow such decays. Measurements of the CBELSA/TAPS collaboration show that for example the branching ratio of the $N^*(1650) \to N\eta$ which is assumed to be 14-22 % [O$^+$14] is probability by factor of ≈ 2 underestimated [Har16b, Har] Therefore, further research with, for example, pion and photon beams could provide an important information to constrain model calculations.
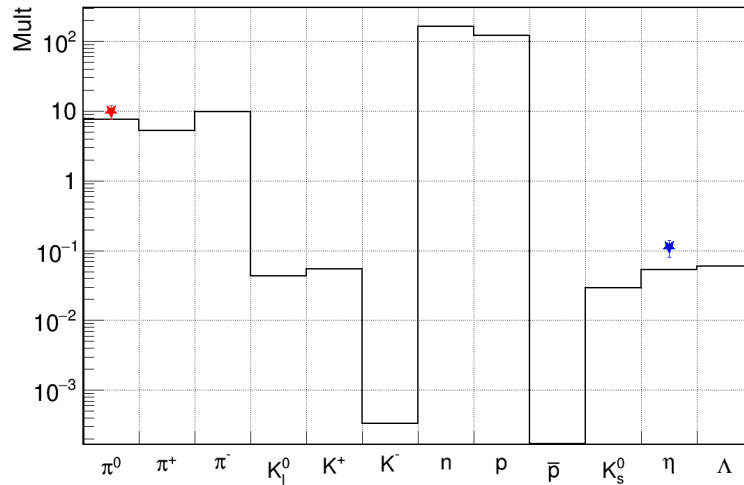

Figure 14.2: UrQMD calculations for particles multiplicities in ^{197}Au$+^{197}$Au collisions at 1.23 GeV/u. The simulations were performed with an maximum impact parameter of b$_{max}$ 11fm. π^0 and η multiplicities obtained in this work are shown as stars.

15 Low Mass Dilepton Excess

As it has been introduced earlier, dileptons are radiated during the whole evolution of a heavy ion collision. Therefore, in order to extract the true medium

radiation the underlying physical background has to be understood. Results from π^0 and η production provide an important constraint in for that underlying background. The dilepton data is obtained by two analyses, one relying on the backtracking algorithm [Sel15, Sel16] and another on using the RICH ring finder [Har16a]. Both analyses use a neural network for the lepton identification. Identified leptons are then combined in unlike sign pairs. The combinatorial background is estimated using so-called same-event technique and event-mixing procedure. After the subtraction of the combinatorial background the signal dilepton spectrum is corrected for efficiency. Even though the backtracking method allows to cover higher invariant masses than the RICH ring finder[24], the results of both methods agree qualitatively and quantitatively. Furthermore, both measurements agree in the π^0 yield with the reference data from elementary p+p and p+n reactions at 1.25 GeV/u [Gal09]. In Figure 15.1 dilepton signals are compared to each other and to a hadronic cocktail, obtained by measurements. The production cross sections for the hadronic cocktail are extracted from reference measurements. The ϕ meson is reconstructed via the K^+K^- decay channel [Sch16]. The ω multiplicity is calculated using the statistical hadronization model predictions (see Section 14.1). The neutral pion multiplicity section is calculated as the average of the charged pions and constrained with the neural pions results of this work. The η meson multiplicity is taken from this work as well. The cock-
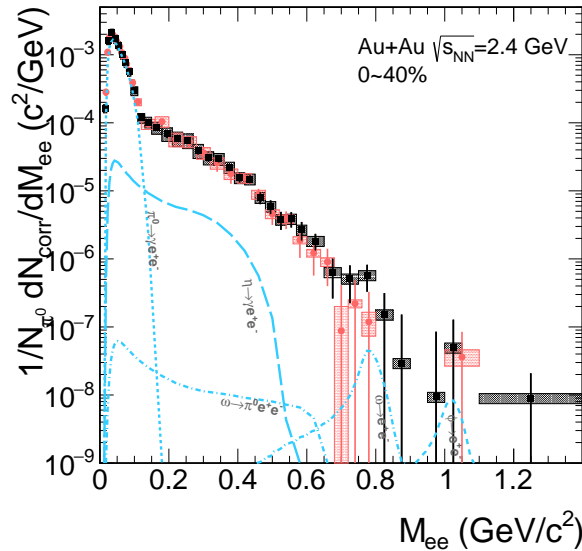

Figure 15.1: ^{197}Au+^{197}Au dilepton invariant mass spectrum together with hadronic cocktail. The measured dileptons are obtained by backtracking algorithm [Sel15, Sel16](black) and the RICH ring finder [Har16a] (red) in 0-40% most central events. The hadronic cocktail is shown in cyan, and the sources are indicated at the lines.

---

[24]due to the higher efficiency and signal to combinatorial background ratio

tail describes the measured data in the π^0 region, but underestimates the yield at higher invariant masses. Since only freeze-out components contribute to the hadronic cocktail, the overshoot can be addressed as radiation, originating from the hot and dense stage of the collision. HADES has measured this radiation in various collision systems at different energies. In Figure 15.2(a) the measured dilepton spectra are compared to those from elementary reactions and normalized to the number of produced π^0. The respective η contribution is subtracted in all cases. Spectra measured in small collision systems (C+C, open squares) are compatible with the elementary reference, independent of the collision energy. In
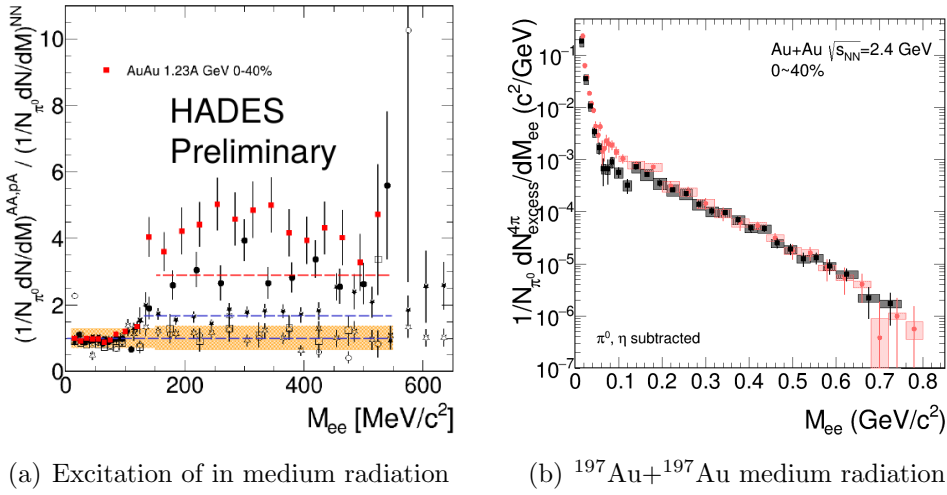

(a) Excitation of in medium radiation   (b) ^{197}Au+^{197}Au medium radiation

Figure 15.2: In medium radiation obtained by HADES measurement campaigns (a) and from ^{197}Au+^{197}Au at 1.23 GeV/u (b)

contrast, the dilepton yield obtained from Ar+KCl collisions shows an overshoot that scales as A_{part}^{α} with α =1.3. The dilepton production in the ^{197}Au+^{197}Au collision system follows the same trend. In Figure 15.2(b) the dilepton invariant mass spectra are shown after the subtraction of the known cocktail sources. It can be compared to theory predictions, like [EvHWB15] and [GHR$^+$16]. Both models are based on the coarse grain approach: the dilepton production in the excess region is based on a thermal ansatz for the spectral functions of ρ, assuming local thermal equilibrium in small space-time cells. Both models describe the excess yield, which supports the conjecture that the radiation originates from the hot and dense stage of the collision. The excess yield scales with $A_{part}^{1.3}$, which points to longer lifetimes of the fireball in more central collisions. The inverse slope parameter T_{slope} of the excess yield seems to rise towards more central collisions while T_{slope} from π^0 seems to stay constant, indicating a sensitivity to the temperature of the medium. After the appropriate estimation of the systematic uncertainties the obtained dilepton yield will lead to a further understanding of hot and dense baryonic matter formed in the SIS18 energy regime.

16   Perspectives with Pion Beams

After the detailed understanding of the ^{197}Au+^{197}Au measurement campaign, the HADES collaboration continues measuring elementary and heavy-ion and pion beam reactions. The heavy-ion data will be used to further understand the systematics of the measured radiation from the hot and dense stage and precisely describe its properties and origin. The π-beam campaigns will help in that context, to better understand the resonance production mechanism, their electromagnetic transition form factors and deliver needed constraints for model calculations. In the following text the raw spectra from π induced reaction as well as upgrade programs in the near and far future will be discussed. In the year 2014, the HADES measured reaction of a pion beam on various targets. The measurement of π^- on polyethylene and carbon targets are used to extract the electromagnetic transition form factor of N*(1520)$\rightarrow \gamma$*N. The obtained dilepton yield is shown in Figure 16.1(a) together with the hadronic cocktail. The cross sections used for the hadronic cocktail are not known precisely enough. Therefore, the reconstruction of π^0 and η using the conversion method is performed. Since the collision environment has much less tracks compared to those in ^{197}Au+^{197}Au the used identification criteria can be much more loose. Figure 16.1(b) shows the four-lepton invariant mass spectrum, obtained using $\alpha_1 < 50$ ° and $\alpha_2 < 100$ ° as topological selection. The meson peaks clearly visible on top of a practically background free region. They are fitted with a Breit-Wigner distribution. Since the leptons are not corrected for energy loss, the peak positions are shifted towards lower invariant masses. The integration in $\pm 2\sigma$ window around peak region gives N$_{\pi^0}$ = 285 ± 17 and N$_\eta$ = 38 ± 6, which will be corrected for conversion probability and efficiency and used to further constrain the hadronic cocktail.

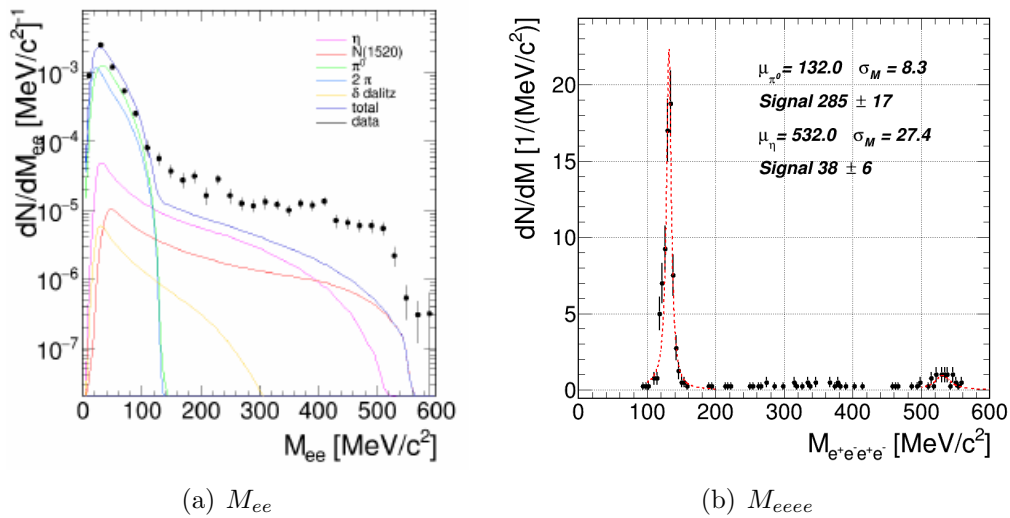(a) M_{ee} (b) M_{eeee}

Figure 16.1: Results from π^+ beam measurements. Left: invariant mass distribution of e^+ee^- pairs, after subtraction of combinatorial background. Right: four-lepton invariant mass distribution.

16.1   Future HADES electromagnetic calorimeter

The dominant correction factor in the present analysis method used in this work is the conversion probability. An increased conversion probability would lead to a higher yield and therefore smaller statistical uncertainties. This could be achieved using, in addition to the segmented target, a thick material block. Furthermore, an increased conversion probability in the target region will lead to much more precise corrections since the conversions on the detector material could be neglected. Using parameters of the ^{197}Au$+^{197}$Au beam time, and a conversion probability of 5% for π^0 and 10% of η, Equation 28 will lead to a measured count rate of $5.38 \cdot 10^{-4}$ π^0/event and $7.66 \cdot 10^{-5}$ η/event. Using these rates, about 10^6 events are needed to obtain the same yield as with the segmented target. This corresponds to about 1% of the currently available statistics. Further investigation for the upcoming heavy-ion campaigns need to be done. Nevertheless, using a thick target other analyses will be affected due to multiple scattering in the material.

Photons can be reconstructed more efficiently using an electromagnetic calorimeter. The installation of an electromagnetic calorimeter ECAL, shown in Figure 16.2, to identify γs directly, is planned in the year 2087. The design of the ECAL is given by the HADES geometry, which means six separate sectors covering almost full azimuthal angle and polar angle 16° to 45°. The size of the modules is fixed since they are loaned from the OPAL collaboration from the former endcap of the detector [A$^+$91]. Details of the calorimeter can be found in [C$^+$11]. The basic physical properties of the calorimeter depend on the type of the lead glass and the geometry. OPAL achieved, using an intrinsic energy resolution of ΔE/E $\approx$ 5% and a pion rejection of $\approx 10^{-3}$, an electron identification efficiency of 80 - 90%. Using this, the acceptance for the π^0 will increase dramatically, since the low-momentum part of the spectrum can be reconstructed. Assuming an acceptance of 80%, a yield similar to the one from the ^{197}Au$+^{197}$Au measurement campaign would be achieved in about 10000 events, without distortion of the dilepton signal due to additional material in the target region. The only disadvantage is the energy resolution of the ECAL, which is ΔE/E $\approx$ 5%. This would lead to much broader reconstructed meson peaks.
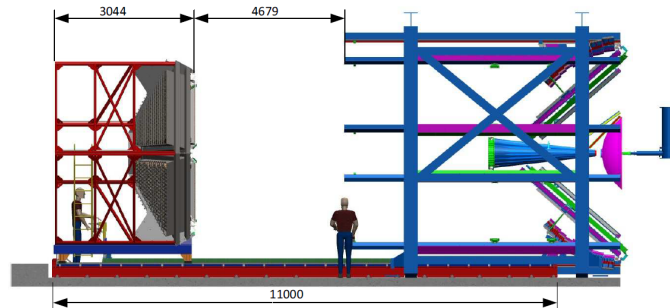

Figure 16.2: Design study of the HADES electromagnetic calorimeter

16.2   The FAIR facility

In the next years the FAIR(Facility for Anti-proton and Ion Research) complex will be built. Close to the current SIS18 accelerator SIS100 will be built. The planned accelerator complex is shown in Figure 16.3 together with the existing GSI accelerators. The SIS18 accelerator will be used as injector for the the SIS 100. At the SIS100 beam energies up to 8 GeV/u (for ^{197}Au beams) and 30 GeV proton beams will be available. Accelerated stripped heavy-ions will be available for experiments using slow extraction and maximum energy. The SIS100 ring will serve a complex system of further rings into which the beams are sent, and then de-accelerated, stored and refined for specific experiments. Four research pillars will define the research done at the FAIR facilities [SSS15] APPA (Atomic, Plasma Physics and Applications), NUSTAR (Nuclear Structure, Astrophysics and Reactions), and Physics with High Energy Antiprotons PANDA and Nuclear Matter Physics. The HADES detector will move from its current position to the so-called CBM cave and will share a beam line with the CBM experiment, and together form the Compressed Baryonic Matter pillar. Both experiments will measure complimentary systems, while HADES will focus on the lower energies up to 3.5 GeV/u (^{107}Ag+^{107}Ag). With a detailed program of heavy-ion and elementary reactions HADES will contribute further to the understanding of the hot and dense matter created in low energy heavy-ion collisions, using the capability to detect various particle species at the same time. Together with the results of experiments at other energies, systematic studies will allow to conclude about deconfinement and the restoration of chiral symmetry.
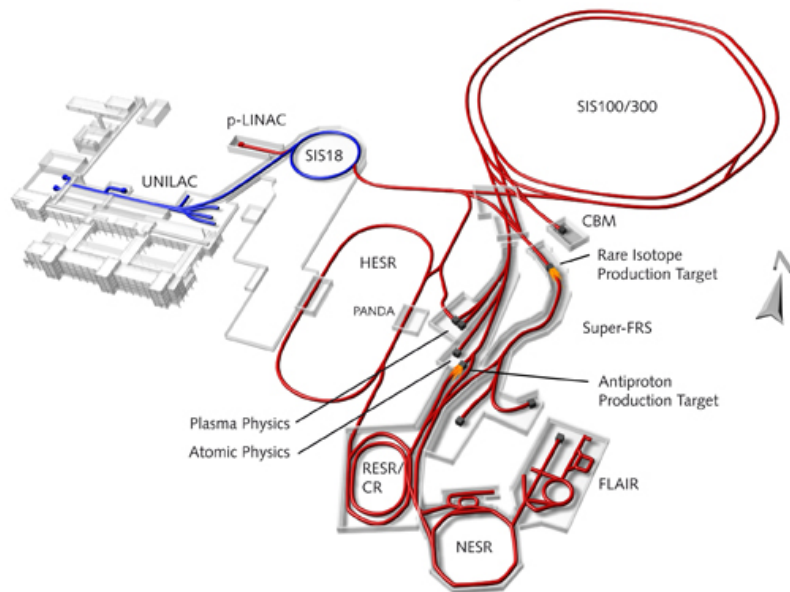

Figure 16.3: FAIR accelerator complex. The existing beam lines are shown in blue and new ones in red.

Zusammenfassung

In dieser Arbeit wurde die Produktionsrate von neutralen Mesonen mittels elektromagnetischer Konversionsmethode bestimmt. Hierbei wurde sich auf das neutrale Pion (π^0) sowie das η-Meson konzentriert. Beide Teilchen tragen mit ihrem Dalitz Zerfall zum Dileptonen Spektrum bei. Da die Lebenszeit dieser beiden Mesonen signifikant höher liegt als die des entstanden Feuerballs, tragen sie keine Informationen über die Hochdichtephase der Kollision, und müssen von Dileptonen Spektrum abgezogen werden.

1 Einleitung

Die Freiheitsgrade von Kernmaterie hängen stark von Temperatur und baryochemischen Potential ab. Bei sehr hohen Temperaturen und sehr niedrigem baryochemischen Potential erwartet man eine *deconfined* Phase, das sogenannte Quark-Gluonen Plasma. Bei niedrigeren Temperaturen und höherem baryochemischen Potential sagen theoretische Modelle noch exotischere Phasen voraus. Beim SIS18 Beschleuniger werden Kerne mit kinetischen Energien von 1 - 2 GeV/u auf stationäre Targets geschossen, um Kernmaterie unter diesen Bedingungen zu vermessen. Eine der aktuellsten Messungen wurde im April 2012 von der HADES Kollaboration abgeschlossen. Das gemessene System war ^{197}Au+^{197}Au bei einer Strahlenergie von 1.23 GeV/u. Im SIS18 Energiebereich werden drei verschiedene Stadien einer Kollision angenommen, die Phase der ersten Kollisionen, die Hochdichtephase und die Ausfrierphase. Direkte Photonen (γ) und Dileptonen (e^+e^-) durchdringen all diese Phasen ohne stark wechselzuwirken. Daher sind Leptonenpaare eine ideale Sonde, um die Eigenschaften der hochdichten Phase der Kollision zu verstehen. Da die Lebensdauer einer Kollision viel kürzer ist als die Auslesezeit der Detektoren, können die verschiedenen Phasen nicht zeitlich unterschieden werden. Es ist daher wichtig die Quellen der Leptonenpaarproduktion aller Phasen zu identifizieren. Messungen eines Referenzspektrums bestehend aus elementaren Reaktionen, p+p und n+p, wurden benutzt um Beiträge der ersten Phase abzuschätzen [A$^+$10c, A$^+$12b, A$^+$12c]. Mesonen mit einer langen Lebensdauer (lang im Vergleich zur Lebensdauer des Feuerballs), wie zum Beispiel das neutrale π^0- und das η-Meson, sind der dominante Beitrag zur invarianten Dileptonenmasse aus der Ausfrierphase. Für die Normierung des invarianten Dileptonenmassenspektrums ist die Messung des π^0 Beitrages entscheidend. Die Messung des Wirkungsquerschnittes des η Mesons ist erforderlich, um die nicht triviale Überhöhung bei niedrigen invarianten Massen ($M_{e^+e^-}$ zwischen 0.15 GeV/c^2 und 0.55 GeV/c^2) zu bestimmen. Diese wurde neben anderen bei DLS [P$^+$97] und HADES [A$^+$11a] am Bevalac/SIS18, CERES [A$^+$05] und NA60 [A$^+$06] am CERN, und STAR [Hua13] und Phenix [A$^+$10a] am RHIC gemessen. Beide Mesonen tragen via ihrer Dalitz Zerfälle (Meson $\rightarrow \gamma e^+e^-$) zum Dileptonenspektrum bei. Durch die Messung des entstandenen

Photons kann der Mesonen Beitrag vollständig rekonstruiert werden. Des Weiteren zerfallen das π^0 und das η Meson dominant in zwei Photonen (Meson $\rightarrow \gamma\gamma$). Durch die Messung von Photonen kann dieser Zerfallskanal ebenfalls studiert werden. HADES besitzt bisher kein elektromagnetisches Kalorimeter, daher ist die Messung von Photonen nur möglich, mithilfe von externer Konversion der Photonen im Detektormaterial.

2   Das HADES Spektrometer

Das High Acceptance DiElectron Spectrometer (HADES) ist am SIS18 (GSI Helmholtzzentrum für Schwerionenforschung, Darmstadt) [A$^+$09c] installiert. Es besteht aus sechs identischen Sektoren, die beinah den vollen azimuthalen Winkel sowie Polarwinkel von 18° bis 85° abdecken. Die Teilchenspurfindung wird mit 4 x 6 Vieldrahtminidriftkammern und einem supraleitenden toroidalen Magneten durchgeführt. Zur Flugzeitmessung werden ein "Time-of-Flight" Detektor und eine "Resistive Plate Chamber" genutzt. Im April 2012 wurde das Kollisionssystem Au+Au mit einer Strahlenergie von E$_{kin}$ = 1.23 GeV/u gemessen. Der gewählte Trigger auf eine Trefferanzahl im Time-of-Flight Detektor ToF_{Mult} >= 20 sowie weitere Ereignisselektionen sorgten für eine Messungen der 40% zentralsten Stöße und einem zugehören Stoßparameter von b$_{max}$ ≈ 10 fm. Die Wahrscheinlichkeit einer externen Konversion wird mithilfe des Simulationspaketes GEANT bestimmt. In dieser Arbeit wird die Konversionswahrscheinlichkeit definiert als die Wahrscheinlichkeit, das ein rekonstruierbares Leptonenpaar, welches aus einem konvertierten Photon stammt, erzeugt wird. Der differentielle Wirkungsquerschnitt dieses Prozesses hängt von der Ordnungszahl Z des Materials ab, in dem die Wechselwirkung auftritt. Für ein zusammengesetztes Material, in dem die Wechselwirkung in einem Element i zufällig auftreten kann gilt die Wahrscheinlichkeit:

$$p_{conv}(Z_i, E_\gamma) = \frac{n_{ati}\sigma(Z_i, E_\gamma)}{\sum_i [n_{ati} \cdot \sigma_i(E_\gamma)]},$$

$$(50)$$

wobei Z_i die Ordnungszahl, n_{ati} die Anzahl der Atome des Volumenelements i^{th} und E_γ die Energie des Photons ist. Tabelle 10.2 zeigt die Konversionswahrscheinlichkeit für die Hauptkomponenten im inneren Teil des Spektrometers. Systematische Fehler aufgrund von Unsicherheiten im Materialbudget werden ebenfalls aufgezählt.

3   Rekonstruktion neutraler Mesonen

Verschiedene Messgrößen werden vom HADES Detektor zur Leptonen Identifikation genutzt. Beispiele sind RICH Ring Eigenschaften, Teilchen Geschwindigkeiten, Energieverlust in ToF Detektor und den MDC Kammern. Bei Geschwindigkeiten

von $\beta \approx 1$ und Impulsen von weniger als 500 MeV/c liegen Leptonenkandidaten. Leptonenpaare welche aus Konversion stammen können mithilfe ihrer kleinen Öffnungswinkel und des niedrigen Impulses charakterisiert werden. Paare, welche diese kleinen Öffnungswinkel haben, lösen im RICH Detektor nur einen einzigen Ring aus. Des Weiteren könnten Konversionen, welche im Radiator Gas und im Spiegel auftreten, nicht berücksichtigt werden, wenn ein Ring im RICH Detektor verlangt wird. Aus diesem Grund werden Leptonen nur mittels ihrer Geschwindigkeit als Funktion des Impulses mal der Ladung identifiziert. Identifizierte Leptonen werden zu ungleich geladene Paaren kombiniert. Mindestens zwei dieser Paare müssen pro Event gefunden werden. Für die Identifikation neutraler Mesonen werden topologische Schnitte auf die Öffnungswinkel zwischen den Leptonen und den rekonstruierten Paaren (Photonen) angewendet. Für die Identifikation mittels totaler Kornversionsmethode muss mindestens eines der Paare von einem echten Photon stammen. Daher wird verlangt das eines der Paare einen
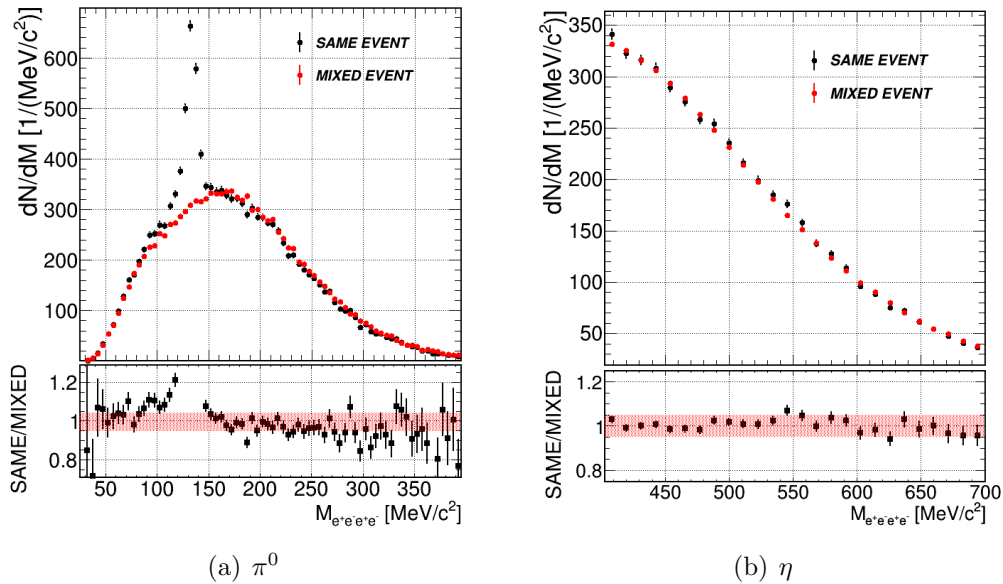

(a) π^0 (b) η

Figure G1: Vier Leptonen invariante Masse (schwarz) nach topologischer Selektion der π^0 (a) und η (b) Mesonen, zusammen mit dem unkorrelierten Untergrund (rot). Die unteren Bilder zeigen das Verhältnis des Signals zum Untergrund

Öffnungswinkel von $\alpha_1 < 4.5°$ hat. Da das Zweite Paar auch aus dem Zerfall eines virtuellen Photon innerhalb eines Dalitz Zerfalls stammen kann, ist der gewählte Schnitt weniger stark: $\alpha_2 < 10°$. Werden in einer Kollision vier Leptonen rekonstruiert, die diesen Kriterien genügen werden sie zu Vier-Leptonen Multiplets kombiniert. Bild G1 zeigt die invariante Masse des Vier-Leptonen Multiplets, für den π^0 und η Massenbereich zusammen mit dem kombinatorischen Untergrund (rot), der über die Kombination von Photonen Kandidaten aus unterschiedlichen Kollision bestimmt werden kann. Der so ermittelte Untergrund beschreibt das Spektrum außerhalb der Signalregion innerhalb einer 5%igen Unsicherheit. Nach

Abzug des Untergrunds wird das resultierende Spektrum mit einer Breit-Wigner Verteilung angepasst und die Anzahl der Mesonen wird in einem 2σ Bereich integriert. Es ergeben sich folgende Anzahlen $N_{\pi^0} = 4606 \pm 130_{stat} + 5 - 6_{sys}$ und $N_\eta = 424 \pm 133_{stat} + 3 - 1_{sys}$, wobei die systematische Unsicherheit mithilfe der Variation der Normierung des Untergrundes abgeschätzt wird. Die so gewonnen Zählraten werden auf Detektor Effekte und Konversionswahrscheinlichkeit korrigiert und in der so genannten Boltzmann Darstellung analysiert um den inversen Steigungsparameter sowie die Ausbeute der Mesonen als Funktion der Rapidität zu erhalten. Durch Extrapolation in den gesammten Phasenraum lassen sich die folgenden Teilchenmultiplizitäten ermitteln: $Mult_{\pi^0}^{4\pi} = 9.70 \pm 0.27_{stat} \pm 1.8_{sys} \pm 1.3_{extrap}$ und $Mult_\eta^{4\pi} = 0.107 \pm 0.005_{stat} \pm 0.028_{sys} \pm 0.007_{extrap}$ sowie ein Inverser Steigungsparameter des π^0 Mesons von 84.7 MeV $\pm 1.8_{stat} \pm 6,1_{sys}$ MeV. Die systematischen Unsicherheiten werden hierbei mithilfe von Variation der Korrektur sowie der Modellannahmen für die gewählte Akzeptanz bestimmt.
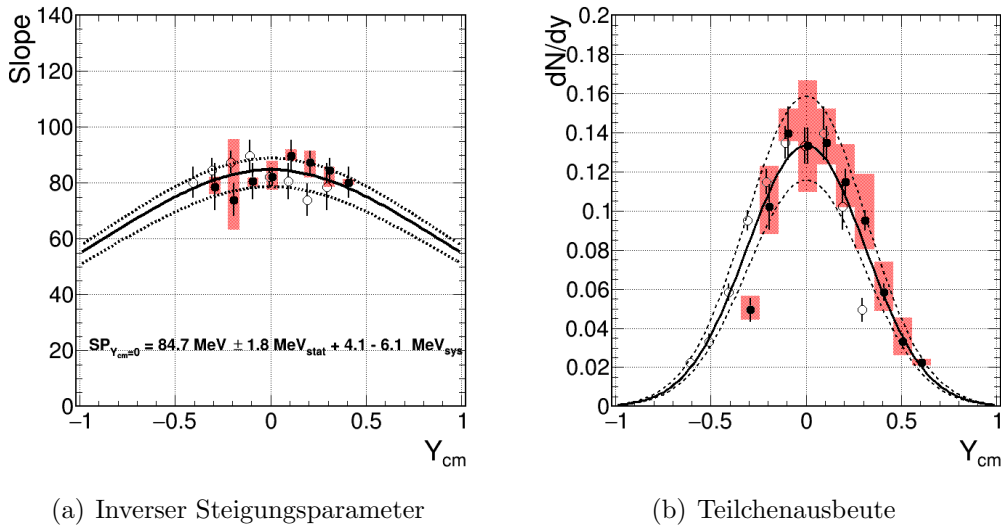

(a) Inverser Steigungsparameter   (b) Teilchenausbeute

Figure G2: Inverser Steigungsparameter und Teilchenausbeute als Funktion der Rapidität für neutraler Pionen

4   Ergebnisse

Die gewonnen Ergebnisse können mithilfe unabhängiger Messungen verifiziert und mit theoretischen Modellen verglichen werden. Zunächst wird die Produktionsrate der neutraler Pionen mit denen der geladene Pionen verglichen. Aus Isospinerhaltung flogt das der Mittelwert der Produktionsraten der geladenen Pionen dem der Neutralen entsprechen muss. Die Anzahl von π^+ liegt bei 12.0 ± 0.71 und π^- 6.7 ± 0.61 pro Kollisionsevent. Der errechnete Mittelwert ist 9.35 ± 1.32 und innerhalb der Unsicherheiten der Anzahl der neutralen Pionen kompatibel. Um einen Vergleich mit bisher gemessenen Kollisionssystemen zu ermöglichen werden die gemessenen Teilchenmultipliztäten zu *minimum bias* Kollisionen extrapoliert.
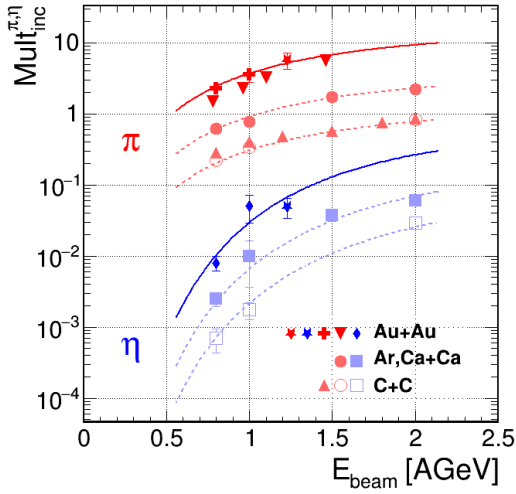
Figure G3: Mesonenmultiplizität

Bild G3 zeigt die gemessenen Multiplizitäten (η: blauer Stern, π^0 roter Stern) zusammen mit Messungen der TAPS und KaoS Kollaborationen [ea97, AHMS03, W+98, BPS+94, A+97, SP+94, M+97, M+99]. Die gemessenen Werte sind in guter Übereinstimmung mit den Daten und der Extrapolation. Im Bild G4 ist das gemessene Dileptonen Spektrum, zusammen mit dem hadronischen Untergrund gezeigt. Die Zusammensetzung des Untergrundes wird durch die gemessenen Teilchenmultiplizitäten bestimmt. Das ϕ Meson wurde in [Sch16] bestimmt, und π^0 und η-Mesonen stammen aus dieser Arbeit.

Mithilfe des statistischen Modells konnte die Anzahl ω-Mesonen bestimmt werden. Alle gezeigten Komponenten haben eine Lebensdauer, die länger als die des Feuerballs ist und tragen daher nur die Informationen der Ausfrierphase. Nach dem Abzug dieses Cocktail vom gemessenen Spektrum (Bild 4.4(b)) wird resultierende Spektrum mit theoretischen Modellen [EvHWB15] und [GHR+16] verglichen. Die hier verwendeten Modelle beschreiben die Dileptonenproduktion in einem "coarse grain" Ansatz, welcher die Überhöhung in diesem Bereich unter Annahme von lokalem thermischem Gleichgewicht beschreibt. Nach der Bestimmung der systematischen Unsicherheiten wird die gemessene Überhöhung zusammen mit dem gemessen Untergrund zum besseren Verständnis der hochdichten Kernmaterie im SIS18 Energiereich beitragen.
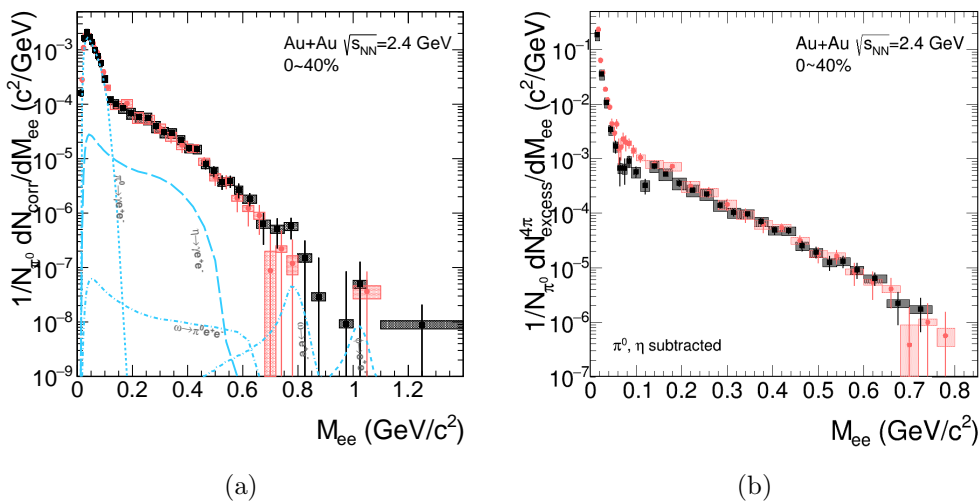

(a)

(b)

Figure G4: invariante Dileptonenmassenspektrum mit (a) Hadronischem Cocktail (b) nach Abzug des Cocktails.

A   Code for Building Conversion Pairs

```
for(UInt_t lep1 = 0; lep1 < lep.size(); lep1 ++)
{
    for(UInt_t lep2 = lep1+1; lep2 < lep.size(); lep2 ++)
    {
        if(lep[lep1]==lep[lep2]) continue;
        for(UInt_t lep3 = lep2+1; lep3 < lep.size(); lep3 ++)
        {
            if(lep[lep1]==lep[lep3]) continue;
            if(lep[lep2]==lep[lep3]) continue;
            for(UInt_t lep4 = lep3+1; lep4 < lep.size(); lep4 ++)
            {
                if(lep[lep1]==lep[lep4]) continue;
                if(lep[lep2]==lep[lep4]) continue;
                if(lep[lep3]==lep[lep4]) continue;
                //-----------------------------------
                HParticlePair* pair_a = new HParticlePair;
                HParticlePair* pair_b = new HParticlePair;
                pair_a->setPair(lep_new_1,2,lep_new_2,3,51,0,vertex);
                pair_b->setPair(lep_new_3,2,lep_new_4,3,51,0,vertex);

                HParticlePair* pair_c = new HParticlePair;
                HParticlePair* pair_d = new HParticlePair;
                pair_c->setPair(lep_new_1,2,lep_new_3,3,51,0,vertex);
                pair_d->setPair(lep_new_2,2,lep_new_4,3,51,0,vertex);

                HParticlePair* pair_e = new HParticlePair;
                HParticlePair* pair_f = new HParticlePair;
                pair_e->setPair(lep_new_1,2,lep_new_4,3,51,0,vertex);
                pair_f->setPair(lep_new_2,2,lep_new_3,3,51,0,vertex);
                //-----------------------------------
                // 1st Pair
                if(((pair_a->getOpeningAngle() < oA_sm)&& (pair_b->getOpeningAngle() < oA_la))  ||
                    ((pair_a->getOpeningAngle() < oA_la )&& (pair_b->getOpeningAngle() < oA_sm))
                    ) {
                    quads_top.push_back(quad_1);
                    //Mixing
                    if(lepCase(quad_1)==0  ){
                        if(pair_a->getOpeningAngle() < oA_sm && pair_b->getOpeningAngle() < oA_la){
                            pairs_close.push_back(pair_a); pairs_open.push_back(pair_b);
                        }
                        else{pairs_open.push_back(pair_a); pairs_close.push_back(pair_b);}
                    } continue;
                }
                // 2nd Pair
                if(((pair_c->getOpeningAngle() < oA_sm)&& (pair_d->getOpeningAngle() < oA_la))  ||
                    ((pair_c->getOpeningAngle() < oA_la )&& (pair_d->getOpeningAngle() < oA_sm))
                    ) {
                    quads_top.push_back(quad_2);
                    if(lepCase(quad_2)==0){
                        if(pair_c->getOpeningAngle() < oA_sm && pair_d->getOpeningAngle() < oA_la){
                            pairs_close.push_back(pair_c);  pairs_open.push_back(pair_d);
                        }
                        else{ pairs_open.push_back(pair_c); pairs_close.push_back(pair_d);}
                    } continue;
                }
                //3rd Pair
                if(((pair_e->getOpeningAngle() < oA_sm)&& (pair_f->getOpeningAngle() < oA_la))  ||
                    ((pair_e->getOpeningAngle() < oA_la )&& (pair_f->getOpeningAngle() < oA_sm))
                    ) {
                    quads_top.push_back(quad_3);
                    if(lepCase(quad_3)==0  ){
                        if(pair_e->getOpeningAngle() < oA_sm && pair_f->getOpeningAngle() < oA_la){
                            pairs_close.push_back(pair_e);  pairs_open.push_back(pair_f);
                        }
                        else{ pairs_open.push_back(pair_e);  pairs_close.push_back(pair_f);  }
                    } continue;
                }
                //-----------------------------------
            }
        }
    }
}
```

Figure A 1: Main part of the double pair analysis.

B   Probability of Uncorrelated Sources

Knowing from Section 11.1 the amount of neutral pions per events is approximately 10. The probability for a decay into two photons is nearly 100%. The conversion probability for one photons (See Section 10.1) is p 0.0078. With assuming a binomial process:

$$1 - (B(k \mid p, n) = \binom{n}{k} p^k (1-p)^{n-k}) - p^2, \tag{51}$$

where n =20,k= 1 it is possible co calculate the possibility that two independent photons convert and contribute to the four lepton invariant mass spectra. The resulting probability is about 85%.

C   Statistical Uncertainties

The four lepton invariant mass spectra M contains the signal S and the background B:

$$M = S + B \tag{52}$$

The extracted signal is:

$$S = M - B = S + B - B \tag{53}$$

The background is estimated with the mixed event method ME, that need to be normalized:

$$B = ME \cdot f \tag{54}$$

The extracted signal is:

$$S = M - ME \cdot f \tag{55}$$

Under the assumption of poissonian errors the statistical error of the signal is:

$$\sigma(S)^2 = M + \sigma^2(f)M^2 + f^2 M \tag{56}$$

With large statistic of the mixed event background the two last terms go to zero and the resulting error is:

$$\sigma(S)^2 = M \tag{57}$$

D   Source Variation for Acceptance

T_1 [MeV]	T_2 [MeV]	T_1/T_2	blast [β]	ϵ_{Acc}
50	80	0.98	0.4	0.088
40	80	0.98	0.4	0.082
60	80	0.98	0.4	0.113
50	70	0.98	0.4	0.081
50	90	0.98	0.4	0.098
50	80	0.98	0.5	0.107
50	80	0.98	0.3	0.074
50	80	0.99	0.4	0.083
50	80	0.97	0.4	0.093

Table A 2: Variation of source for acceptance

T_1 [MeV]	blast [β]	ϵ_{Acc}
50	0.4	0.698
40	0.4	0.759
60	0.4	0.642
50	0.3	0.778
50	0.5	0.583

Table A 3: Variation of source for acceptance

E   Geant Medium Numbers

Used for ^{179}Au+^{179}Au at 1.23 GeV/u.
AIR 1
METHAN 2
ALUMINIUM 3
STEEL 4
STESALITH 5
RICHPHOTDET 6
RICHPADS 7
C4F10 8
CAF2 9
CARBON 10
AIR_100MBAR 11
STEEL_RICH 12
RICHMIRROR 13
CFKSHELL 14

ARBON_RICH 15
KAPTON 16
POLYPROPYLEN 17
POLYPROPYLEN_RICH 18
GOLDTARGET 19
CARBONFIBRE 20
CARBONFIBRE_TARG 21
DUROSTONE 22
DRIFTGAS_MDC_AR_CO 23
CUBE_KATH 24
CUBE_KATH_C4 25
MYLAR_DET 26
CUBETUWI_D1 27
ALU_KATH 29
ALTUWI_D2 30
ALU_KATHC4 31
ALTUWI_D3 32
ALTUWI_D4 33
VAKUUM 34
COIL_STEEL 35
COIL_MIXT 36
COIL_ALU 37
INSULATOR_TOF 38
SCINTILLATOR 39
EPOXY 40
PAD_FIBRE 41
DRIFTGAS_SHOWER 42
TU_CU_BE_WIRES 43
LEAD 44
HELIUM 45
ALUMINIUM_10PERC 46
CONCRETE 47
TROVIDUR 48
COPPER 49
DIAMOND 50
SCINTILLATOR_NOFIELD 51
AIR_ACTIVE 52
GAS_RPC_NOACTIVE 53
GLASS 55

F   Invariant Mass in Phase Space Bins
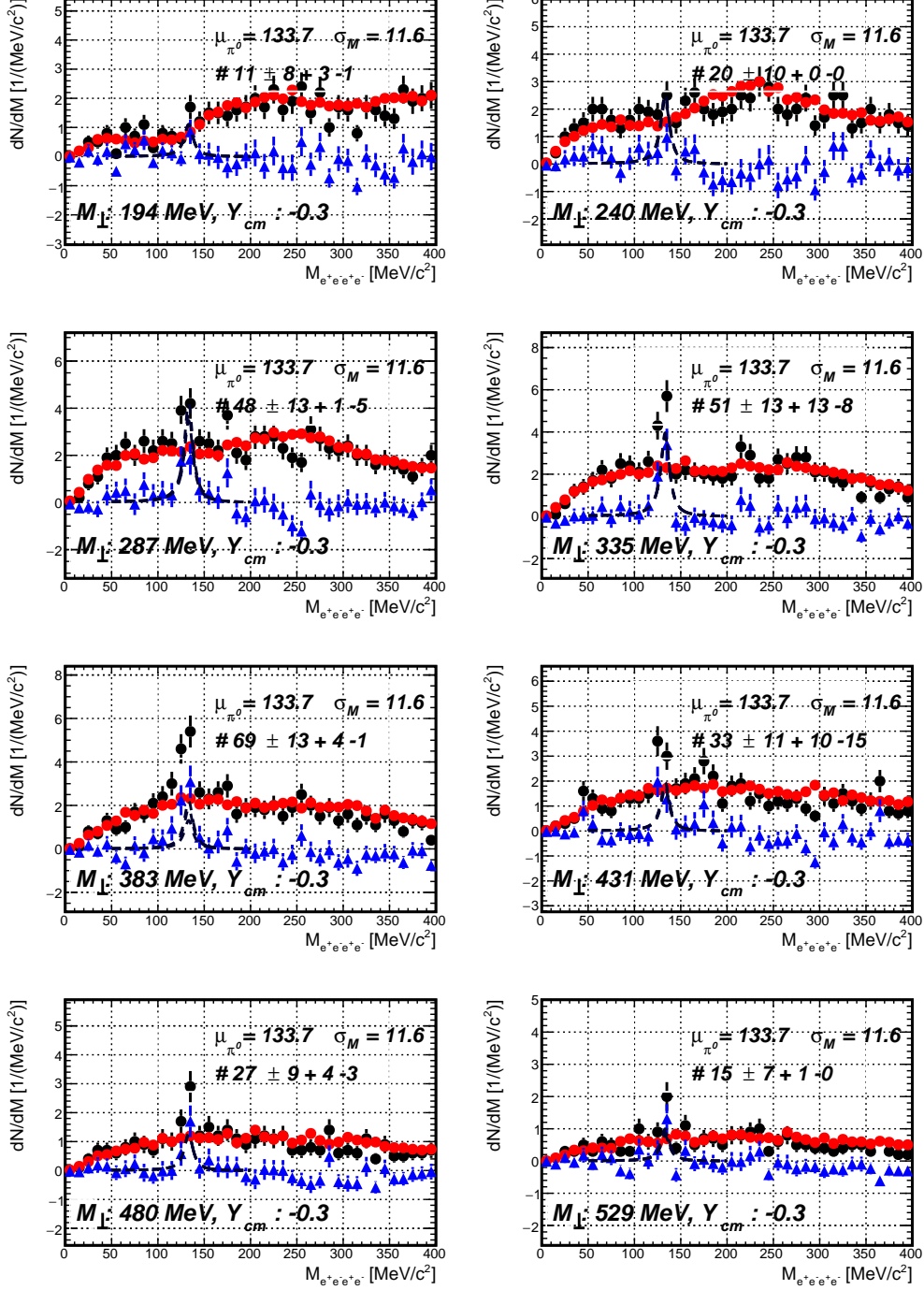
Figure A 1: Phase space dependent four lepton invariant mass spectrum with mixed event background (red).
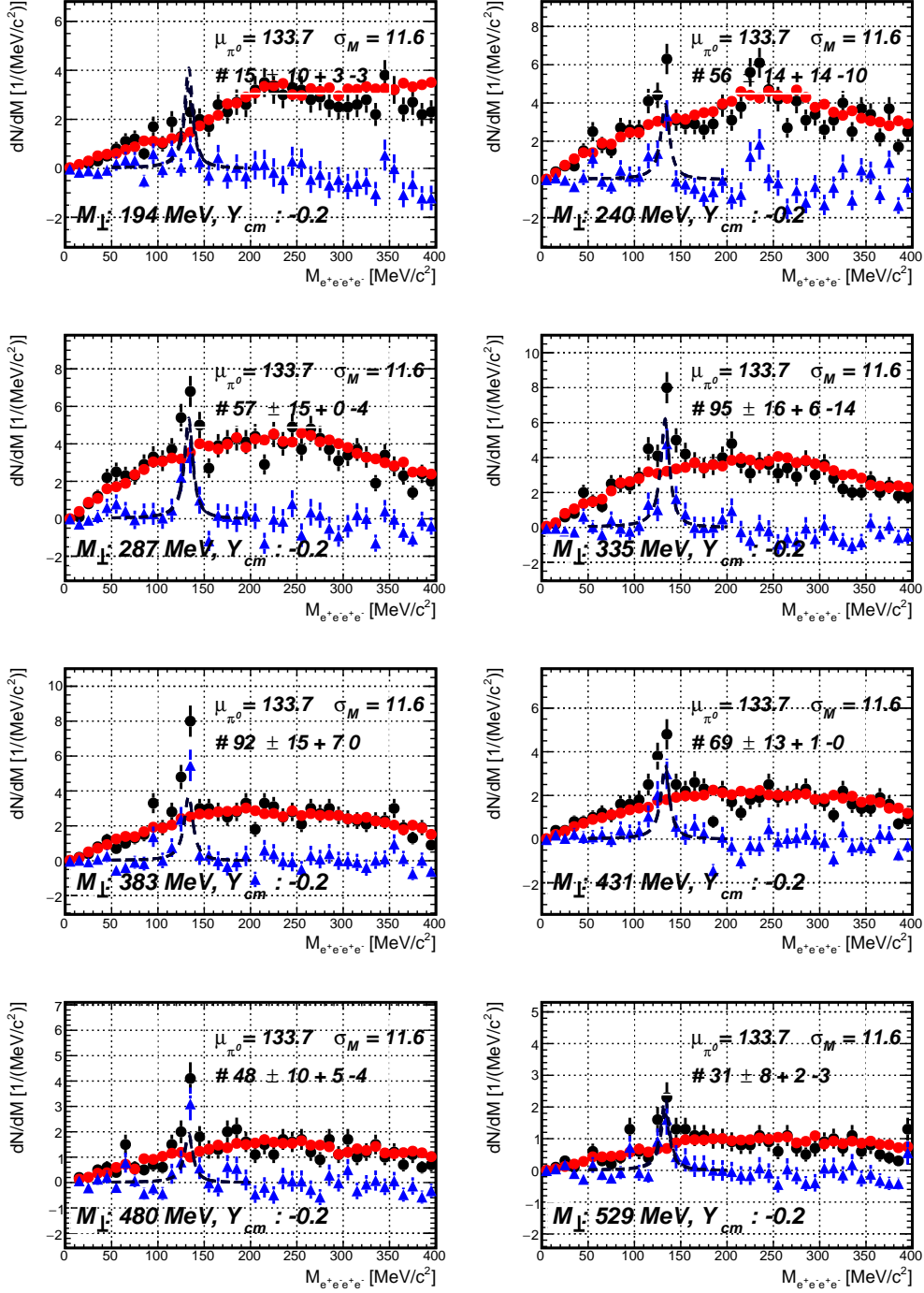
Figure A 2: Phase space dependent four lepton invariant mass spectrum with mixed event background (red).
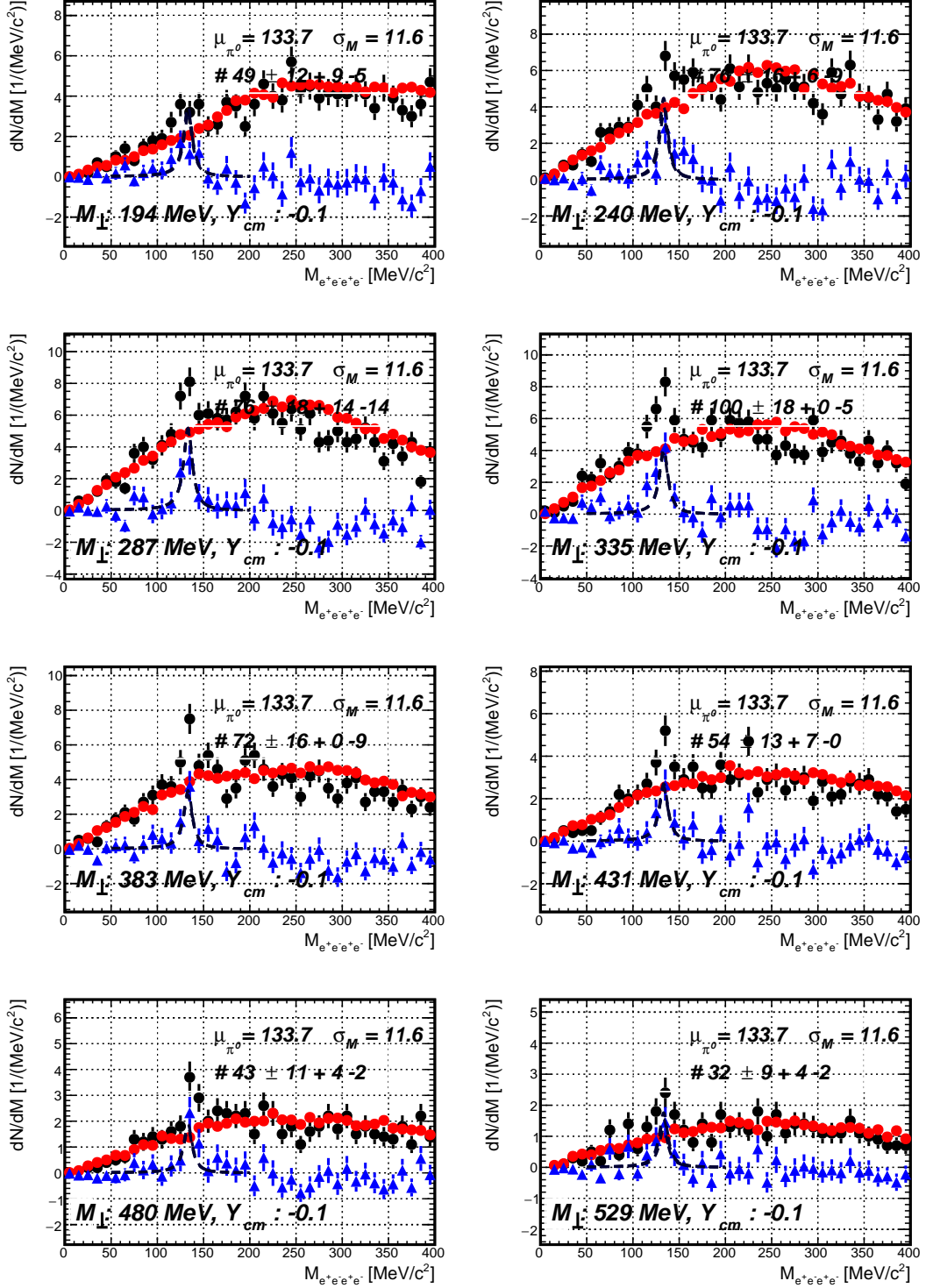
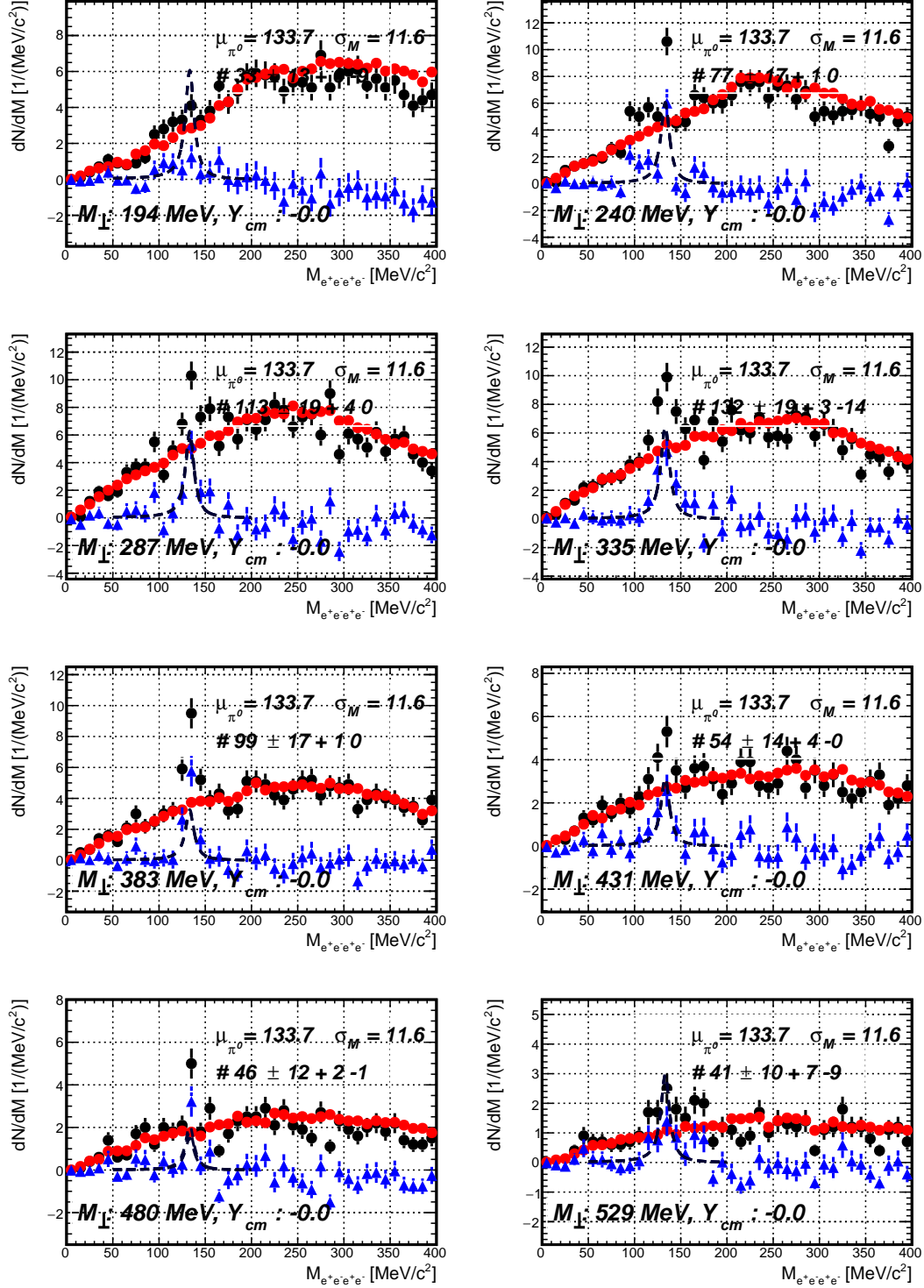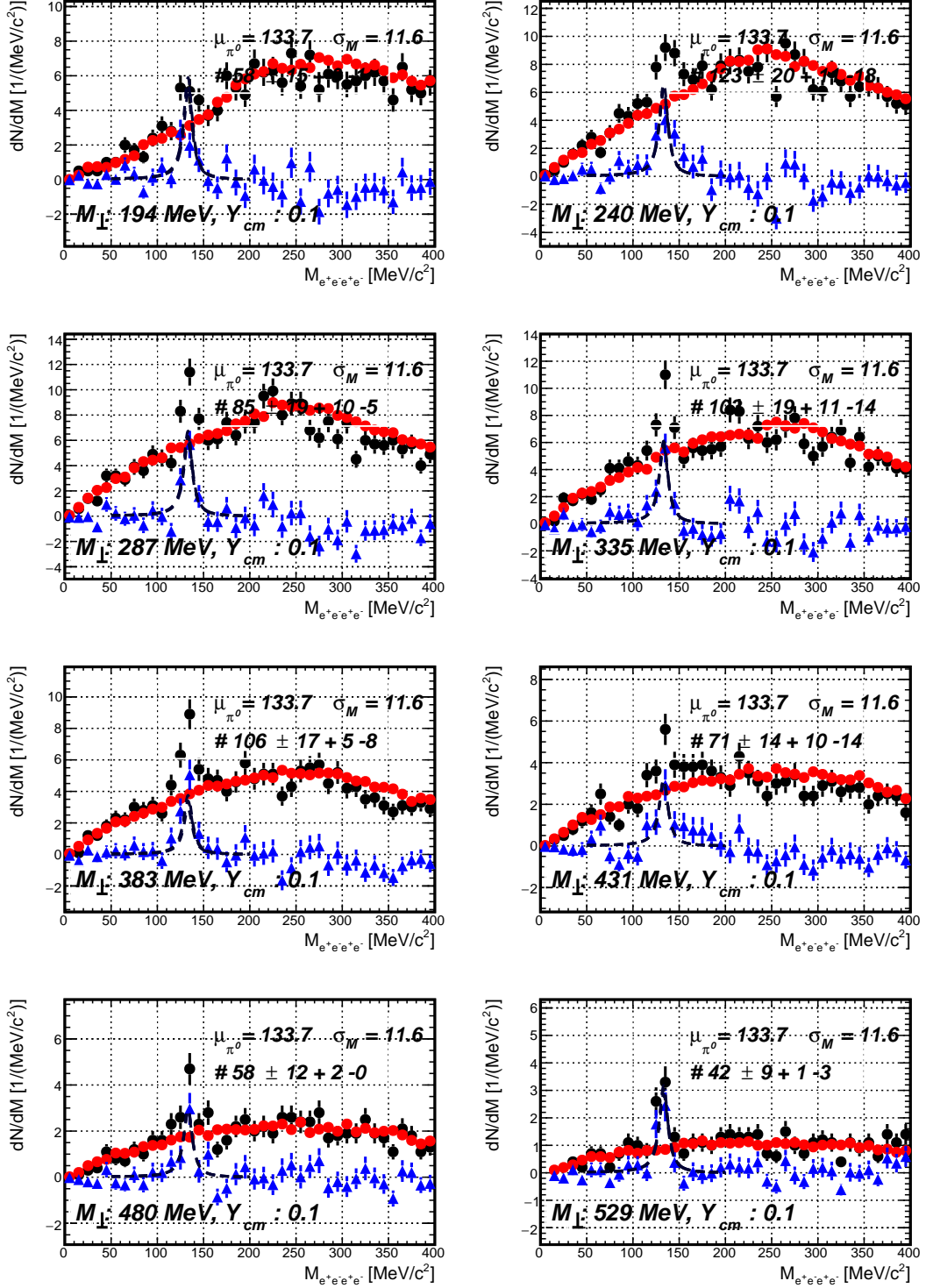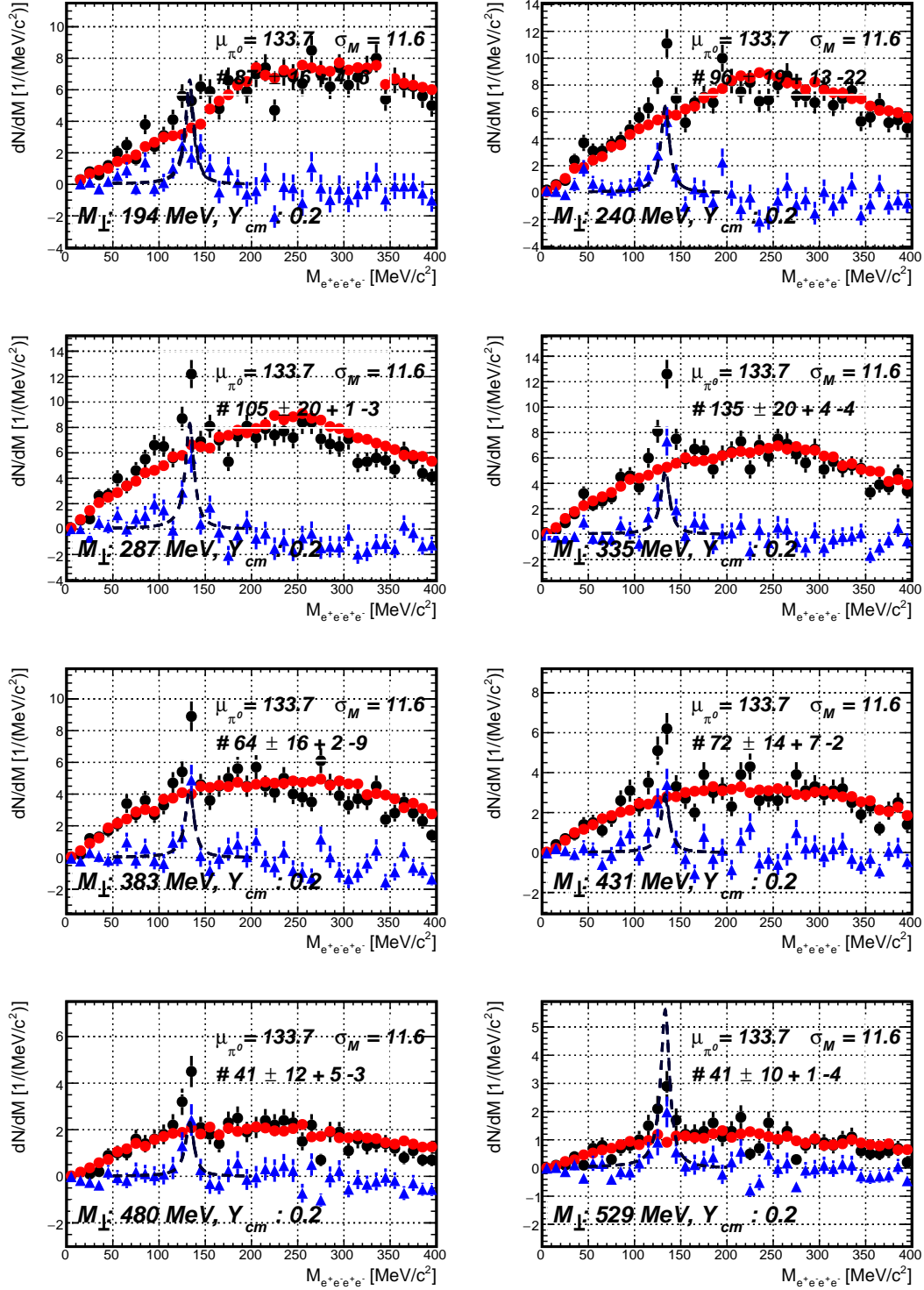Figure A 3: Phase space dependent four lepton invariant mass spectrum with mixed event background (red).

Figure A 4: Phase space dependent four lepton invariant mass spectrum with mixed event background (red).

Figure A 5: Phase space dependent four lepton invariant mass spectrum with mixed event background (red).

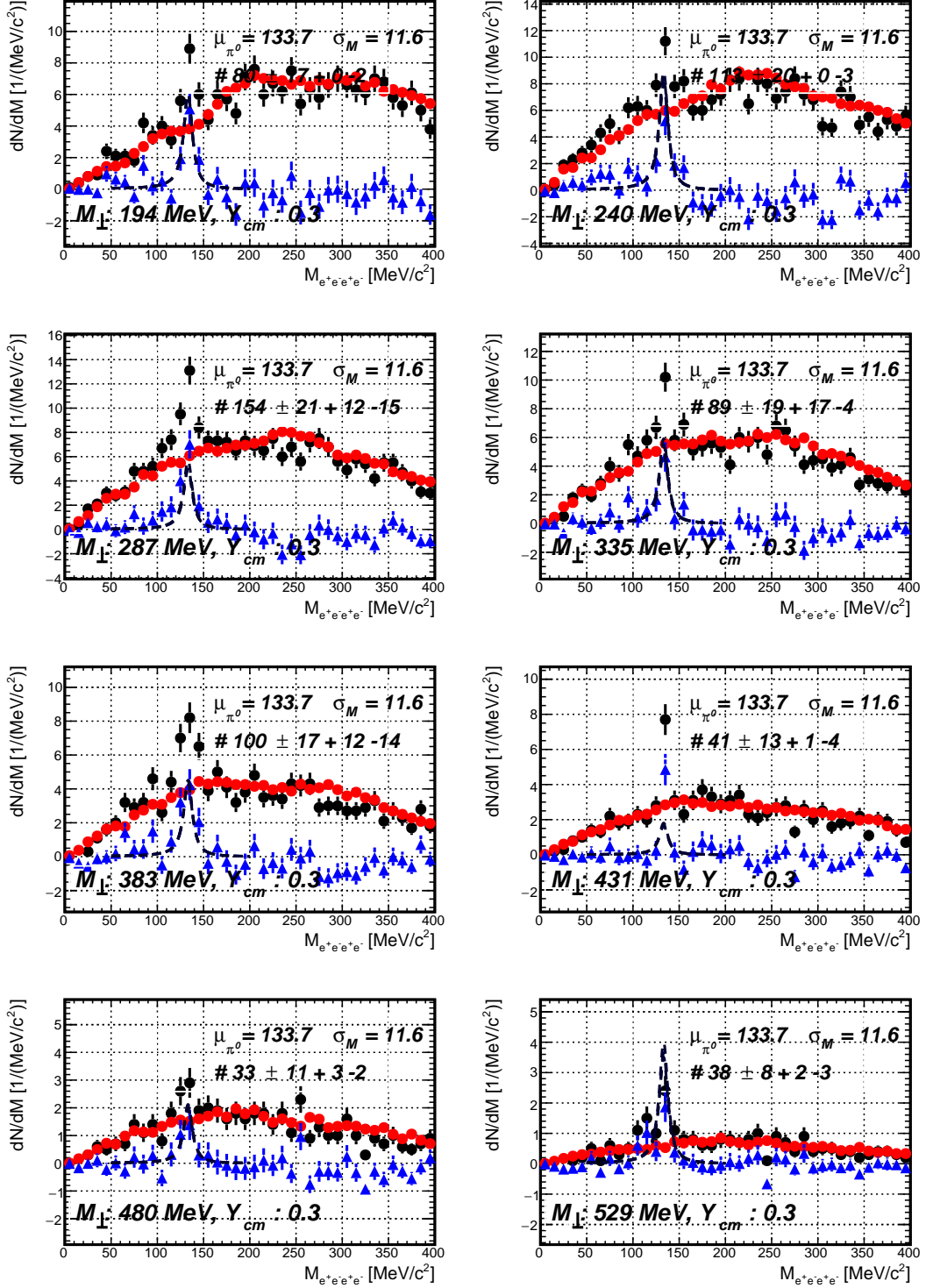Figure A 6: Phase space dependent four lepton invariant mass spectrum with mixed event background (red).

Figure A 7: Phase space dependent four lepton invariant mass spectrum with mixed event background (red).
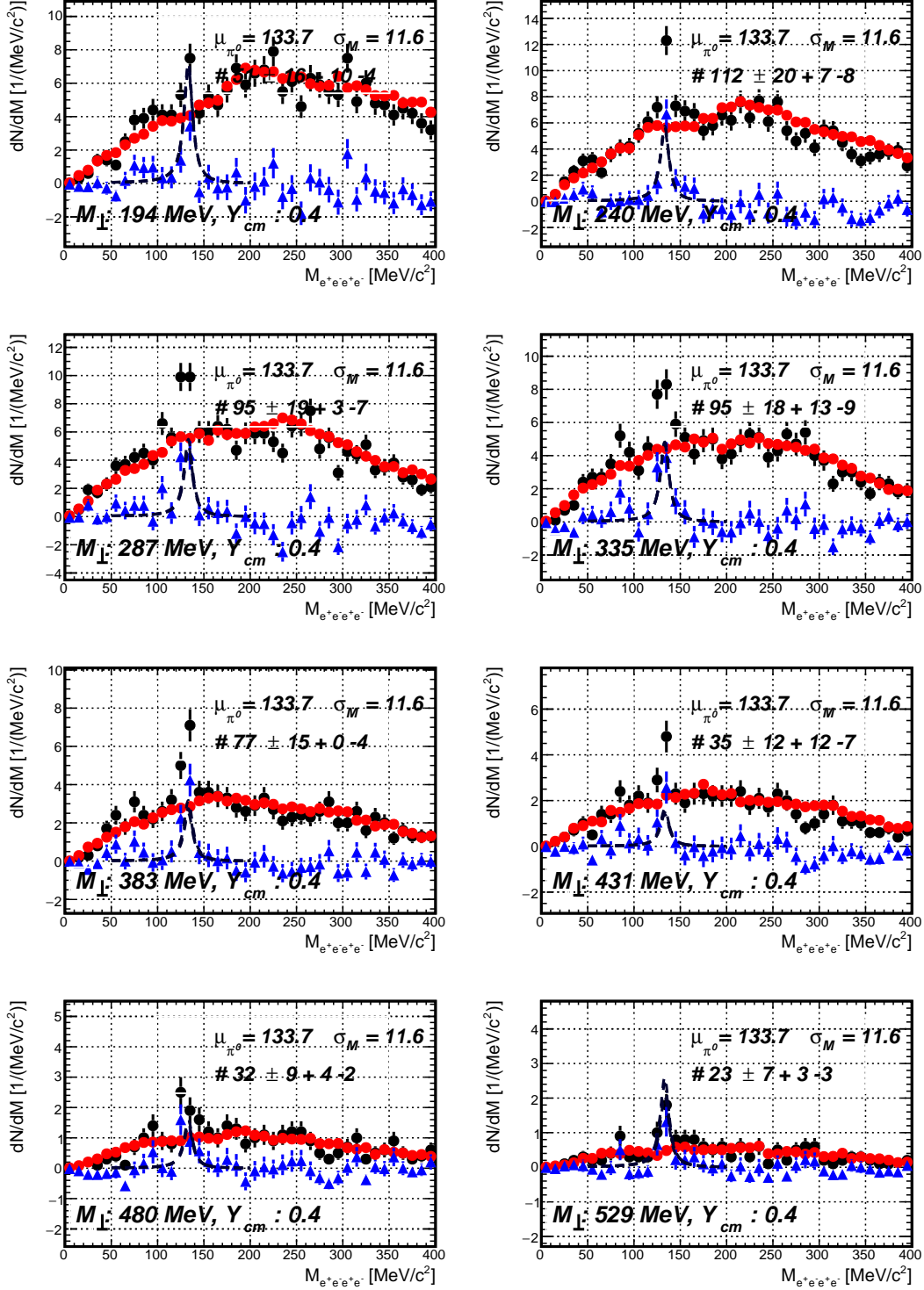
Figure A 8: Phase space dependent four lepton invariant mass spectrum with mixed event background (red).
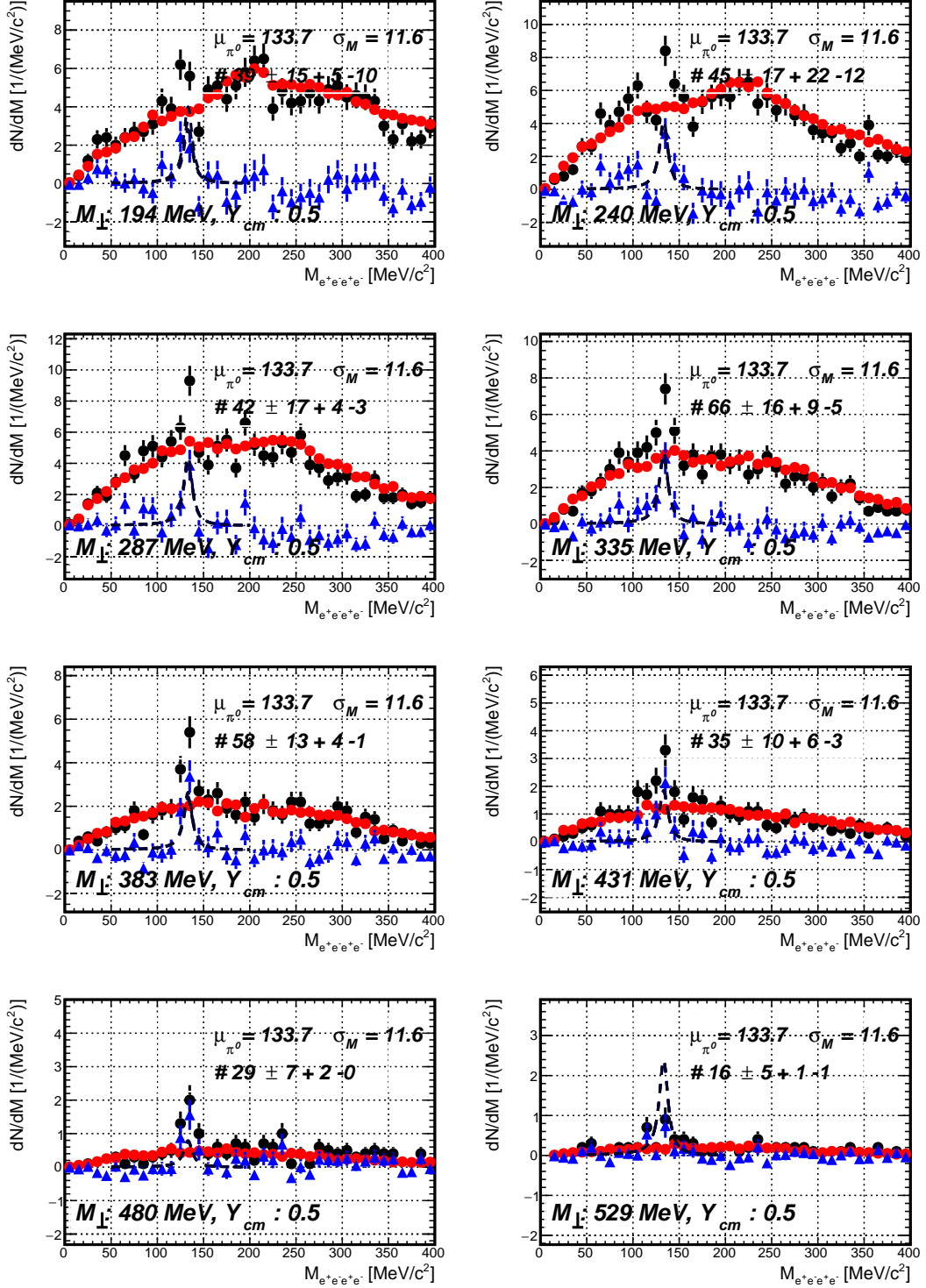
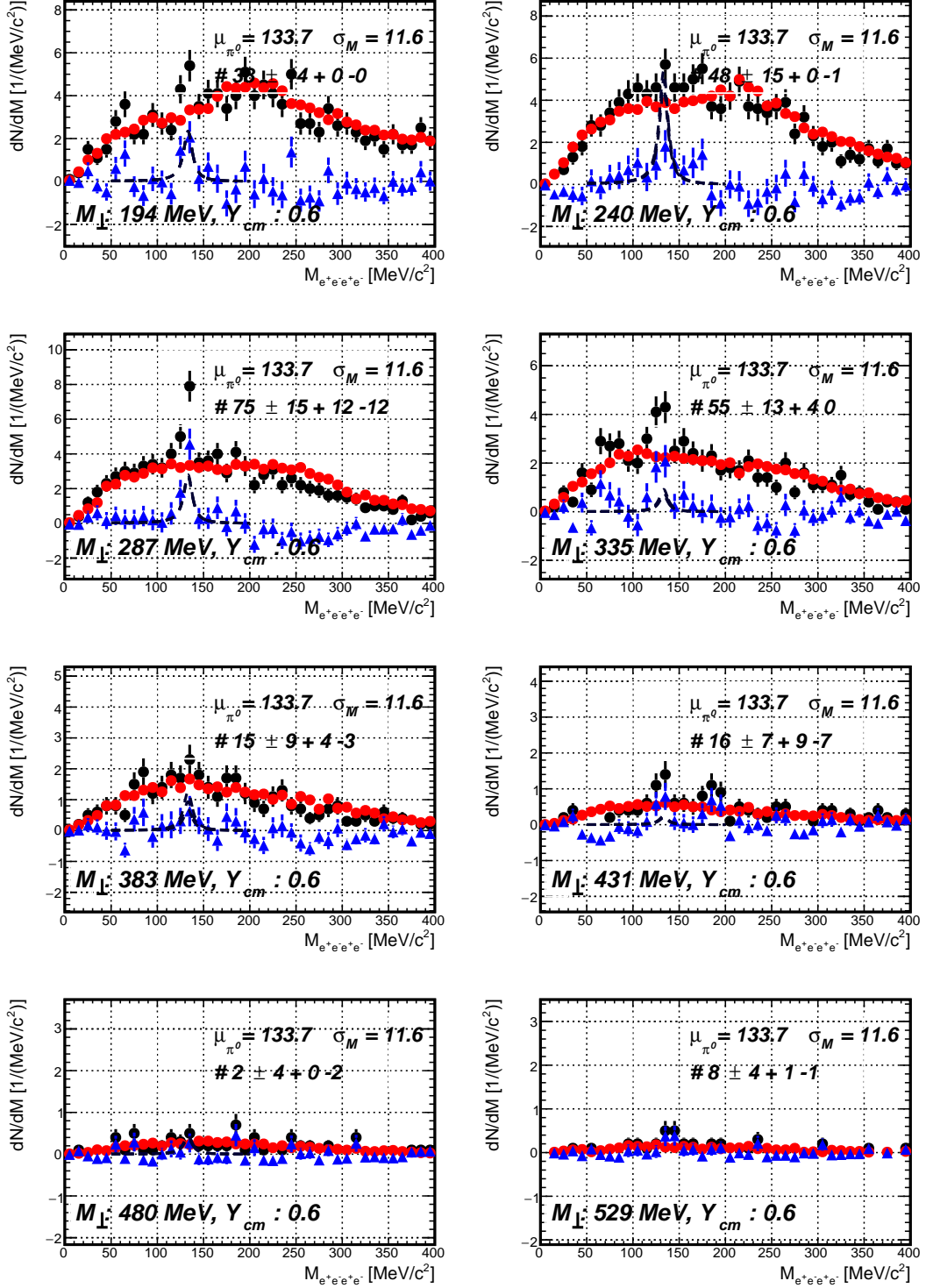Figure A 9: Phase space dependent four lepton invariant mass spectrum with mixed event background (red).

Figure A 10: Phase space dependent four lepton invariant mass spectrum with mixed event background (red).

Index and Glossary

Bibliography

[A+91]   K. Ahmet et al. The OPAL detector at LEP. *Nucl.Instrum.Meth.*, A305:275–319, 1991. 96

[A+97]   R. Averbeck et al. Production of π 0 and η mesons in carbon-induced relativistic heavy-ion collisions. *Zeitschrift für Physik A Hadrons and Nuclei*, 359(1):65–73, 1997. 20, 23, 90, 103

[A+01]   M.N. Achasov et al. Study of conversion decays $\phi \to \eta e^+e^-$ and $\eta \to \gamma e^+e^-$ in the experiment with SND detector at VEPP-2M collider. *Physics Letters B*, 504(4):275–281, 2001. 10

[A+05]   G. Agakichiev et al. e+ e- pair production in Pb - Au collisions at 158-GeV per nucleon. *Eur.Phys.J.*, C41:475–513, 2005. 99

[A+06]   R. Arnaldi et al. First measurement of the rho spectral function in high-energy nuclear collisions. *Phys.Rev.Lett.*, 96:162302, 2006. 99

[A+09a]   G. Agakishiev et al. ϕ decay: A relevant source for K^- production at energies available at the GSI Schwerionen-Synchrotron (SIS)? *Phys. Rev. C*, 80:025209, Aug 2009. 24

[A+09b]   G. Agakishiev et al. Deep Subthreshold Ξ^- Production in Ar+KCl Reactions at $1.76A$ GeV. *Phys. Rev. Lett.*, 103:132301, Sep 2009. 24

[A+09c]   G. Agakishiev et al. The High-Acceptance Dielectron Spectrometer HADES. *Eur. Phys. J.*, A41:243–277, 2009. 29, 33, 100

[A+10a]   A. Adare et al. Detailed measurement of the e^+e^- pair continuum in $p+p$ and Au+Au collisions at $\sqrt{s_{NN}} = 200$ GeV and implications for direct photon production. *Phys.Rev.*, C81:034911, 2010. 99

[A+10b]   Agakishiev et al. In-medium effects on K^0 mesons in relativistic heavy-ion collisions. *Phys. Rev. C*, 82:044907, Oct 2010. 24

[A+10c]   G. Agakishiev et al. Origin of the low-mass electron pair excess in light nucleus-nucleus collisions. *Phys.Lett.*, B690:118–122, 2010. I, 13, 27, 99

[A+11a]   G. Agakishiev et al. Dielectron production in Ar+KCl collisions at 1.76A GeV. *Phys.Rev.*, C84:014902, 2011. III, 24, 27, 99

[A+11b]   G. Agakishiev et al. Hyperon production in Ar+KCl collisions at 1.76A GeV. *Eur. Phys. J.*, A47:21, 2011. 24

[A⁺12a]   Georges Aad et al. Observation of a new particle in the search for the Standard Model Higgs boson with the ATLAS detector at the LHC. *Phys. Lett.*, B716:1–29, 2012. 3

[A⁺12b]   G. Agakishiev et al. Inclusive dielectron production in proton-proton collisions at 2.2 GeV beam energy. *Phys.Rev.*, C85:054005, 2012. 99

[A⁺12c]   G. Agakishiev et al. Inclusive dielectron spectra in p+p collisions at 3.5 GeV. *Eur.Phys.J.*, A48:64, 2012. 99

[A⁺13]   G. Agakishiev et al. Deep sub-threshold K*(892)0 production in collisions of Ar + KCl at 1.76 A GeV. *The European Physical Journal A*, 49(3):1–7, 2013. 24

[A⁺15]   P. A. R. Ade et al. Planck 2015 results. XIII. Cosmological parameters. 2015. 1

[A⁺16]   G. Agakishiev et al. Statistical model analysis of hadron yields in proton-nucleus and heavy-ion collisions at SIS 18 energiesStatistical hadronization model analysis of hadron yields in p + Nb and Ar + KCl at SIS18 energies. *Eur. Phys. J.*, A52(6):178, 2016. 24

[AB⁺03]   M. Abdel-Bary et al. Measurement of the η production in proton-proton collisions with the COSY time-of-flight spectrometer. *The European Physical Journal A - Hadrons and Nuclei*, 16(1):127–137, 2003. 11

[ABB⁺13]   G. Agakishiev, A. Balanda, D. Belver, A. Belyaev, J.C. Berger-Chen, et al. Inclusive pion and eta production in p+Nb collisions at 3.5 GeV beam energy. 2013. 15, 53, 67

[ABBM⁺10] A. Andronic, D. Blaschke, P. Braun-Munzinger, J. Cleymans, K. Fukushima, L.D. McLerran, H. Oeschler, R.D. Pisarski, K. Redlich, C. Sasaki, H. Satz, and J. Stachel. Hadron production in ultra-relativistic nuclear collisions: Quarkyonic matter and a triple point in the phase diagram of QCD. *Nuclear Physics A*, 837(1-2):65–86, 2010. 25

[AHMS03]   R. Averbeck, R. Holzmann, V. Metag, and R. S. Simon. Neutral pions and eta mesons as probes of the hadronic fireball in nucleus-nucleus collisions around 1 AGeV. *Phys. Rev. C*, 67:024903, 2003. I, III, 20, 23, 24, 90, 103

[AP⁺04]   H. Alvarez-Pol et al. A large area timing RPC prototype for ion collisions in the HADES spectrometer. *Nucl.Instrum.Meth.*, A535:277–282, 2004. 31

[ASRS08]   Mark G. Alford, Andreas Schmitt, Krishna Rajagopal, and Thomas Schafer. Color superconductivity in dense quark matter. *Rev. Mod. Phys.*, 80:1455–1515, 2008. 2

[B$^+$98]   S. A. Bass et al. Microscopic models for ultrarelativistic heavy ion collisions. *Prog. Part. Nucl. Phys.*, 41:255–369, 1998. 19, 26, 91

[B$^+$04a]   A. Bałanda et al. The HADES Pre-Shower detector. *Nuclear Instruments and Methods in Physics Research Section A: Accelerators, Spectrometers, Detectors and Associated Equipment*, 531(3):445–458, 2004. 38

[B$^+$04b]   F. Balestra et al. Exclusive eta production in proton-proton reactions. *Phys. Rev.*, C69:064003, 2004. 11, 14

[BA53]   H. A. Bethe and J. Ashkin. Passage of radiation through matter. *Experimental Nuclear Physics*, 10(Part II):253, 1953. 48, 55

[Bar77]   Bertrand C. Barrois. Superconducting Quark Matter. *Nucl. Phys.*, B129:390–396, 1977. 2

[BBC$^+$90]   Frank R. Brown, Frank P. Butler, Hong Chen, Norman H. Christ, Zhihua Dong, Wendy Schaffer, Leo I. Unger, and Alessandro Vaccarino. On the existence of a phase transition for QCD with three light quarks. *Phys. Rev. Lett.*, 65:2491–2494, Nov 1990. 2

[BBC$^+$02]   H. Bokemeyer, J.L. Boyard, V. Chepurnov, S. Chernenko, H. Daues, et al. Development of low-mass drift chambers for the HADES spectrometer. *Nucl.Instrum.Meth.*, A477:397–400, 2002. 33

[BC14]   M. Bashkanov and H. Clement. On a possible explanation of the DLS puzzle. *The European Physical Journal A*, 50(7):1–6, 2014. 13

[BCD$^+$69]   E. D. Bloom, D. H. Coward, H. DeStaebler, J. Drees, G. Miller, L. W. Mo, R. E. Taylor, M. Breidenbach, J. I. Friedman, G. C. Hartmann, and H. W. Kendall. High-Energy Inelastic $e - p$ Scattering at 6° and 10°. *Phys. Rev. Lett.*, 23:930–934, Oct 1969. 7

[BDG$^+$99]   R. Baldini, S. Dubnicka, P. Gauzzi, S. Pacetti, E. Pasqualucci, and Y. Srivastava. Nucleon timelike form-factors below the N anti-N threshold. *Eur. Phys. J.*, C11:709–715, 1999. 9

[BDG$^+$00]   R Baldini, S Dubnička, P Gauzzi, S Pacetti, E Pasqualucci, and Y Srivastava. Determination of nucleon and pion form factors via dispersion relations. *Nuclear Physics A*, 666:38–43, 2000. 9

[Beh11]   C. Behnke. Development of an event generator for dilepton production in heavy ion collisions in the SIS energy regime . Master's thesis, Goethe-Universitaet,Frankfurt am Main, 2011. 26

[BFK+69]   M. Breidenbach, J. I. Friedman, H. W. Kendall, E. D. Bloom, D. H. Coward, H. DeStaebler, J. Drees, L. W. Mo, and R. E. Taylor. Observed Behavior of Highly Inelastic Electron-Proton Scattering. *Phys. Rev. Lett.*, 23:935–939, Oct 1969. 7

[BGG+12]   O. Buss, T. Gaitanos, K. Gallmeister, H. van Hees, M. Kaskulov, et al. Transport-theoretical Description of Nuclear Reactions. *Phys.Rept.*, 512:1–124, 2012. 26

[Blo33]   Felix Bloch. Zur Bremsung rasch bewegter Teilchen beim Durchgang durch Materie. *Annalen der Physik,*, 408(Nr 3):285–320, 1933. 48, 55

[BMRS03]   Peter Braun-Munzinger, Krzysztof Redlich, and Johanna Stachel. Particle production in heavy ion collisions. 2003. 23

[BN77]   Henrik Bohr and H.B. Nielsen. Hadron production from a boiling quark soup: A thermodynamical quark model predicting particle ratios in hadronic collisions. *Nuclear Physics B*, 128(2):275–293, 1977. 2

[BPS+94]   F.-D. Berg, M. Pfeiffer, O. Schwalb, M. Franke, W. Kühn, H. Löhner, V. Metag, M. Notheisen, R. Novotny, A. E. Raschke, J. Ritman, M. Röbig-Landau, R. S. Simon, M. Šumbera, L. Venema, and H. Wilschut. Transverse momentum distributions of η mesons in near-threshold relativistic heavy ion reactions. *Phys. Rev. Lett.*, 72:977–980, Feb 1994. 20, 23, 26, 90, 103

[BR79]   G.E. Brown and Mannque Rho. The little bag. *Physics Letters B*, 82(2):177–180, 1979. 2

[Bro04]   Ian G. Brown. *The Physics and Technology of Ion Sources*. Wiley-VCH, 2004. 30

[BS07]   Braun-Munzinger Peter and Stachel Johanna. The quest for the quark-gluon plasma. *Nature*, 448(7151):302–309, jul 2007. 10.1038/nature06080. 76

[BZS+99]   M Bleicher, E Zabrodin, C Spieles, S A Bass, C Ernst, S Soff, L Bravina, M Belkacem, H Weber, H Stöcker, and W Greiner. Relativistic hadron-hadron collisions in the ultra-relativistic quantum molecular dynamics model. *Journal of Physics G: Nuclear and Particle Physics*, 25(9):1859, 1999. 26

XXX

[C+99]   H. Calen et al. Higher partial waves in p p —¿ p p eta near threshold. *Phys. Lett.*, B458:190–196, 1999. 11

[C+11]   W. Czyzycki et al. Electromagnetic Calorimeter for HADES. 2011. 96

[C+12]   Serguei Chatrchyan et al. Observation of a new boson at a mass of 125 GeV with the CMS experiment at the LHC. *Phys. Lett.*, B716:30–61, 2012. 3

[Cav06]   Tiago Perez Cavalcanti. *η production in p+p reactions in the HADES spectrometer at 2.2 GeV* . dissertation, Justus Liebig Universität Giessen, 2006. 14

[CEKS98]   J. Cleymans, D. Elliott, A. Keränen, and E. Suhonen. Thermal model analysis of particle ratios in Ni+Ni experiments using exact strangeness conservation. *Phys. Rev. C*, 57:3319–3323, Jun 1998. 23

[Che34]   P. A. Cherenkov. Visible emission of clean liquids by action of gamma radiation. *Doklady Akademii Nauk SSSR*, 2:451+, 1934. 32

[CHJ+09]   M. Cheng, P. Hegde, C. Jung, F. Karsch, O. Kaczmarek, et al. Baryon Number, Strangeness and Electric Charge Fluctuations in QCD at High Temperature. *Phys.Rev.*, D79:074505, 2009. 2

[Col]   HADES Collaboration. HYDRA - HADES analysis package. 52

[COR99]   Jean Cleymans, Helmut Oeschler, and Krzysztof Redlich. Influence of impact parameter on thermal description of relativistic heavy ion collisions at (1ˇ2)AGeV. *Phys. Rev. C*, 59:1663–1673, Mar 1999. 23

[CR98]   J. Cleymans and K. Redlich. Unified Description of Freeze-Out Parameters in Relativistic Heavy Ion Collisions. *Phys. Rev. Lett.*, 81:5284–5286, Dec 1998. 23

[CWOR06]   J. Cleymans, S. Wheaton, H. Oeschler, and K. Redlich. Comparison of chemical freeze-out criteria in heavy-ion collisions. *PoS*, CPOD2006:035, 2006. 25

[DGK+]   R.I. Djhelyadin, S.V. Golovkin, V.A. Kachanov, A.S. Konstantinov, V.F. Konstantinov, V.P. Kubarowski, A.V. Kulik, L.G. Landsberg, V.M. Leontiev, V.A. Mukhin, V.F. Obraztsov, T.I. Petrunina, Yu.D. Prokoshkin, V.A. Viktorov, and A.M. Zaitzev. *Physics Letters B*, (4):548–550. 10

[dMFPS06]   J. P. B. C. de Melo, T. Frederico, E Pace, and G. Salme. Space-like and time-like pion electromagnetic form-factor and Fock state components within the light-front dynamics. *Phys. Rev.*, D73:074013, 2006. 9

[DV66]   B. Deler and G. Valladas. Practical formulation of the isobar model. *Il Nuovo Cimento A*, 45(3):559–587, 1966. 20

[ea97]   R. Averbeck et all. Production of p and light mesons in carbon-induced relativistic heavy-ion collisions. *Zeitschrift für Physik A Hadrons and Nuclei*, 359:65–73, 1997. 20, 21, 90, 103

[ea07]   Agakichiev et all. Dielectron Production in ^{12}C+^{12}C Collisions at 2AGeV with the HADES Spectrometer. *Phys. Rev. Lett.*, 98:052302, Feb 2007. I, III, 26

[ea08]   G. Agakishiev et al. Study of dielectron production in ^{1}2C+^{1}2C collisions at 1 GeV. *Physics Letters B*, 663(1–2):43–48, 2008. I, 21, 26

[EB64]   F. Englert and R. Brout. Broken Symmetry and the Mass of Gauge Vector Mesons. *Phys. Rev. Lett.*, 13(9):321–323, August 1964. 3

[EC96]   W. Ehehalt and W. Cassing. Relativistic transport approach for nucleus nucleus collisions from SIS to SPS energies. *Nucl.Phys.*, A602:449–486, 1996. 26

[EvHWB15]   Stephan Endres, Hendrik van Hees, Janus Weil, and Marcus Bleicher. Dilepton production and reaction dynamics in heavy-ion collisions at SIS energies from coarse-grained transport simulations. *Phys. Rev. C*, 92:014911, Jul 2015. 17, 94, 103

[F^{+}07]   I. Frohlich et al. Pluto: A Monte Carlo Simulation Tool for Hadronic Physics. *PoS*, ACAT2007:076, 2007. 21

[FGH^{+}99]   J. Friese, R. Gernhauser, J. Homolka, A. Kastenmuller, P. Maier-Komor, et al. Enhanced quantum efficiency for CsI grown on a graphite based substrate coating. *Nucl.Instrum.Meth.*, A438:86–93, 1999. 32

[FGMKW03]   J. Friese, R. Gernhauser, P. Maier-Komor, and S. Winkler. A new carbon based VUV mirror of high radiation length for the HADES RICH. *Nucl.Instrum.Meth.*, A502:241–245, 2003. 32

[FH11]   Kenji Fukushima and Tetsuo Hatsuda. The phase diagram of dense QCD. *Rept. Prog. Phys.*, 74:014001, 2011. 2

[FK04]   Z. Fodor and S. D. Katz. Critical point of QCD at finite T and mu, lattice results for physical quark masses. *JHEP*, 04:050, 2004. 2

[Flo14]   M. Floris. Hadron yields and the phase diagram of strongly interacting matter. *Nuclear Physics A*, 931:103–112, 2014. 23

[FLW98]   B. Friman, M. Lutz, and G. Wolf. Masses of hadrons in nuclei, November 1998. 6

[FP02]   P. Fonte and V. Peskov. High-resolution TOF with RPCs. *Nucl. Instrum. Meth.*, A477:17–22, 2002. 37

[FS13]   Kenji Fukushima and Chihiro Sasaki. The phase diagram of nuclear and quark matter at high baryon density. *Prog. Part. Nucl. Phys.*, 72:99–154, 2013. 2

[G+53]   Glauber et al. in Lectures in Theoretical Physics. Glauber, 1953. 54

[G+64]   M. Goldberg et al. Existence of a New Meson of Mass 960 MeV. *Phys. Rev. Lett.*, 12:546–550, 1964. 5

[Gal09]   T Galatyuk. *Di-electron spectroscopy in HADES and CBM: from p + p and n + p collisions at GSI to Au + Au collisions at FAIR.* PhD thesis, Goethe-Universitaet,Frankfurt am Main, 2009. I, III, 13, 52, 76, 93

[Gar03]   M. Sánchez García. *Momentum reconstruction and pion production analysis in the HADES spectrometer at GSI.* dissertation, Universidade de Santiago De Compostela, Spain, 2003. 52

[GAR11]   GARFIELD. Simulation of gaseous detectors. Group report and private communication, 2011. 42

[GG11]   R.V. Gavai and Sourendu Gupta. Lattice {QCD} predictions for shapes of event distributions along the freezeout curve in heavy-ion collisions. *Physics Letters B*, 696(5):459–463, 2011. 2

[GHK64]   G. S. Guralnik, C. R. Hagen, and T. W. B. Kibble. Global Conservation Laws and Massless Particles. *Phys. Rev. Lett.*, 13(20):585–587, November 1964. 3

[GHL71]   H.A. Grunder, W.D. Hartsough, and E.J. Lofgren. Acceleration of heavy ions at the bevatron. *Science*, 174:1128–1129, 1971. 18

[GHR+16]   Tetyana Galatyuk, M. Paul Hohler, Ralf Rapp, Florian Seck, and Joachim Stroth. Thermal dileptons from coarse-grained transport as fireball probes at SIS energies. *The European Physical Journal A*, 52(5):1–8, 2016. 17, 19, 94, 103

[Gib10]   Josiah Willard Gibbs. *Elementary Principles in Statistical Mechanics*. Cambridge University Press, 2010. Cambridge Books Online. 23

[GKM+98]   C. Garabatos, W. Karig, C. Muntz, A. Steigerwald, J. Stroth, et al. Optimisation of low mass drift chambers for HADES. *Nucl.Instrum.Meth.*, A412:38–46, 1998. 33

[Gol]   4

[GW73]   David J. Gross and Frank Wilczek. Ultraviolet Behavior of Non-Abelian Gauge Theories. *Phys. Rev. Lett.*, 30:1343–1346, Jun 1973. 1

[H+13]   G. Hinshaw et al. Nine-Year Wilkinson Microwave Anisotropy Probe (WMAP) Observations: Cosmological Parameter Results. *Astrophys. J. Suppl.*, 208:19, 2013. 1

[Har]   Jan Hartmann. Talk at the DPG 2016 and private communication. 92

[Har16a]   Szymon Harabasz. *Reconstruction of virtual photons from Au+Au collosion at 1.23 GeV/u.* dissertation, TU Darmstadt, 2016. 87, 93

[Har16b]   Jan Hartmann. Double polarisation experiments in meson photo-production. 2016. 92

[Hei27]   W. Heisenberg. Über den anschaulichen Inhalt der quantentheoretischen Kinematik und Mechanik. *Zeitschrift fur Physik*, 43:172–198, March 1927. 7

[HG13]   R. Holzmann and M. Gumberidze. *SR2012-PHN-NQM-EXP-06 Inclusive π^0 and η production in the 1.76 GeV/u Ar+KCl reaction*, volume 2013-1 of *GSI Report*. GSI Helmholtzzentrum für Schwerionenforschung, Darmstadt, 2013. 22

[Hig64]   Peter W. Higgs. Broken Symmetries and the Masses of Gauge Bosons. *Phys. Rev. Lett.*, 13(16):508–509, October 1964. 3

[HJ00]   Ulrich W. Heinz and Maurice Jacob. Evidence for a new state of matter: An Assessment of the results from the CERN lead beam program. *nucl-th/0002042*, 2000. 18

[HL92]   Hatsuda and Lee. QCD sum rules for vector mesons in the nuclear medium. *Phys. Rev., C Nucl. Phys.*, 46(1):R34–R38, July 1992. 6

[HR14]   Paul M. Hohler and Ralf Rapp. Probing chiral restoration with ρ-meson melting through sum rules. *J. Phys. Conf. Ser.*, 535:012024, 2014. 6

[Hua13]   Bingchu Huang. Dielectron differential cross section in Au + Au collisions at different beam energies at STAR. *Nucl.Phys.*, A904-905:565c–568c, 2013. 99

[K$^+$64]   George R. Kalbfleisch et al. Observation of a Nonstrange Meson of Mass 959 MeV. *Phys. Rev. Lett.*, 12:527–530, May 1964. 5

[K$^+$14]   G. Kornakov et al. Time of flight measurement in heavy-ion collisions with the HADES RPC TOF wall. *Journal of Instrumentation*, 9(11):C11015, 2014. 37

[Kar15]   B. Kardan. Centrality Determination at 1.23 AGeV Gold-Gold collision and readout-electronics for the HADES electromagnetic calorimeter. Master's thesis, Goethe-Universitaet,Frankfurt am Main, 2015. 34, 35, 55, 87

[KBF$^+$99] A. Kastenmuller, M. Bohmer, J. Friese, R. Gernhauser, J. Homolka, et al. Fast detector readout for the HADES-RICH. *Nucl.Instrum.Meth.*, A433:438–443, 1999. 32

[KDE$^+$04] K. Kanaki, F. Dohrmann, W. Enghardt, C. Garabatos, E. Grosse, et al. HADES tracking system: First in-beam experience. *IEEE Trans.Nucl.Sci.*, 51:939–942, 2004. 33

[KK06]   L.P. Kaptari and Burkhard Kampfer. Di-electron bremsstrahlung in intermediate-energy pn and Dp collisions. *Nucl.Phys.*, A764:338–370, 2006. 13

[KK$^+$11]   W. Koenig, I. Koenig, et al. Delta-electrons in Au+Au: Why they hurt us and what we can do about it. Group report and private communication, 2011. 38

[Koc97]   Volker Koch. Aspects of chiral symmetry. *Int. J. Mod. Phys.*, E6:203–250, 1997. 3

[Kos98]   V. Alan Kostelecky. The Status of CPT. *hep-ph/9810365*, pages 588–600, 1998. 3

[Kru72]   H. Krupp. The unilac ion source and injection system. *IEEE Trans.Nucl.Sci.*, 19:69–73, 1972. 30

[L+03]   J. Lehnert et al. Performance of the HADES ring recognition hard-
            ware. *Nucl.Instrum.Meth.*, A502:261–265, 2003. 32

[Lan85]   L. G. Landsberg. Electromagnetic Decays of Light Mesons. *Phys.
            Rept.*, 128:301–376, 1985. 8

[LEF+13]   R. Lalik, E. Epple, L. Fabbietti, T. Hennino, P. Koczon, et al. CER-
            BEROS — Beam detector for pion experiments at GSI.
            2013. 31

[L'H94]   D. L'Hôte. About resonance signal extraction from multiparticle
            data: combinatorics and event mixing methods. *Nuclear Instru-
            ments and Methods in Physics Research Section A: Accelerators,
            Spectrometers, Detectors and Associated Equipment*, 337(2–3):544–
            556, 1994. 65

[LM98]   Stefan Leupold and Ulrich Mosel. On QCD sum rules for vector
            mesons in nuclear medium. *Phys.Rev.C58:2939-2957,1998*, May
            1998. 6

[LMC+11]   I. Larin, D. McNulty, E. Clinton, P. Ambrozewicz, D. Lawrence,
            I. Nakagawa, Y. Prok, A. Teymurazyan, et al. New Measurement
            of the π^0 Radiative Decay Width. *Phys. Rev. Lett.*, 106:162303,
            Apr 2011. 66

[LMOP47]   C. M. G. Lattes, H. Muirhead, G. P. S. Occhialini, and C. F. Pow-
            ell. PROCESSES INVOLVING CHARGED MESONS. *Nature*,
            159:694–697, 1947. [,42(1947)]. 4

[M+97]   A. Marín et al. Exclusive Ïo- and Î·-meson production in 40Ar +
            natCa at 800A MeV. *Physics Letters B*, 409(1):77–82, 1997. 20,
            23, 26, 90, 103

[M+99]   G. Martínez et al. Deep-Subthreshold η and π^0 Production Probing
            Pion Dynamics in the Reaction $Ar + Ca$ at $180A$ MeV. *Phys. Rev.
            Lett.*, 83:1538–1541, Aug 1999. 20, 23, 26, 90, 103

[M+04]   C. Muntz et al. The hades tracking system. *Nucl.Instrum.Meth.*,
            A535:242–246, 2004. 33, 34

[Mar05]   J. Markert. *Untersuchung zum Ansprechverhalten der Vieldraht-
            Driftkammern niedriger Massenbelegung des HADES Experimentes
            *. PhD thesis, Goethe-Universitaet,Frankfurt am Main, 2005. 41,
            43, 44, 52

[Max67]   J. Clerk Maxwell. On the Dynamical Theory of Gases. *Philosoph-
            ical Transactions of the Royal Society of London*, 157:49–88, 1867.
            76

XXXVI

[Mic12]   J. Michel. *Development and Implementation of a New Trigger and Data Acquisition System for the HADES Detector.* PhD thesis, Goethe-Universitaet,Frankfurt am Main, 2012. 39

[MP07]   Larry McLerran and Robert D. Pisarski. Phases of Cold, Dense Quarks at Large Nc. *Nucl. Phys.*, A796:83–100, 2007. 2

[N$^+$10]   K Nakamura et al. Review of particle physics. *J. Phys.*, G37:075021, 2010. 3, 4, 5, 7

[Nam60]   Yoichiro Nambu. Quasi-Particles and Gauge Invariance in the Theory of Superconductivity. *Phys. Rev.*, 117:648–663, Feb 1960. 4

[NJL61]   Y. Nambu and G. Jona-Lasinio. Dynamical Model of Elementary Particles Based on an Analogy with Superconductivity. I. *Phys. Rev.*, 122:345–358, Apr 1961. 2, 6

[O$^+$14]   K. A. Olive et al. Review of Particle Physics. *Chin. Phys.*, C38:090001, 2014. 25, 26, 92

[P$^+$61]   A. Pevsner et al. Evidence for a Three Pion Resonance Near 550-MeV. *Phys. Rev. Lett.*, 7:421–423, 1961. 5

[P$^+$97]   R. J. Porter et al. Dielectron Cross Section Measurements in Nucleus-Nucleus Reactions at $1.0A$ GeV. *Phys. Rev. Lett.*, 79:1229–1232, Aug 1997. 21, 99

[P$^+$04]   H. Alvarez Pol et al. A large area timing RPC prototype for ion collisions in the HADES spectrometer. *Nuclear Instruments and Methods in Physics Research Section A: Accelerators, Spectrometers, Detectors and Associated Equipment*, 535(1–2):277–282, 2004. Proceedings of the 10th International Vienna Conference on Instrumentation. 37

[Pes95]   M.; Schroeder D Peskin. *An Introduction to Quantum Field Theory.* Westview Press., 1995. 7

[PFKW10]   J. Pietraszko, L. Fabbietti, W. Koenig, and M. Weber. Diamonds as timing detectors for minimum-ionizing particles: The HADES proton-beam monitor and START signal detectors for time of flight measurements. *Nuclear Instruments and Methods in Physics Research Section A: Accelerators, Spectrometers, Detectors and Associated Equipment*, 618(1–3):121–123, 2010. 36

[PGG$^+$14] J. Pietraszko, T. Galatyuk, V. Grilj, W. Koenig, S. Spataro, and M. Träger. Radiation damage in single crystal {CVD} diamond material investigated with a high current relativistic 197Au beam.

Nuclear Instruments and Methods in Physics Research Section A: Accelerators, Spectrometers, Detectors and Associated Equipment, 763:1–5, 2014. 35, 36

[PMW+06]   M. Procura, B. U. Musch, T. Wollenweber, T. R. Hemmert, and W. Weise. Nucleon mass: From lattice QCD to the chiral limit. *Phys. Rev. D*, 73:114510, Jun 2006. 3

[Poi06]   Henri Poincaré. Sur la dynamique de l'électron. *Rendiconti del circolo matematico di Palermo*, 21:129–176, 1906. 3

[Pol73]   H. David Politzer. Reliable Perturbative Results for Strong Interactions? *Phys. Rev. Lett.*, 30:1346–1349, Jun 1973. 1

[Pro96]   Proceedings AIHENP'96 Workshop, Lausanne. *An Object Oriented Data Analysis Framework*, volume 389, Sept 1996. 52

[R+07]   W. Reisdorf et al. Systematics of pion emission in heavy ion collisions in the 1A- GeV regime. *Nucl. Phys.*, A781:459–508, 2007. 87

[Rei08]   Frederick Reif. *Fundamentals of Statistical and Thermal Physics*. Waveland Pr Inc;, 56946th edition, December 2008. 76

[Rus06]   A. Rustamov. Exclusive omega Meson Reconstruction in Proton-Proton Collisions at 2.2 GeV with the HADES Spectrometer and High Resolution Tracking, 2006. 14, 46

[Rut11]   E. Rutherford. The scattering of alpha and beta particles by matter and the structure of the atom. *Phil.Mag.*, 21:669–688, 1911. 2, 8

[RW02]   R. Rapp and J. Wambach. Chiral Symmetry Restoration and Dileptons in Relativistic Heavy-Ion Collisions. In *Advances in Nuclear Physics*, volume 25 of *Advances in Nuclear Physics*, pages 1–205. Springer US, 2002. 10.1007. 17

[Sak60]   J. J. Sakurai. Theory of strong interactions. *Annals Phys.*, 11:1–48, 1960. 7

[SBCM89]   M. Schaefer, T.S. Biro, W. Cassing, and U. Mosel. e+eâ Production in proton-neutron collisions. *Physics Letters B*, 221(1):1–5, 1989. 12

[SC81]   R. Santonico and R. Cardarelli. Development of Resistive Plate Counters. *Nucl.Instrum.Meth.*, 187:377–380, 1981. 37

[Sch95]   H Schoen. *Ein Dielektronenspekrometer hoher Akzeptanz fuer relativistische Schwerionenkollisionen*. PhD thesis, Goethe-Universitaet,Frankfurt am Main, 1995. 36

[Sch08]   Alexander Schmah. *Produktion von Seltsamkeit in Ar+KCl Reaktionen bei 1.756 AGeV mit HADES.* PhD thesis, Fachbereich Physik, Technische Universität Darmstadt, Darmstadt, 2008. 45, 46, 52

[Sch15]   T. Scheib. V^0 Reconstruction of Strange Hadrons in Au+Au Collisions at 1.23 AGeV with HADES. *J.Phys.Conf.Ser.*, 599(1):012030, 2015. 4, 44

[Sch16]   Heidi Schuldes. *Charged Koan and Phi reconsturction in Au=Au collisions at 1.23 Gev/u with HADES.* PhD thesis, Goethe-Universitaet,Frankfurt am Main, 12016. 4, 47, 48, 54, 62, 77, 87, 88, 91, 93, 103

[SEK+10]   Peter Spiller, Hartmut Eickhoff, Holger Kollmus, Patrick Puppel, Hartmut Reich-Sprenger, et al. Acceleration of Intermediate Charge State Heavy Ions in SIS18. *Conf.Proc.*, C100523:MOPD002, 2010. 30

[Sel15]   P. Sellheim. Backtracking algorithm for lepton reconstruction with HADES. *J.Phys.Conf.Ser.*, 599(1):012027, 2015. 93

[Sel16]   Patrick Sellheim. *Backtracking alorithm for dielection reconstrucktion with HADES.* dissertation, Goethe Universitaet Frankfurt, 2016. 87, 93

[Sen]   Peter. Senger. Erzeugung von Pionen und Kaonen in relativistischen Schwerionenstoesen. Habilitationsschrift Universitaet Frankfurt, 1995, 106 pages. 20

[SL15]   Heidi Schuldes and Manuel Lorenz. Protons and light fragments in Ar+KCl at 1.76 AGeV measured with HADES. *J. Phys. Conf. Ser.*, 599(1):012028, 2015. 24

[SM03]   R. Shyam and U. Mosel. Role of baryonic resonances in the dilepton emission in nucleon-nucleon collisions. *Phys.Rev.*, C67:065202, 2003. 12

[SM10]   R. Shyam and U. Mosel. Dilepton production in proton-proton and quasifree proton-neutron reactions at 1.25 GeV. *Phys. Rev. C*, 82:062201, Dec 2010. 13

[SP+94]   O. Schwalb, M. Pfeiffer, et al. Mass dependence of Ï0-production in heavy ion collisions at 1 A GeV. *Physics Letters B*, 321(1):20–25, 1994. 20, 23, 26, 90, 103

[Spa05]   Stefano Spatano. *CHARACTERIZATION OF THE HADES SPECTROMETER IN PP COLLISIONS AT 2.2 GEV: ELASTIC SCATTERING AND EXCLUSIVE ETA RECONSTRUCTION* . dissertation, UNIVERSITÀ DEGLI STUDI DI CATANIA, 2005. 14

[Spa07]   S. Spataro. eta meson reconstruction in pp reactions at 2.2-GeV with HADES. *Int. J. Mod. Phys.*, A22:533–536, 2007. 14

[SPS50]   J. Steinberger, W. K. H. Panofsky, and J. Steller. Evidence for the Production of Neutral Mesons by Photons. *Phys. Rev.*, 78:802–805, Jun 1950. 4

[SPW07]   B.-J. Schaefer, J. M. Pawlowski, and J. Wambach. Phase structure of the Polyakov-quark-meson model. *Phys. Rev. D*, 76:074023, Oct 2007. 2

[SS07]   Maria Schmah and Alexander Schmah. Technical Simulation of the HADES . www-HADES.gsi.de, 2007. 29

[SSS15]   Horst Stöcker, Thomas Stöhlker, and Christian Sturm. FAIR - Cosmic Matter in the Laboratory. *J. Phys. Conf. Ser.*, 623(1):012026, 2015. 97

[Ste09]   M. A. Stephanov. Non-Gaussian Fluctuations near the QCD Critical Point. *Phys. Rev. Lett.*, 102:032301, Jan 2009. 2

[Ste11]   M. A. Stephanov. Sign of Kurtosis near the QCD Critical Point. *Phys. Rev. Lett.*, 107:052301, Jul 2011. 2

[T+09]   P. Tlusty et al. Charged pion production in C+C and Ar+KCl collisions measured with HADES. In *Proceedings, 47th International Winter Meeting on Nuclear Physics (Bormio 2009): Bormio, Italy, January 26-30, 2009*, 2009. 24

[Tar10]   A Tarantola. *Dielectron analysis in p+p collisions at 3.5 GeV with the HADES spectrometer: omega-meson line shape and a new electronics readout for the Multi-wire Drift Chambers.* PhD thesis, Goethe-Universitaet,Frankfurt am Main, 2010. 14, 32

[Taw14]   Abdel Nasser Tawfik. Equilibrium statistical–thermal models in high-energy physics. *International Journal of Modern Physics A*, 29(17):1430021, 2014. 23

[Tei11]   Kaled Teilab. *The production of η and ω mesons in 3.5 GeV p+p interaction in HADES* . PhD thesis, Goethe-Universitaet,Frankfurt am Main, 2011. 14, 15

[Tul87]   J. K. Tuli. EVALUATED NUCLEAR STRUCTURE DATE FILE: A MANUAL FOR PREPARATION OF DATA SETS. 1987. 68

[TVL14]   Giorgio Torrieri, Sascha Vogel, and Stefano Lottini. Phenomenology of quarkyonic matter in heavy-ion collisions. *Journal of Physics: Conference Series*, 509(1):012035, 2014. 2

[Ura11]   Antonio Uras. Measurement of the η and *omega* Dalitz decays transition form factors in p-A collisions at 400 GeV/c with the NA60 apparatus. *J. Phys. Conf. Ser.*, 270:012038, 2011. 10

[Vog14]   Sascha Vogel. Studying quarkyonic matter at {FAIR} energies with electromagnetic probes. *Nuclear Physics A*, 932:224–229, 2014. Hard Probes 20136th International Conference on Hard and Electromagnetic Probes of High-Energy Nuclear Collisions. 2

[Vol01]   J. et.al. Volmer. Measurement of the Charged Pion Electromagnetic Form Factor. *Phys. Rev. Lett.*, 86:1713–1716, Feb 2001. 9

[VPS+08]   S. Vogel, H. Petersen, K. Schmidt, E. Santini, C. Sturm, J. Aichelin, and M. Bleicher. How Sensitive are Di-Leptons from Rho Mesons to the High Baryon Density Region? *Phys.Rev.C78:044909,2008*, May 2008. 7, 17

[VW91]   U. Vogl and W. Weise. The Nambu and Jona Lasinio model: Its implications for hadrons and nuclei. *Prog. Part. Nucl. Phys.*, 27:195–272, 1991. 3

[W+98]   A. R. Wolf et al. Multistep Production of η and Hard π^0 Mesons in Subthreshold Au-Au Collisions. *Phys. Rev. Lett.*, 80:5281–5284, Jun 1998. 20, 23, 26, 90, 103

[WCH09]   S. Wheaton, J. Cleymans, and M. Hauer. THERMUS—A thermal model package for {ROOT}. *Computer Physics Communications*, 180(1):84–106, 2009. 24, 90

[Wei93]   W. Weise. Nuclear aspects of chiral symmetry. *Nuclear Physics A*, 553:59–72, 1993. 6

[Wil74]   Kenneth G. Wilson. Confinement of quarks. *Phys. Rev. D*, 10:2445–2459, Oct 1974. 1

[Wil99]   Frank Wilczek. The Recent Excitement in High-Density QCD. *Nucl.Phys. A663 (2000) 257-271*, August 1999. 3

[Z+99]   K. Zeitelhack et al. The HADES RICH detector. *Nucl.Instrum.Meth.*, A433:201–206, 1999. 32

Curriculum Vitae

NAME:	Claudia Behnke
DATE OF BIRTH:	30 September 1986
PLACE OF BIRTH:	Bad Soden, Germany
ADDRESS:	Nusszeil 60
	60433 Frankfurt
	Germany
PHONE:	(+49) 171 3852865
EMAIL:	c.behnke@gsi.de

Education

09/2011 -10/2016	PHD CANDIDATE Goethe Universität Frankfurt, Frankfurt a. M. Institute for nuclear physics DOCTORAL ADVISOR: Prof. Dr. J. Stroth CO-PROMOTOR: Prof Dr. T. Galatyuk THESIS TITLE: *Reconstruction of π^0 and η mesons via conversion in Au+Au at 1.23 GeV/u with the HADES spectrometer*
09/2009 - 09/2011	MASTER OF SCIENCE Goethe Universität Frankfurt, Frankfurt a. M. Institute for nuclear physics SUPERVISOR: Prof. Dr. J. Stroth PhD THESIS TITLE: *Development of an event generator for dilepton production in heavy ion collisions in the SIS energy regime*
09/2006 - 09/2009	BACHELOR OF SCIENCE Goethe Universität Frankfurt, Frankfurt a. M. Institute for nuclear physics SUPERVISOR: Prof. Dr. J. Stroth THESIS TITLE: *UrQMD-Simulations for the HADES-Experiment*
09/1999 - 06/2006	ABITUR, Pestallozzi Schule Gymnasium - Idstein, Germany Majors: Physics and German Graduation: Abitur